# Developing an Elevated Temperature Pourbaix Diagram for Zirconium and Multi-Element Pourbaix Diagram of Zircaloy-4

by

Graeme J. Francolini

A thesis submitted to the
School of Graduate and Postdoctoral Studies in partial
fulfillment of the requirements for the degree of

**Master of Science in Materials Science**

Faculty of Science

University of Ontario Institute of Technology (Ontario Tech University)

Oshawa, Ontario, Canada

August 2023

**THESIS EXAMINATION INFORMATION**

Submitted by: **Graeme J. Francolini**

**Master of Science** in **Materials Science**

Thesis title: Developing an Elevated Temperature Pourbaix Diagram for Zirconium and Multi-Element Pourbaix Diagram of Zircaloy-4

An oral defense of this thesis took place on July 18th, 2023 in front of the following examining committee:

**Examining Committee:**

| | |
|---|---|
| Chair of Examining Committee | Dr. Jennifer McKellar |
| Research Supervisor | Dr. Matthew H. Kaye |
| Examining Committee Member | Dr. Markus Piro |
| Examining Committee Member | Dr. Bill Atkinson |
| Thesis Examiner | Dr. Brian M. Ikeda |

The above committee determined that the thesis is acceptable in form and content and that a satisfactory knowledge of the field covered by the thesis was demonstrated by the candidate during an oral examination. A signed copy of the Certificate of Approval is available from the School of Graduate and Postdoctoral Studies.

## Abstract

Zirconium and Zircaloy-4 are used in applications that require corrosion resistance under extreme conditions. For example, the fuel bundles in coolant systems of CANDU™ reactors operate between 533 to 583 K (260 to 310 °C). However, thermodynamic and hydrolysis properties of aqueous zirconium species have not been measured above standard conditions.

This lack of information is addressed through solubility measurements and the development of elevated temperature Pourbaix (E-pH) diagrams for zirconium and Zircaloy-4. These Pourbaix diagrams of zirconium and multi-element diagram (Sn, Zr, Cr) of Zircaloy-4 were developed at 373.15 K (100 °C). Solubility measurements were made using a batch-style pressure vessel and concentration measurements were made using ICP-OES and ICP-MS, for zirconium and Zircaloy-4, respectively.

For $Zr(OH)_6^{2-}$, $Zr(OH)_{4\,(aq)}$, and $Zr(OH)_2^{2+}$ the hydrolysis constants were found to be -19.39±1.98, 1.77±1.60, and 3.72±1.63, and the Gibbs energy of formation were: -2177.40±8.49 kJ/mol; -1704.86±1.46 kJ/mol; and -1095.05±2.72 kJ/mol, respectively.


**Keywords:** Pourbaix diagrams; Aqueous chemistry; thermodynamics; Zircaloy-4; zirconium.

**AUTHOR'S DECLARATION**

I hereby declare that this thesis consists of original work of which I have authored. This is a true copy of the thesis, including any required final revisions, as accepted by my examiners.

I authorize the University of Ontario Institute of Technology (Ontario Tech University) to lend this thesis to other institutions or individuals for the purpose of scholarly research. I further authorize University of Ontario Institute of Technology (Ontario Tech University) to reproduce this thesis by photocopying or by other means, in total or in part, at the request of other institutions or individuals for the purpose of scholarly research. I understand that my thesis will be made electronically available to the public.

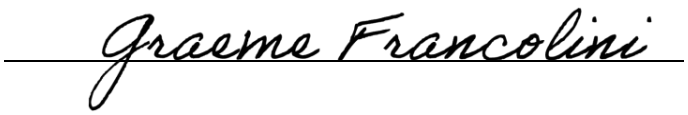

Graeme Francolini

## STATEMENT OF CONTRIBUTIONS

All ICP-MS measurements mentioned in Chapters 4 and 5 of this work were performed by Dr. Karla Newman at the University of Trent's Water Quality Centre. All samples were taken and prepared by myself before being transported to the University of Trent for analysis.

This work was presented at the Canadian Material Science Conference 2023 at the University of Manitoba, titled "Developing an Elevated Temperature Pourbaix Diagram for Zirconium and Zircaloy-4". All work and presenting were performed by myself and a Student Oral Presentation award (Green and Sustainability Section) was given.

I hereby certify that I am the sole author of this thesis and that no part of this thesis has been published or submitted for publication. I have used standard referencing practices to acknowledge ideas, research techniques, or other materials that belong to others. Furthermore, I hereby certify that I am the sole source of the creative works and/or inventive knowledge described in this thesis.

# *Acknowledgements*

Thank you to NSERC for the scholarship which allowed me to focus on this research without worry of needing additional financial income to sustain myself. I'd also like to thank BWXT NEC for donating the Zircaloy-4 tubes which were used in the work, only half this work could have been completed without this. Similarly, I'd like to thank the Trent Water Quality Centre for performing high quality ICP-MS analysis of my samples and for putting up with the relatively chaotic planning of this. Thank you to Michael Allison for allowing to use the ICP-OES and ensuring I had the proper training on the instrument.

It is important that I thank those who assisted me both with my work and outside of it as well. Thank you to my fellow graduate students for helping keep me sane during this sometimes stressful process, and particularly to the members of the Piro group for adopting me and including me in many activities. I will miss our random outings and late night D&D sessions.

Thank you to my fellow office gremlin, Kevin Sawatzky, for making the long hours working in the office enjoyable and listening to me ramble. I hope you did not get tired of my random outbursts and mumbles.

Of course thank you to my supervisor, Dr. Matthew H. Kaye. I've learned a lot from you over these past two years. I appreciate that you always made sure I wasn't working too hard and you're willingness to sit down for long discussions. Thank you for your mentorship and never stopping me when I've wanted to learn more or get training on a new method.

My appreciation does not only exist for those in the the university, but in the community as well. I want to thank every member of the Oshawa Vikings rugby club for giving me a second home while I have pursued my graduate studies. From the first week of moving to Oshawa all the way to the completion of this degree, you have given me a place to get away and have allowed me to

grow as a leader and a person. You can guarantee if I am ever back in town that I will stop by the club for a rye & ginger.

Lastly, to my partner Kaitlin. You're support over the last two years has been incredible. From moving away from home for the first time for me to putting up with me during stressful times and health issues. Thank you. I think sometimes you believe you have not done much for me, but you have been a constant support. I look forward to continuing my studies with you by my side.

# Contents

# List of Figures

# List of Tables

# List of Abbreviations

| | |
|---|---|
| **BWR** | Boiling water reactor |
| **CALPHAD** | Calculation of Phase Diagram |
| **CANDU** | CANada Deuterium Uranium |
| **CEF** | Compound energy formulism |
| **DFT** | Density Functional Theory |
| **HKF** | Helgeson-Kirkham-Flowers |
| **ICP-MS** | Inductively coupled plasma – mass spectrometry |
| **ICP-OES** | Inductively coupled plasma – optical emission spectroscopy |
| **MPEA** | Multi-principle element alloy |
| **NEA** | Nuclear Energy Agency |
| **ORP** | Oxidation-reduction potential |
| **PAS** | Polyarylsulfone |
| **PTFE** | Polytetrafluoroethylene |
| **SCC** | Stress corrosion cracking |
| **SER** | Standard element reference |
| **SIT** | Specific ion interaction |
| **SPP** | Secondary phase particles |
| **WQC** | Water quality centre |

# Physical Constants

| | |
|---|---|
| Dimensional constant for effective Born coefficient | $\eta = 1.660\,27 \times 10^{-5}\ \text{Å} \cdot\ \text{cal} \cdot \text{mol}^{-1}$ |
| Faraday's constant | $F = 9.648\,533\,212\,331\,001\,84 \times 10^{4}\ \text{C} \cdot \text{mol}^{-1}$ |
| Universal gas constant | $R = 8.3145\,\text{J} \cdot \text{mol}^{-1} \cdot \text{K}^{-1}$ |

# List of Symbols

| | |
|---|---|
| $\alpha_{\mathrm{i}}$ | Activity of species $i$ |
| $\beta$ | Hydrolysis constant |
| $\beta^{\circ}$ | Zero ionic strength hydrolysis constant |
| $\gamma_{\mathrm{i}}$ | Activity coefficient of species $i$ |
| $\epsilon$ | Interaction coefficient |
| $\epsilon_{\mathrm{w}}$ | Temperature-dependent dielectric constant function of water |
| $\Theta$ | HKF model solvation parameter, equal to 228 K |
| $\Phi$ | HKF model solvation parameter, equal to 2600 bar |
| $\omega_{\mathrm{e}}$ | Effective Born coefficient |
| $a$ | Criss-Cobble entropy correspondence principal constant |
| $A$ | Heat capacity parameter at 25°C for the Criss-Cobble method |
| $a_3$ | Species-dependent non-solvation parameter for the HKF model |
| $a_4$ | Species-dependent non-solvation parameter for the HKF model |
| $a_{dh}$ | Effective ionic radius |
| $A_{dh}$ | Temperature dependent Debye-Hückel constant |
| $b$ | Criss-Cobble entropy correspondence principal constant |
| $B$ | Heat capacity parameter at 25°C for the Criss-Cobble method |
| $b_d$ | Experimentally derived constant from the Davies equation |
| $B_{dh}$ | Temperature dependent Debye-Hückel constant |
| $b_i$ | Molar fraction of the i-th element |
| $c_1$ | Species-dependent non-solvation parameter for the HKF model |
| $c_2$ | Species-dependent non-solvation parameter for the HKF model |
| $C_i$ | Concentration of species $i$ |

| | |
|---|---|
| $C_p$ | Constant pressure heat capacity |
| $C_p^\circ$ | Constant pressure heat capacity at standard conditions |
| $C_v$ | Constant volume heat capacity |
| $C_v^\circ$ | Constant volume heat capacity at standard conditions |
| $E$ | Electrochemical potential |
| $E^\circ$ | Standard electrochemical potential |
| $E_H$ | Standard Hydrogen Electrode |
| $G$ | Gibbs energy |
| $G_f$ | Gibbs energy of formation |
| $G_r$ | Gibbs energy of reaction |
| $G^\circ$ | Standard Gibbs energy |
| $H$ | Enthalpy |
| $H^\circ$ | Standard enthalpy |
| $I$ | Ionic strength |
| $K$ | Equilibrium constant |
| $K^\circ$ | Zero ionic strength equilibrium constant |
| $M$ | metal |
| $m$ | Ion concentration |
| $n$ | number; often number of electrons involved in a reaction |
| $P_r$ | Reference pressure |
| $Q_H$ | Heat |
| $r_e$ | Effective electrostatic radius of species |
| $r_M$ | Ionic radii of cation |
| $r_N$ | Ionic radii of anion |
| $r_{NM}$ | Ionic radii of molecule |
| $S$ | Entropy |
| $S^\circ$ | Standard entropy |
| $T$ | Temperature |

| | |
|---|---|
| $X$ | Born function |
| $Z_e$ | Effective charge |
| $z$ | Charge of ion |
| $z_i$ | Charge of species $i$ |

# Chapter 1

# Introduction & Background

Metals and alloys are a grouping of materials that are used in a wide range of important applications, such as chemical processing, construction, and various methods of power production. The operating conditions in some of these applications can be extreme, which is the case in nuclear power generation. The internal materials of a reactor must withstand high temperatures, pressures, and have beneficial neutronic properties, with some doing so in aqueous and corrosive environments over extended periods of time. A Canadian example of such an environment would be the CANada Deuterium Uranium (CANDU™) reactor where the temperature and pressure of the heat transport system can vary from 265 °C and 11.05 MPa to 310 °C and 9.89 MPa, at the inlet and outlet respectively [1, 2]. A main component used in the CANDU reactors is the zirconium based alloy, Zircaloy-4, which makes up the fuel rod sheaths and bundles.

Zircaloy-4 and other zirconium alloys can also be exposed to extreme conditions post-reactor as well; for instance in post-irradiation wet storage conditions where light water reactor fuel bundles are known to peak at 603 K initially and decline to between 363 K and 423 K [3]. Similar behaviour is expected for CANDU fuel bundles but with lower temperatures due to their lower burn-up [3]. Deep geologic repositories are another possible environment zirconium alloys might be present [4], where geochemical conditions are difficult to control during a containment breach.

As these materials are used in such important applications while being under severe conditions, it is important that their material properties are well studied and understood. One particular property of interest for metals and alloys is how they corrode and behave under aqueous conditions.

This work investigates this aqueous corrosion through development of an elevated temperature Pourbaix (potential-pH) diagram for both zirconium and a multi-element Pourbaix diagram for Zircaloy-4 at elevated and standard conditions.

## 1.1 Aqueous Corrosion Behaviour of Metals and Alloys

### 1.1.1 General Corrosion Process

Corrosion is the natural process where a pure or refined metal undergoes degradation due to interactions with its environment. This process is destructive in nature and typically results in the formation of a metal oxide product, though other corrosion products are possible.

Since corrosion is an electrochemical process, it can be expressed in terms of half-cell reactions. At the anodic half-cell the metal is oxidized, resulting in an aqueous ionic metal species and free electrons. A general equation for this is given below.

$$M_{(s)} \rightarrow M^{n+}_{(aq)} + ne^- \tag{1.1}$$

In the cathodic half-cell, a given species undergoes reduction and with that, a gain of electrons at the cathodic site. This reaction can be generally illustrated in two ways, as shown in equations 1.2 and 1.3, where equation 1.2 is the dominant cathodic reaction in acidic solutions and equation 1.3 is the dominant cathodic

reaction in neutral or basic solutions [5].

$$2H^{+}_{(aq)} + 2e^{-} \rightarrow H_{2(g)} \tag{1.2}$$

$$O_{2(g)} + 2H_2O + 4e^{-} \rightarrow 4OH^{-}_{(aq)} \tag{1.3}$$

However, not all anodic are corrosion reactions. For example, the anodic reaction shown for chromium [5], equation 1.4.

$$Cr^{3+}_{(aq)} + 4H_2O \rightarrow CrO^{2-}_{4(aq)} + 8H^{+}_{(aq)} + 3e^{-} \tag{1.4}$$

This reaction results in a charge transfer with no loss of metal. The definition for a corrosion reaction is that there must be a simultaneous transfer of mass and charge across the metal/solution interface [5]. During a corrosion reaction the anodic and cathodic reactions function in a coupled manner, though these reactions do not typically occur at the same location on the metal surface. The nature of metals then allow the electrons released in the anodic reaction to be effectively transported along the surface of the metal, as illustrated in Figure 1.1.

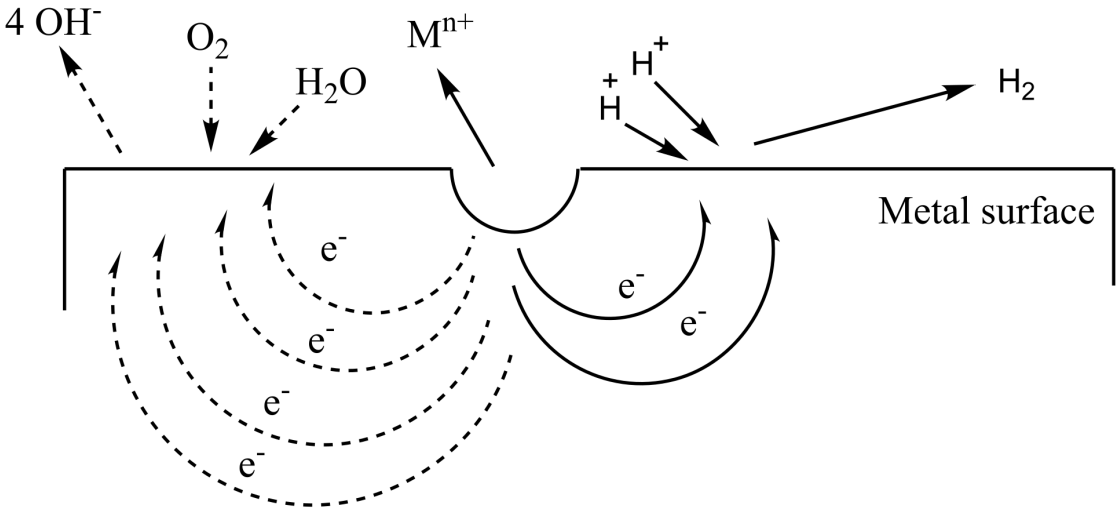


FIGURE 1.1: General corrosion reaction at the metal surface for acidic (right) and neutral/basic (left) conditions. Adapted from [5].

These anodic and cathodic reactions do not continuously occur at the same anodic and cathodic sites of the metal, but rather occur at different spots on the metal surface over time, which is because metal atoms at higher energy sites are more likely to react and dissolve into solution [5]. As these reactions occur, the energy distribution of the reaction sites changes, causing the corrosion to be locally uniform, overall.

### 1.1.2 Localized Corrosion Mechanisms

Not all corrosion mechanisms result in uniform corrosion of a material. Pitting, crevice corrosion, stress corrosion cracking (SCC), and galvanic corrosion are corrosion mechanisms that cause selected attack. These occur when the anode and cathode sites become fixed on the metal surface and cause greater damage in a specific or localized area rather than over the entire material. Pitting corrosion is a common form of corrosion that occurs with metals and is one that can be extremely damaging if left unchecked [6].

Pitting corrosion is known to have three possible mechanisms: penetration, film thinning, and film rupture [5]. In the penetration mechanism, aggressive anions diffuse through the oxide layer to the underlying metal surface resulting in a localized dissolution at the metal/oxide interface. The film thinning mechanism occurs with the localized breakdown of the passivating oxide layer as a result of adsorption of aggressive anions, such as $Cl^-$. The exposure of the metal surface from this breakdown allows for the reduction of oxygen in the solution to occur on the metal surface. The reaction is given below in Equation 1.5.

$$O_{2(aq)} + 2H_2O_{(l)} + 4e^- \rightarrow 4OH^-_{(aq)} \tag{1.5}$$

This reduction on the metal surface results in an increased concentration of dissolved metal cations within the pit. As these cations within the pit do not readily diffuse into the bulk solution as a result of the restricted geometry [5].

This accumulation of metal ions causes them to hydrolyze and to generate hydrogen ions. The overall effect of this being a localized build up of positively charged particles within the pit. Chloride anions are drawn into the pit to maintain charge neutrality, resulting in further corrosion of the metal as the chloride breaks down the protective film on the metal [5, 6].

Lastly, in the film rupture mechanism aggressive ions enter the oxide layer through cracks and defects in the layer. The anion rich layer begins growing under the oxide layer. Resulting in an uplifting of the oxide, in addition to the anions reacting with the underlying metal surface [5].

Crevice corrosion is similar in nature to pit corrosion because both proceed through the formation of differential oxygen concentration cells. Crevice corrosion occurs in tight spaces on a metal surface, such as under bolt heads or screw threads [5]. These tight spaces cause a differential cell to form, as the bulk of the metal is exposed to a large supply of oxygen through the atmosphere and the crevice is only exposed to a limited supply of oxygen. These tight spaces limit the diffusion of oxygen as it is consumed through the reaction given in Equation 1.5. Thus, the metal exposed to lower oxygen concentrations has a more negative potential compared to the bulk surface. This difference, while typically small, is enough to initiate corrosion and results in a deepening of the crevice [5].

SCC is a process known to occur on many metals in a range of environments [6]. This process can be broken into two general stages, initiation of a fracture and propagation of the crack, and is induced through a mixture of corrosive attack and mechanical stresses. This process begins with the passive oxide layer of the metal experiencing localized damage from either mechanical damage or chemical attack by aggressive ions (*e.g.*, $Cl^-$ or $I^-$) [5]. This damaged oxide layer allows for corrosion to occur deeper into the metal and forms a pit within it.

The formation of this pit causes a localized mechanical weakening of the material, which leads to the initiation of a crack into the bulk metal. Hydrogen,

available as a bi-product of the cathodic reaction and within the aqueous environment, is subsequently absorbed in the region near the tip of the crack, resulting in hydrogen embrittlement and reduction in the ductility of the metal at the tip [5]. This embrittlement, in addition to the environmental mechanical stresses, causes the crack to propagate further, restarting the process. This process is illustrated in Figure 1.2.

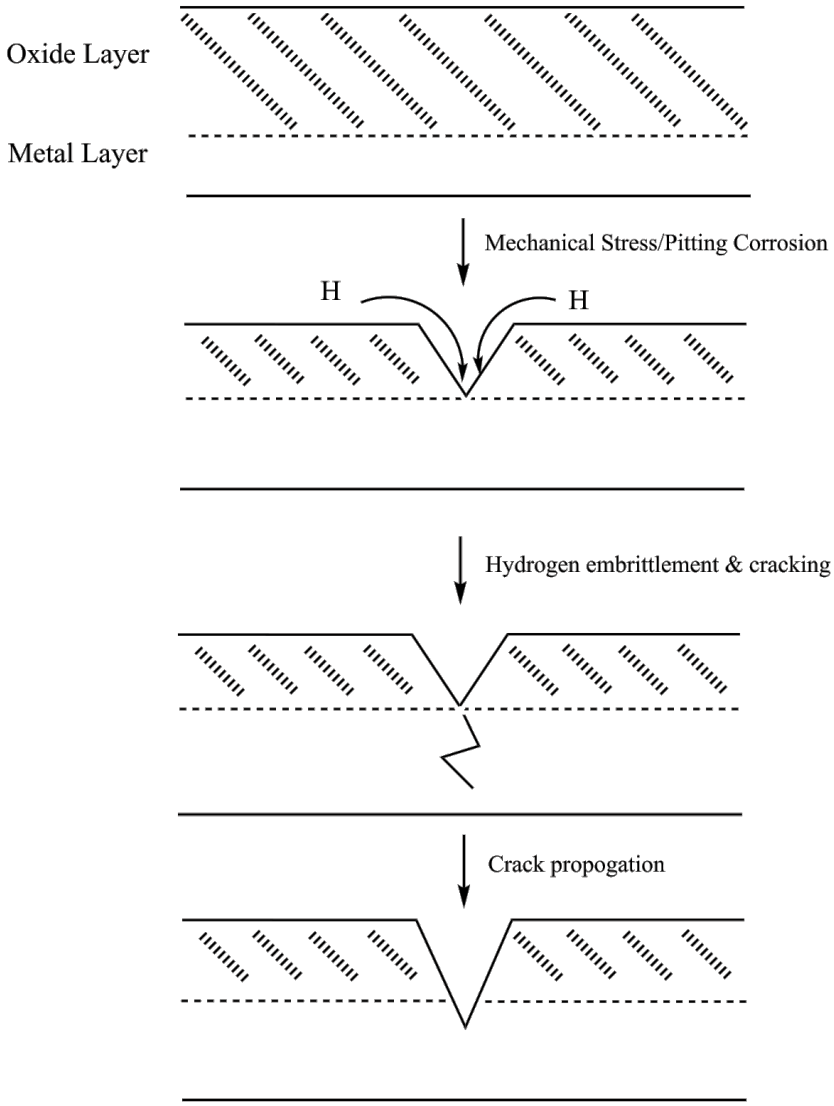


FIGURE 1.2: General mechanism of Stress Corrosion Cracking. Adapted from [5].

The final localized corrosion mechanism that will be discussed is galvanic corrosion. While SCC and pitting were similar initially in their mechanism, galvanic corrosion follows a different process. Rather than occurring through

the reaction between a metal and the aqueous environment, galvanic corrosion occurs when two dissimilar metals are in physical contact with one another or when connected by an external metal pathway in an aqueous electrolyte [5]. The latter is an unusual occurance. In galvanic corrosion the two metals act together as an electrochemical cell, with one being the cathode and the other being the anode. The metal that acts as the cathode has a greater potential than the anode metal and is said to be the more noble (less reactive) metal. The anode metal is thereby more active and experiences corrosion [6]. This relationships between pure metal potentials can be found using the galvanic series, in Table 1.1. This type of series lists the potential of a reduction reaction for different metals and can be used for alloys. An important factor to recognize for galvanic corrosion is that as the anode metal is the material that corrodes, the reaction rate, and therefore corrosion rate, of the process is controlled by the cathode metal, particularly its surface area [6].

TABLE 1.1: Galvanic series for various metals. Recreated from [6] and zirconium data from [7].

| Metal-Metal-ion Equilibrium | Potential (25 °C) Volts VS. Standard Hydrogen Electrode |
|---|---|
| $Au^{3+} + 3e^- \rightleftharpoons Au$ | +1.498 |
| $Pt^{2+} + 2e^- \rightleftharpoons Pt$ | +1.200 |
| $Pd^{2+} + 2e^- \rightleftharpoons Pd$ | +0.987 |
| $Ag^{+} + e^- \rightleftharpoons Ag$ | +0.799 |
| $Cu^{2+} + 2e^- \rightleftharpoons Cu$ | +0.377 |
| $2H^{+} + 2e^- \rightleftharpoons H_2$ | 0.000 |
| $Sn^{2+} + 2e^- \rightleftharpoons Sn$ | -0.136 |
| $Ni^{2+} + 2e^- \rightleftharpoons Ni$ | -0.250 |
| $Co^{2+} + 2e^- \rightleftharpoons Co$ | -0.277 |
| $Fe^{2+} + 2e^- \rightleftharpoons Fe$ | -0.440 |
| $Cr^{3+} + 3e^- \rightleftharpoons Cr$ | -0.744 |
| $Zn^{2+} + 2e^- \rightleftharpoons Zn$ | -0.763 |
| $Zr^{4+} + 4e^- \rightleftharpoons Zr$ | -1.450 |
| $Al^{3+} + 3e^- \rightleftharpoons Al$ | -1.662 |
| $Mg^{2+} + 2e^- \rightleftharpoons Mg$ | -2.363 |

### 1.1.3 Corrosion Mechanisms of Zirconium Alloys

The preceding list of corrosion mechanisms is not a comprehensive list of all possible mechanisms. Each of these mechanisms has been observed to occur in some fashion under reactor conditions for zirconium alloys. Some other notable types of corrosion are shadow corrosion, nodular corrosion, and corrosion due to LiOH.

Shadow corrosion is a type of enhanced corrosion of Zircaloy that occurs in boiling water reactors (BWR), under both irradiation and oxidative coolant conditions [8]. Shadow corrosion occurs when Zircaloy is near to or in contact with another metal or alloy which is more noble than Zircaloy. This corrosion is localized and mirrors the shape of the other metal/alloy, as if it were a shadow [9] and can be seen in Figure 1.3.

There have been multiple suggested mechanisms for shadow corrosion,

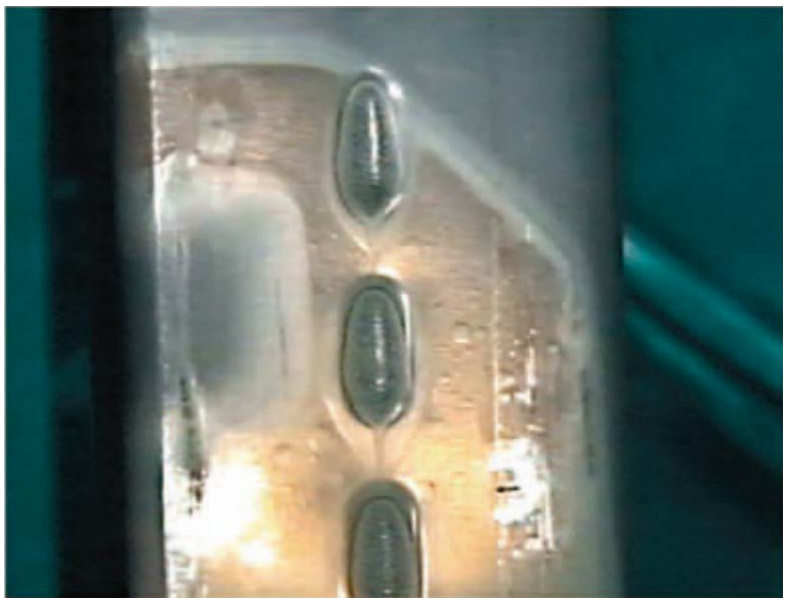

FIGURE 1.3: Shadow corrosion on a BWR fuel channel as a result of a close proximity stainless steel control rod handle. Taken from [8].

such as crevice corrosion and galvanic corrosion. However, neither of these mechanisms fully explain the occurrence of shadow corrosion [10, 11]. For crevice corrosion the distance between the metallic components which make up the crevice are typically only on the scale of tens of nanometers, whereas the gaps seen in shadow corrosion range from a fraction of a millimeter to a few millimeters [9]. Galvanic corrosion does not fully explain this either as galvanic corrosion requires some sort of contact between the anodic and cathodic metals.

There has been a mechanism proposed more recently by *Ramasubramanian* [9], which further explain this seemingly galvanic corrosion process. This proposed mechanism suggests that the galvanic corrosion occurs only in the presence of irradiation and happens through a galvanic coupling of the two surfaces by a proton transport current. This current is generated by complimentary redox reactions of $H_2O_2$ generated from the irradiation. Oxidation of $H_2O_2$ occurs on the more noble metal surface and a reduction reaction of the resulting products occurs on the Zircaloy surface [9]. This mechanism has been further studied by *Wang et al.* [12] through experimental testing and provided further evidence that this is the governing mechanism of

shadow corrosion.

Nodular corrosion occurs through a galvanic corrosion mechanism and is known to occur in BWRs and out-of-pile at temperatures >773 K. In nodular corrosion the zirconium matrix of the alloy is galvanically coupled with the secondary phase particles (SPP) that result from irradiation [11, 13]. These SPPs are nobler than the zirconium matrix and act as the cathodes for the reduction reaction, promoting further oxidation of the surrounding zirconium [11]. Nodular corrosion is seen to be dominant when these SPPs are larger and widely spaced, while smaller (<100 nm diameter) particles that are randomly distributed result in uniform corrosion [11]. Impurities in the coolant water are also expected to be important for nodular corrosion, as impurities that enhance the water conductivity (such as aqueous metals) should enhance the galvanic effect for the SPPs and zirconium matrix [13].

Unlike the previous two mechanisms, corrosion from LiOH is a known mechanism for enhanced corrosion of Zircaloy-4 and in CANDU reactors. LiOH is used to control the pH of the coolant in CANDU reactors, with the apparent pH held between 10.2 and 10.4 [14]. However, the corrosion rate of Zircaloy-4 and Zr-2.5%Nb is known to be increased by high LiOH concentrations of >0.1 M [15] through dissolution of $ZrO_2$ [16]. This is a result of the LiOH creating pores within the protective oxide layer of the zirconium alloys, thus exposing the oxide-metal surface to further corrosion [16]. In practice, the concentration of LiOH within the coolant of CANDU reactors is actively controlled to be below this critical concentration. Even so, localized areas of high LiOH concentration can form at the alloy surface through crevice corrosion. Water within the crevice reacts with the available metal surface, raising the LiOH concentration [16], and thereby promoting further corrosion.

## 1.2 Pourbaix Diagrams

There are various mechanisms that a metal or alloy can undergo corrosion. As such, it is important to understand the corrosion properties of different metals in aqueous solutions. This understanding can be partially obtained through the use of Pourbaix diagrams.

Pourbaix diagrams, or potential/pH diagrams, are a type of predominance area diagram which was developed by Marcel Pourbaix starting in 1939. These diagrams illustrate the thermodynamically stable phases of a metal in an aqueous electrochemical system, at a given temperature, pressure, and concentration. The diagrams indicate the regions where the metal in question undergoes corrosion, where it passivates and where it is immune to corrosion. These diagrams are developed under the assumption that the system is at equilibrium, and do not provide information on the kinetics of a reaction. Lastly, it is assumed when plotting a Pourbaix diagram that the reaction products are known and that the Gibbs energy of formation for each solid and ionic species is known at conditions of interest [17].

The abscissa of a Pourbaix diagram is the pH of the aqueous solution and the ordinate is the electrochemical potential E. An example of Pourbaix diagram has been provided in Figure 1.4 for zirconium, as developed by Pourbaix [18].

As can be seen in Figure 1.4, there are three major types of solid lines that appear on Pourbaix diagrams. Horizontal lines are for equilibria reactions involving purely free electron transfer. Vertical lines are for chemical reactions. Lastly there are sloped lines, which are equilibrium reactions that involve both chemical changes and electron transfer. These lines are stability boundaries between thermodynamically stable species regions, at a given concentration of aqueous species.

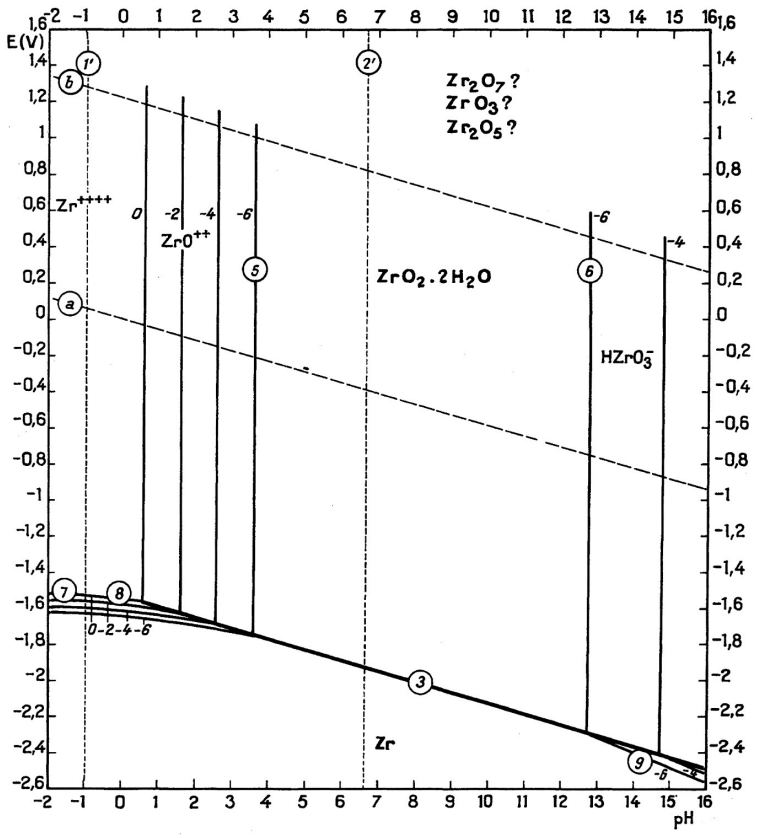


FIGURE 1.4: Pourbaix diagram for the zirconium-water system at 25 °C from the *Atlas of Electrochemical Equilibria in Aqueous Solutions* [18].

The standard Gibbs energy can be used to determine where these boundaries lie for purely chemical reactions (vertical lines), using the following equation,

$$\Delta G^\circ = -RTln(K) \tag{1.6}$$

where $\Delta G^\circ$ represents the change in the standard Gibbs energy of reaction, $R$ represents the universal gas constant, $T$ represents temperature, and $K$ represents the equilibrium constant. These lines are vertical because the chemical reaction is independent of the electrochemical potential, due to the absence of free electrons. For reactions involving only free electrons (horizontal lines), the Nernst equation can be used to determine where the boundary lines will be,

$$E = E^\circ - \frac{RT}{nF}ln(K) \tag{1.7}$$

where $E$ represents the reduction potential of the reaction in question, typically expressed on the standard hydrogen electrode scale [5]. Variables $T$ and $R$ remain the same as they are for Equation 1.6. $F$ represents Faraday's constant, and $n$ represents the number of free electrons involved in the reaction. Lastly, for equilibrium boundaries that involve both free electrons and chemical exchange, a sloped line will result and a combination of equation 1.6 and 1.7 is used. Given that,

$$\Delta G^{\circ} = -nFE^{\circ} \tag{1.8}$$

One can rearrange and substitute equation 1.8 into 1.7 for $E^{\circ}$, to obtain

$$E = -\frac{\Delta G^{\circ}}{nF} - \frac{RT}{nF} ln(K) \tag{1.9}$$

This equation can be simplified through the use of a generalized reaction equation, 1.10, and given that the reaction quotient is equal to the activity of the products over the activity of the reactants. [1]

$$rM + wH_2O \rightarrow pP + hH^+ + ne^- \tag{1.10}$$

$$E = -\frac{\Delta G^{\circ}}{nF} - \frac{RT}{nF} ln[\frac{(\alpha_P)^p(\alpha_{H^+})^h}{(\alpha_M)^r(\alpha_{H_2O})^w}] \tag{1.11}$$

The activity of hydrogen, $\alpha_C$, can be related to its concentration through equation 1.12 below, where $\gamma_C$ is the activity coefficient.

$$\alpha_C = [C] * \gamma_C \tag{1.12}$$

In an ideal dilute solution, the activity of a solute will approach its concentration and one can set the activity coefficient to be equal to one (*i.e.*, $\alpha_C \rightarrow [C]$ as $\gamma_C \rightarrow 1$). However, this is only true for an ideal solution. When conditions

[1] The generalized reaction equation is taken to be an oxidation reaction. If a reduction reaction is used as the basis, a sign flip will occur in equations 1.7, 1.8, 1.9, and 1.11.

are not ideal there will be Coulombic interactions between the ions present in solution, which affect thermodynamic properties. Systems such as aqueous metal environments often involve such interactions between metallic ions and ionic species of high concentration and result in the $\gamma$ to deviate from ideality, *i.e.*, $\gamma$ will not be one. This can be remedied if the activity coefficients of the given ions in solution are known, as one can extrapolate thermodynamic properties to the ideal dilute solution state using the activity coefficients. The activity of water will be equal to one and since the pH is equal to the negative logarithm of the hydrogen activity, Equation 1.11 becomes,

$$E = -\frac{\Delta G^{\circ}}{nF} - 2.3026\frac{RT}{nF}log\frac{(\alpha_P)^p}{(\alpha_M)^r} + 2.3026h\frac{RT}{nF}(pH) \tag{1.13}$$

There are two other distinct lines, labeled **a** and **b**, that are present in Figure 1.4. These lines show the thermodynamic stability limits of water at 298 K and 1 atm of pressure. Above the **b** line $O_2$ is stable and below the **a** line $H_2$ is stable. This results in a chemical environment that is, respectively, oxidizing and reducing. In between these two lines is the region where $H_2O$ is stable. These regions can be of particular interest when developing a Pourbaix diagram as they can be used to predict possible failure mechanisms given the aqueous conditions. For example, below the a line the evolution of hydrogen is possible, generating hydrogen atoms. Typically these hydrogen atoms will combine to form $H_2$ gas. If these hydrogen atoms instead react with the surface of a metal or transfer into the interior of the metal then these hydrogen atoms can promote stress-corrosion cracking through hydrogen embrittlement [5]. There are other types of lines present in Figure 1.4, such as heavy solid lines, light solid lines, and dashed lines. The heavy solid lines represent the boundary between two solid species. Light solid lines indicate boundaries between a solid species and an ionic species. The remaining dashed lines make up an ionic species diagram where the lines represent regions where the thermodynamic activity

of the species on each side of the line are equal [17]. Often these lines are given for a series of aqueous concentrations (*e.g.*, 1, $10^{-2}$, $10^{-4}$, and $10^{-6}$ M).

Another important thing to understand when reading a Pourbaix diagram is what the presence of each species type indicates. When the metallic form of an element is present, the material is said to be immune to corrosion for the given conditions, such as the lower section of Figure 1.4. If an aqueous species is shown to be the most prevalent species in a region, the material would actively undergo corrosion. Lastly, the presence of an oxide or hydroxide species indicates that the material is in a passivation region.

Pourbaix diagrams do not account for non-protective oxides, such as $Fe_2O_3$. In reality, the material may not be truly passivated in the given region. If not specified, Pourbaix diagrams are typically assumed to be created with a dissolved metal species concentration of $10^{-6}$ M. This value was stated by Pourbaix as the practical limit for corrosion, given the detection limits of instrumentation at the time when the *Atlas of Electrochemical Equilibria of Aqueous Solutions* was published [18]. Therefore, active corrosion is assumed to occur when the metal species concentration is greater than $10^{-6}$ M, and corrosion is considered to not occur at concentrations less than this.

### 1.2.1 Applications and Limitations of Pourbaix Diagrams

As may have been gathered from the previous section, there are many applications for Pourbaix diagrams. They can be used to understand in what conditions a metal or alloy will be resistant to aqueous uniform corrosion and to establish which metals could be expected to passivate over a wide range of pH and potential conditions. However, there are some limitations that should be known when using these diagrams. As stated previously, equilibrium is assumed in Pourbaix diagrams. This is not typical in practical applications and Pourbaix diagrams do not provide information on the rate of corrosion because

of this. Traditional Pourbaix diagrams are only made for singular elements at 25 °C and specific diagrams must be developed for cases outside this. These cases will be discussed in the following sections. Lastly, Pourbaix diagrams do not explicitly account for localized corrosion mechanisms involving chloride ions, such as pitting corrosion [5]. However, diagrams can be created including chloride species which illustrate their effect on the stability regions of the metallic species.

## 1.3 Multi-Element Pourbaix Diagrams

The construction of Pourbaix diagrams typically becomes more difficult when additional elements are incorporated. The simplest way to create such diagrams, for two metals, is to superimpose the Pourbaix diagrams of the individual metals. In all but some rare cases this will create a Pourbaix diagram that omits multiple species that would be present in reality. These rare cases are when the two metals do not form any compounds or species that contain both metals. Outside of these borderline cases, the resulting multi-metal Pourbaix diagram becomes much more complex. An example of this can be seen in Figure 1.5 where the individual Pourbaix diagram for Ni and Fe are given alongside the multi-metal diagram.

As one can gather from Figure 1.5, superimposing individual element Pourbaix diagrams does not provide a full understanding of the aqueous chemistry in more complex solutions. The superposition of the individual element diagrams does not show the presence of $NiFe_2O_4$, which is seen in the multi-element diagram.

The alternative and more encompassing method of creating a multi-element Pourbaix diagram is through Gibbs energy minimization. This method requires the appropriate thermodynamic data (standard enthalpy of formation, $\Delta H^\circ_{298\,\mathrm{K}}$, standard entropy, $\Delta S^\circ_{298\,\mathrm{K}}$, and heat capacity, $C_p$) to be available

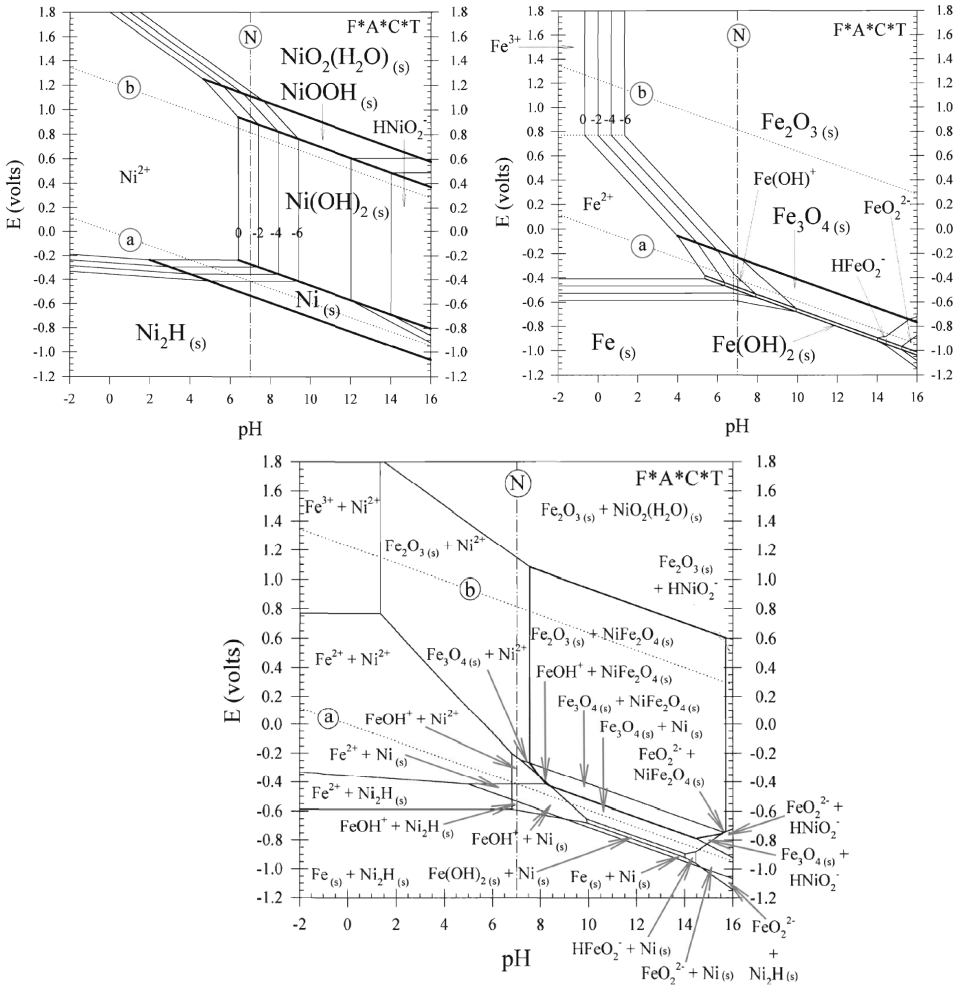


FIGURE 1.5: Pourbaix diagrams of Fe (right), Ni (left), and Ni-Fe (bottom) at 25 °C. Aqueous species concentrations range from 1 to $10^{-6}$ M for Ni and Fe [17]. The Ni-Fe diagrams has a fixed concentration of $10^{-6}$ M.

for each species, or to be estimated. This method calculates the Gibbs energy change for every reaction where the metal becomes an ionic species, compound, or remains in its metallic form [19]. Alongside the standard Gibbs energy of formation for each reactant and product being required, the activity of the metal containing species, pH, and redox potential must be known. With each reaction, for the given pH and redox potential, there will be a species or compound with the largest negative Gibbs energy change per mole of metal. This Gibbs energy change indicates which compound or species is stable for the given point on the diagram. In the case where all the Gibbs energy changes

are positive, the metal is known to be the stable species and is immune to corrosion.

Unfortunately, the required thermodynamic data are lacking for a large number of metals and their respective aqueous ions. This has resulted in many works using different methods or models to estimate the thermodynamic data. The most common of these methods is the Criss-Cobble method [20, 21], which can be used to estimate the heat capacity of ionic species in aqueous solutions.

The Criss-Cobble method follows the understanding that, at constant volume, the entropy is equal to,

$$\Delta S = \int_{T_1}^{T_2} \frac{\delta Q_H}{T} = \int_{T_1}^{T_2} \frac{\delta Q_H}{dT}\frac{dT}{T} = \int_{T_1}^{T_2} C_p(T)\frac{dT}{T} \tag{1.14}$$

where $Q_H$ represents the heat of reaction and $C_v$ is the constant volume heat capacity. Equation 1.14 can be simplified to,

$$S^\circ(T_2) - S^\circ(T_1) = C_p^\circ(T)\Big|_{T_1}^{T_2} ln\frac{T_2}{T_1} \tag{1.15}$$

Equation 1.15 can be rearranged to isolate the average heat capacity, with $T_1$ being set to 298 K [21],

$$\frac{S^\circ(T_2) - S^\circ(298)}{ln(T_2/298)} = C_p^\circ(T)\Big|_{298}^{T_2} \tag{1.16}$$

Equation 1.16 can be further simplified using the entropy Correspondence Principle that was developed by *Criss and Cobble* [20], which states: *A standard state can be chosen at every temperature such that the partial molal entropies of one class of ions at that temperature are linearly related to the corresponding entropy at some reference temperature* [20], and mathematically expressed as:

$$S^\circ_{(T_2)} = a_{(T_2)} + b_{(T_2)} S^\circ_{(T_1),(abs.)} \tag{1.17}$$

where $a$ and $b$ represent constants that are determined through experimental measurements, or through extrapolation to higher temperatures [21]. These entropy constants are given in Table 1.2, as stated by *Criss and Cobble* [21]. Additionally, the entropy at $T_1$ is the ionic entropy on the "absolute" scale [21], which is defined to be $S^{\circ}_{(abs.)} = S^{\circ}_{(conventional)} - 5.0Z$, where $Z$ is the charge of the ion.

TABLE 1.2: Entropy constants for equation 1.17 from [21] ($J \cdot mol^{-1} \cdot K^{-1}$). Values in brackets were estimated by extrapolation from lower temperatures.

| | Simple cations | | Simple anions and $OH^-$ | | Oxy anions ($XO_n^{-m}$) | | Acid oxy anions ($XO_n(OH)^{-m}$) | |
|---|---|---|---|---|---|---|---|---|
| T [°C] | $a_{(T)}$ | $b_{(T)}$ | $a_{(T)}$ | $b_{(T)}$ | $a_{(T)}$ | $b_{(T)}$ | $a_{(T)}$ | $b_{(T)}$ |
| 25 | 0 | 4.184 | 0 | 4.184 | 0 | 4.184 | 0 | 4.184 |
| 60 | 16.3 | 3.996 | -21.3 | 4.054 | -58.6 | 5.092 | -56.5 | 5.774 |
| 100 | 43.1 | 3.665 | -54.4 | 4.184 | -129.7 | 6.176 | -126.8 | 7.924 |
| 150 | 67.8 | 3.314 | -89.1 | 4.138 | -194.1 | 7.058 | (-209.2) | (9.962) |
| 200 | (97.5) | (2.975) | (126.4) | (4.104) | (-280.3) | (8.452) | (-292.9) | (12.385) |

One can substitute Equation 1.17 into Equation 1.16 to further simplify, resulting in,

$$\frac{a_{(T_2)} - S^{\circ}_{(298)}[1.000 - b_{(T_2)}]}{ln(T_2/298)} = C^{\circ}_p(T)\Big|_{298}^{T_2} \tag{1.18}$$

While this formula is useful to estimate the average ionic heat capacity, it can be used to estimate point values. By applying Equation 1.18 over smaller and smaller temperature intervals, one begins to approach the heat capacity at the mean temperature in the interval, $C^{\circ}{}_{v,T}$. This allows Equation 1.18 to be used to estimate the ionic heat capacity at 25 °C, in the form:

$$A_{(T)} + B_{(T)} S^{\circ}_{298} = C^{\circ}_{p,298} \tag{1.19}$$

The constants, $A$ and $B$, in Equation 1.19 are provided in Table 1.3.

TABLE 1.3: Heat capacity parameters at 25 °C from [21] ($J \cdot mol^{-1} \cdot K^{-1}$).

| Category of ion | A | B |
|---|---|---|
| Cations | 174.1 | -2.188 |
| $OH^-$, anions | -236.4 | 0.749 |
| Oxy anions | -607 | 9.20 |
| Acid oxy anions | -569 | 12.84 |

This allows the estimation of the heat capacity for several types of ionic species that would be seen in hydrolysis reactions. An example of this use of the Criss-Cobble method can be found in the work by *Wang et al.* [22], where a Pourbaix diagram was developed for the alloy Cr22 MPEA.

Equation 1.19 does require the entropy of the given ionic species to be known for standard conditions. This is a problem for Zircaloy-4 even at standard conditions, because there is an absence in the literature of thermodynamic data for the ionic hydrolysis species of zirconium [23]. Therefore, an additional method must be used to estimate the entropy of the ionic species. A formula was developed and published previously by *Cobble* [24] in 1953, which permits the estimation of more complex ions, such as $OH^-$ species or oxy-hydroxy species [24]. The formula is defined using the general equation for the complexation of a simple ion by ionic ligands ($O^{2-}$ and $OH^-$),

$$xM^a(H_2O)_y + zN^{-b} = M_xN_z(H_2O)^{(xa-bz)}_{(y-z)} + zH_2O \tag{1.20}$$

As found by *Powell and Latimer* and *Cobble* [24, 25], the entropy of the complex ion formation can be estimated as follows,

$$\Delta S = 49 + 16.7z - 49(z+x) - \frac{99(xa-bz)}{r_{NM}} + 270[\frac{bz}{(r_N+1)^2} + \frac{xa}{(r_M+2)^2}] \tag{1.21}$$

Here, $r_{NM}$ is equal to $r_N + r_M$, where $r_N$and $r_M$ represent the ionic radii for the anion and cation respectively [24].

Through a combination of Equations 1.18, 1.19, and 1.21, estimations of the entropy and heat capacity for ionic hydrolysis species can be obtained as needed for developing multi-element Pourbaix diagrams. These equations are only useful for charged aqueous complexes/ionic species. However, these are not the only type of aqueous species one can expect in solution, as non-ionic species can exist in solution due to hydration effects. For these aqueous species, the Helgeson-Kirkham-Flowers (HKF) model can be used [26]. The HKF model was revised in 1988 by *Tanger and Helgeson* [27] to allow for the estimation of standard partial molal thermodynamic properties of aqueous species up to 5 kbar and 1000 °C [27]. The equations of state were developed on the assumption that all standard partial molal properties of electrolytes and ions are sums of structural and solvation contributions [28]. These equations were extended to include neutral species by *Shock et al.* [26]. The particular equation of interest for this work is the equation for estimating the heat capacity, accounts for the non-solvation and solvation contributions. This equation can be directly applied when estimating the heat capacity for aqueous species. The contribution for non-solvation effects can be calculated using the formula:

$$\Delta_n C_p^\circ = c_1 + \frac{c_2}{(T-\Theta)^2} - (\frac{2T}{(T-\Theta)^3})[a_3(P-P_r) + a_4 ln\frac{\Phi+P}{\Phi+P_r}] \tag{1.22}$$

where $c_1$, $c_2$, $a_3$, and $a_4$ represent experimentally determined species-dependent non-solvation parameters. $\Phi$ and $\Theta$ represent solvation parameters equal to 2600 bar and 228 K, respectively. Lastly, $P_r$ is the reference pressure of 1 bar [29]. The contribution to the heat capacity from the solvation of the species in solvent can be calculate as,

$$\Delta_s C_p^\circ = \omega_e T X \tag{1.23}$$

where $\omega_e$ is the effective Born coefficient and $X$ is the Born function. These are defined here:

$$\omega_e = \frac{Z_e^2 * \eta}{r_e} \tag{1.24}$$

$$X = \frac{1}{\epsilon_w}\left[\left(\frac{\delta^2 ln(\epsilon_w)}{\delta T^2}\right)_P - \left(\frac{\delta ln(\epsilon_w)}{\delta T}\right)_P^2\right] \tag{1.25}$$

For Equation 1.24, $Z_e$ represents the effective charge, $r_e$ represents the effective electrostatic radius of the species, and $\eta$ represents a dimensional constant equal to $6.946\,57 \times 10^5\,\text{Å} \cdot \text{J} \cdot \text{mol}^{-1}$ [29]. $\epsilon_\text{w}$ in Equation 1.25 represents the temperature function for the dielectric constant of water.

Typically, the heat capacity would be evaluated using the combination of Equations 1.22 and 1.23. However, only the solvating contributions will be used in this work to predict the heat capacity of neutral aqueous species. This is due to the presence of the several experimentally derived parameters in Equation 1.22 and the fact that the solvating contributions are dominant at high temperatures and lower pressures [27, 30]. Therefore, the more simplistic Equation 1.23 will be used in this work to predict the heat capacity of uncharged aqueous species.

With these methods, one should be able to generate an estimate for a multi-element Pourbaix diagram. However, further work must be done to be able to generate this diagram at elevated temperatures.

## 1.4 Elevated Temperature Pourbaix Diagrams

As stated in the previous section, the Gibbs energy is the factor that dictates the dominant species for the given conditions in solution. The Gibbs energies of formation and mixing have been found for many molecules and compounds at standard conditions, but not for elevated temperatures. To solve this problem when making Pourbaix diagrams one must do one of two things, make empirical measurements at the desired temperature or extrapolate

from standard conditions to that temperature. The Gibbs energy for a given temperature can be calculated using enthalpy, $H$, and entropy, $S$,

$$G_T = H - TS \tag{1.26}$$

Differentiating Equation 1.26 gives,

$$dG = dH - dTS - TdS \tag{1.27}$$

The Gibbs energy, Equation 1.27, will simplify into the two following equations, for an isothermal step and isobaric step respectively.

$$dG_T = dH_T - TdS_T \tag{1.28}$$

$$dG = VdP - SdT \tag{1.29}$$

Equation 1.29 can be simplified further by evaluating it at a constant temperature.

$$(\frac{\partial G}{\partial P})_T = V \tag{1.30}$$

Combining Equations 1.28 and 1.30 gives the overall expression for the Gibbs energy at the new conditions.

$$G_T^P = H_T^{P_{std}} - TS_T^{P_{std}} + \int_{P_{std}}^{P} V_T dP \tag{1.31}$$

This equation allows extrapolation from a reference condition to a higher temperature. However, the enthalpy and entropy will not be constant; they will change with the temperature, in relation to the heat capacity.

$$H_T = H_{std} + \int_{T_{std}}^{T} C_p dT \tag{1.32}$$

$$S_T = S_{std} + \int_{T_{std}}^{T} \frac{C_p}{T} dT \tag{1.33}$$

Equations 1.32 and 1.33 can be substituted into Equation 1.31. The *VdP* factor can be ignored at hydrostatic pressures lower than 100 atm for aqueous species, as this factor is small enough to be incorporated into the uncertainty of the other variables [17].

$$G_T^\circ = H_{std} + \int_{T_{std}}^{T} C_p dT - T\left(S_{std} + \int_{T_{std}}^{T} \frac{C_p}{T} dT\right) \tag{1.34}$$

One can simplify Equation 1.34 by remembering that the Gibbs energy is equal to *H - TS*. Therefore Equation 1.34, at a standard state of $T$ = 298 K becomes,

$$G_T^\circ = G_{298}^\circ + \int_{T_{std}}^{T} C_p dT - T\int_{T_{std}}^{T} \frac{C_p}{T} dT \tag{1.35}$$

Using Equation 1.35, and the heat capacities, which are either reported through literature, or estimated using the Criss-Cobble or the HKF model, it is possible to determine the Gibbs free energy of a hydrolysis species at elevated temperatures. The next chapter will review previous works where both the Criss-Cobble and HKF models were used to develop Pourbaix diagrams, alongside the available thermodynamic data for the hydrolysis species of zirconium, tin, and chromium.

## 1.5 Objective

There are three main objectives of this work: to investigate the aqueous corrosion and corrosion species of zirconium and Zircaloy-4 up to 373.15 K; to fill in the knowledge gap of thermodynamic data for zirconium above standard conditions; and to develop Pourbaix diagrams up to 373.15 K for zirconium and Zircaloy-4 using this newfound data.

The first two objectives are completed through in-situ measurements of the solution pH and oxidation-reduction potential (ORP) at 373.15 K, for submerged zirconium and Zircaloy-4 samples, alongside aqueous metal concentration measurements. This allows for the determination of hydrolysis constants and Gibbs energy of formation values for aqueous zirconium species. The third objective is completed using the thermochemical modelling software FactSage [31] to calculate the Pourbaix diagrams.

# Chapter 2

# Literature Review

## 2.1 Thermodynamic Data for Zirconium, Tin, and Chromium

The development of Pourbaix diagrams for zirconium and Zircaloy-4 requires an understanding of the possible hydrolysis species that may exist for the metals in question, followed by the aggregation of the necessary thermodynamic properties for the different metal-$H_2O$ systems involved.

For zirconium the first part is relatively simple since the only system involved is Zr-$H_2O$. For Zircaloy-4 there are multiple metals present, with the nominal composition being Zr - 1.5wt%Sn - 0.2wt%Fe - 0.1wt%Cr [32]. To properly model the composition of Zircaloy-4, one should account for the hydrolysis species from the Zr-$H_2O$, Sn-$H_2O$, Fe-$H_2O$, and Cr-$H_2O$ systems. Three of these four systems will be considered in this work, with the Fe-$H_2O$ system being omitted due to technical limitations which will be outlined later.

The Zr-$H_2O$ system will be the first outlined here since the element is a focus for both diagrams.

### 2.1.1 Thermodynamic Data of the Zr-$H_2O$ System

There are many possible hydrolysis species of zirconium, which have been found or predicted, some of which exist as mononuclear species while others

can exist as polynuclear and polymeric species [23, 33].

The mononuclear hydrolysis species will typically exist in an equilibrium reaction, which can be generalized as,

$$Zr^{4+} + qH_2O \rightleftharpoons Zr(OH)_q^{4-q} + qH^+ \tag{2.1}$$

From Equation 2.1, various hydroxide species would be expected. A confirmation of these species is the evidence of $ZrOH^{3+}$ obtained through potentiometric measurements, solvent extraction methods, and solubility studies, alongside $Zr^{4+}$, $Zr(OH)_2{}^{2+}$, and $Zr(OH)_{4\,(aq)}$ [23, 34, 35]. The presence of these species has been further corroborated by multiple sources [36–38]. Additionally, the work by *Kobayashi et al.* [35] found $Zr^{4+}$, $ZrOH^{3+}$, and $Zr(OH)_{4\,(aq)}$ to be the dominant soluble species from $ZrO_2$, particularly at pH < 2, where the contribution of $ZrOH^{3+}$ and $Zr(OH)_2{}^{2+}$ were found to be negligible [35].

While these species are known to be present in aqueous solution, there is not unanimous agreement on the nature and predominance of these species. This can be clearly seen in the mass review published by the Nuclear Energy Agency (NEA) on the chemical thermodynamics of zirconium [23]. This uncertainty arises because some studies were performed in conditions that may favour the formation of polymeric species. This is further complicated due to their slow polymerization kinetics causing difficulties in identification of stable species [23]. The formation of these polymeric species is partially dependent on the concentration of zirconium in solution, with monomeric species being dominate at concentrations between $10^{-4}$–$10^{-6}$ M [33, 35]. However, the polymeric species of zirconium will be omitted in this work as the zirconium concentration is not expected to exceed $10^{-6}$ M, due to the low solubility of $ZrO_2$ and Zircaloy-4. Outside these polymeric species, there is an additional monomeric species, $Zr(OH)_6{}^{2-}$, which was been found in highly alkaline media

by *Sheka and Pevzner* [39]. Activity coefficients and the equilibrium constant for this species were not determined at the time due to the possible influence on the zirconium solubility by the presence of carbonate in solution. A later work by *Ekberg et al.* [34] was able to effectively exclude $CO_2$, and by extension carbonate, which suggested the existence of $ZrO_3^{2-}$. These two species are believed to be analogous to one another, as $Zr(OH)_6^{2-}$ would be a hydrated form of $ZrO_3^{2-}$ (*i.e.*, $ZrO_3^{2-}\cdot 3H_2O$). Therefore the present literature data for these species will be arbitrarily taken in terms of $Zr(OH)_6^{2-}$, as has been done previously [23].

The hydrolysis constants and standard Gibbs energy of formation, at standard conditions, for these stated species have been aggregated and presented in Table 2.1. The heat capacity is not available in the literature for all species. These missing data were estimated instead using the HKF model and Criss-Cobble method described in Section 1.3. The heat capacity of $Zr(OH)_4$ was taken to be equal to that of $ZrO_2$ as they are structurally similar. $Zr(OH)_4$ can also be given as a hydrated form of $ZrO_2$ (*i.e.*, $ZrO_2\cdot 2H_2O$).

TABLE 2.1: Thermodynamic data for zirconium hydrolysis species. Values obtained from [23] or calculated using the Criss-Cobble method [21] or HKF model [29].

| Species | $\Delta G_f^\circ$ $(kJ/mol)$ | $log(K)$[a] | $C_{p_{25^\circ C}}$ $(J\cdot mol^{-1}\cdot K^{-1})$ | $C_{p_{100^\circ C}}$ $(J\cdot mol^{-1}\cdot K^{-1})$ |
|---|---|---|---|---|
| $ZrO_{2\ (s)}$ | $-1042.7$ $\pm 1.3$ | $-7.0$ $\pm 1.6$ | 55.96 | 63.74 |
| $Zr(OH)_{4\ (s)}$ | $-1495.6$ $\pm 9.2$ | $-3.24$ $\pm 0.10$ | 55.96 | 63.74 |
| $Zr(OH)_{4\ (aq)}$ | $-1464.6$ $\pm 13.4$ | $-2.19$ $\pm 1.70$ | 8.53 [b] | 5.88 [b] |
| $Zr^{4+}$ | $-528.5$ $\pm 9.2$ | $-7.0$ $\pm 1.6$ | 474.39[c] | 509.17[c] |
| $Zr(OH)^{3+}$ | $-767.5$ $\pm 9.3$ | 0.32 $\pm 0.22$ | 181.24[c] | 199.57[c] |
| $Zr(OH)_2^{2+}$ | $-1008.3$ $\pm 11.0$ | 0.98 $\pm 1.06$ | -12.02[c] | -4.55[c] |
| $Zr(OH)_6^{2-}$ | $-1785.8$ $\pm 10.1$ | $-29.0$ $\pm 0.7$ | 1148.23[c] | 1530.95[c] |

[a] The hydrolysis constant ($\log\beta$) is for hydrolysis species, while the equilibrium constant is for solid species.

[b] Heat capacities calculated using the Helgeson-Kirkham-Flower Model

[c] Heat capacities calculated using the Criss-Cobble Method

The entropy and enthalpy of formation can be relatively trivial to obtain for elements with well known and studied hydrolysis species. However, this becomes more complex for hydrolysis species of zirconium. For solid species and $Zr^{4+}$, the information is readily available. For the other hydrolysis species,

the entropy of formation is not typically provided. For all hydrolysis species, except $Zr(OH)_6^{2-}$, the enthalpy of formation was obtained from *Brown et al.* [23]. The entropy values were back-calculated from the Gibbs energy of formation and the enthalpy, using the general formula,

$$S^{\circ}_{m,\text{Zr species}} = \frac{\Delta_f H^{\circ}_{m,\text{Zr species}} - \Delta_f G^{\circ}_{m,\text{Zr species}}}{T} + \sum S^{\circ}_{m.\text{reactants}} - \sum S^{\circ}_{m,\text{non-Zr products}} \quad (2.2)$$

For $Zr(OH)_6^{2-}$, neither the entropy nor enthalpy values have been provided through experimental measurements. The values used in this work were calculated instead by *Shock et al.* using the HKF model [40]. These values are provided in Table 2.2. The heat capacity values provided in Table 2.3 are given at 298.15 K and all zirconium species accounted for in this work are provided.

TABLE 2.2: Entropy and enthalpy of formation values at 298.15 K for zirconium species. Enthalpy and entropy values taken from *Brown et al.* [23] for all species, except $Zr(OH)_6^{2-}$ [40].

| Species | $\Delta H^{\circ}_{298.15\,K}$ $(J{\cdot}mol^{-1})$ | $S^{\circ}_{298.15\,K}$ $(J{\cdot}\,mol^{-1}{\cdot}\,K^{-1})$ |
|---|---|---|
| $ZrO_{2\,(s)}$ | -1100600 | 50.190 |
| $Zr(OH)_{4\,(s)}$ | -1662200 | 151.40 |
| $ZrH_{(s)}$ | -84400 | 38.3 |
| $ZrO_{2\,(g)}$ | -290000 | 273.7 |
| $ZrO_{(g)}$ | 56000 | 227.6 |
| $ZrH_{(g)}$ | 516300 | 216.2 |
| $Zr(OH)_{4\,(aq)}$ | -1628900 | -769.15 |
| $Zr^{4+}$ | -608500 | -491 |
| $Zr(OH)^{3+}$ | -800000 | -530.06 |
| $Zr(OH)_2^{2+}$ | -1064200 | -538.25 |
| $Zr(OH)_6^{2-}$ | -1394527 | -136.9 |

TABLE 2.3: Heat capacity coefficients of zirconium species, for 298.15 K. Values for non-aqueous species are taken from *Brown et al.* [23]. The heat capacity of the aqueous species were estimated using the Criss-Cobble method.

| Species | $C_p = a + bT + cT^2 + dT^{-2}$ ($J \cdot mol^{-1} \cdot K^{-1}$) | | | |
|---|---|---|---|---|
| | a | b | c | d |
| $ZrO_{2\,(s)}$ | -17.82 | -0.414 | 0.0005611 | 8841 |
| $Zr(OH)_{4\,(s)}$ | 69.622 | 0.007531 | 0 | -1406000 |
| $ZrH_{(s)}$ | 12.34 | 0.06 | 0 | 0 |
| $ZrO_{2\,(g)}$ | 46.1 | 0 | 0 | 0 |
| $ZrO_{(g)}$ | 30.8 | 0 | 0 | 0 |
| $ZrH_{(g)}$ | 29.7 | 0 | 0 | 0 |
| $Zr(OH)_{4\,(aq)}$ | 8.53 | 0 | 0 | 0 |
| $Zr^{4+}$ | 474.39 | 0 | 0 | 0 |
| $Zr(OH)^{3+}$ | 181.24 | 0 | 0 | 0 |
| $Zr(OH)_2{}^{2+}$ | -12.02 | 0 | 0 | 0 |
| $Zr(OH)_6{}^{2-}$ | 1148.23 | 0 | 0 | 0 |

Additional thermodynamic data are provided for auxiliary species of the Zr-$H_2O$ system, at standard conditions, in Tables 2.4 and 2.5.

TABLE 2.4: Thermodynamic data for auxiliary species. Data taken from [23].

| Species | $\Delta H^{\circ}_{298.15\,K}$ ($J \cdot mol^{-1}$) | $S^{\circ}_{298.15\,K}$ ($J \cdot mol^{-1} \cdot K^{-1}$) |
|---|---|---|
| $H_2O$ | -285830±40 | 69.950±0.03 |
| $H^+$ | 0 | 0 |

TABLE 2.5: Heat capacity values for auxiliary species. Data taken from [23], except the heat capacity of water which was taken from [41].

| Species | $C_p = a + bT + cT^2 + dT^{-2}$ ($J \cdot mol^{-1} \cdot K^{-1}$) | | | |
|---|---|---|---|---|
| | a | b | c | d |
| $H_2O$ | -203.1190 | 1.52070 | -0.0032 | 3848758 |
| $H^+$ | 0 | 0 | 0 | 0 |

### 2.1.2 Thermodynamic Data of the Sn-$H_2O$ System

Previous work has been performed to develop an elevated temperature Pourbaix diagram for tin by *Palazhchenko* [42]. To allow direct comparison, the

hydrolysis products included in this work have been chosen to match those of *Palazhchenko*. The thermodynamic data for the following species will be primarily taken from the 12th volume of the *Chemical Thermodynamics* series published by the NEA, *Chemical Thermodynamics of Tin* [43], as the review by the NEA is overall more encompassing than the work by *Palazhchenko* and was published six months after the work of *Palazhchenko*.

It is important to note that hydrolysis species of tin can be separated into two groups; those being the hydrolysis species that come from $Sn^{2+}$ and those that come from $Sn^{4+}$. The species from $Sn^{2+}$ are $SnOH^{+}$, $Sn(OH)_{2\,(aq)}$, and $Sn(OH)_3^{-}$, in addition to $Sn^{2+}$. The presence of $SnOH^{+}$ has been identified through many studies, alongside $Sn(OH)_{2\,(aq)}$ and $Sn(OH)_3^{-}$ [43–45].

It has been suggested that polynuclear species may complicate the formation of these species; an example is the trinuclear species, $Sn_3(OH)_4^{2+}$, reported by *Tobias* [46]. This species has become widely accepted as the dominating hydrolysis species at tin concentrations greater than $10^{-4}$ M [43]. *Tobias* also suggested that $Sn_2(OH)_2^{2+}$ formed as well, but the results from more recent publications showed no justification for the species [47, 48]. This conclusion was confirmed upon re-evaluation of the data reported by *Tobias* [43]. As with zirconium, the polynuclear species of tin are exempted from this work due to the expected low concentration of tin. $Sn(OH)_2$ has been found to be the primary species in the neutral pH range, but with a very low solubility [45].

For $Sn^{4+}$ the hydrolysis species, $Sn(OH)_{4\,(aq)}$, $Sn(OH)_5^{-}$, $Sn(OH)_6^{2-}$, and $Sn^{4+}$ are similar to that of $Zr^{4+}$, which is not unreasonable considering that both cations have a 4+ charge. The $Sn(OH)_6^{2-}$ had been stated by *Pourbaix* [18] to be the only stable hydrolysis species of $Sn^{4+}$, but multiple works have shown the presence of both $Sn(OH)_5^{-}$ and $Sn(OH)_6^{2-}$ [49–51]. Additionally, a solubility study by *Rai et al.* reported stability constants for these two species, and $SnOH^{3+}$ [52]. However, $SnOH^{3+}$ will not be accounted for in this analysis as there is no additional corroborating information for the $SnOH^{3+}$ species,

which is discussed by *Rai et al.* [52].

An important note when viewing the thermodynamic data for Sn is that some values were estimated, as was done for Zr. This primarily applies for the heat capacities for the $Sn^{4+}$ hydrolysis species. For $Sn^{4+}$ itself the heat capacity was set equal to that of $Sn^{2+}$, as was done by *Kaye and Thompson* [41], and *Palazhchenko* [42]. Lastly, the solubility constants for $Sn^{2+}$ and $Sn^{4+}$ were taken from *Rai et al.* [52] and *Duro et al.* [53], respectively. Values are presented in Table 2.6.

TABLE 2.6: Thermodynamic data for tin hydrolysis species. Values were obtained from [42], [43], [52], and [53]. Any unavailable data were calculated using the Criss-Cobble method [21] or HKF model [29] and have been denoted as such.

| Species | $\Delta G_f^\circ$ $(kJ/mol)$ | $log(K)$[a] | $C_{p_{25^\circ C}}$ $(J \cdot mol^{-1} \cdot K^{-1})$ | $C_{p_{100^\circ C}}$ $(J \cdot mol^{-1} \cdot K^{-1})$ |
|---|---|---|---|---|
| $SnO_{(s)}$ | $-255.4$ $\pm 0.8$ | * | 47.76 | 51.19 |
| $SnO_{2\ (s)}$ | $-516.6$ $\pm 0.2$ | * | 55.26 | 65.72 |
| $Sn(OH)_{2\ (aq)}$ | $-457.8$ $\pm 2.3$ | $-7.680$ $\pm 0.400$ | 1.83 [b] | 1.26 [b] |
| $Sn(OH)_{4\ (aq)}$ | $-944.9$ $\pm 0.7$ | $-8.060$ $\pm 0.110$ | 8.67[b] | 5.98[b] |
| $Sn^{4+}$ | 46.7 $\pm 3.9$ | $-61.80$ $\pm 0.29$ | 464.94[c] | 499.19[c] |
| $Sn^{2+}$ | $-27.4$ $\pm 0.3$ | $-2.50$ $\pm 0.50$ | 206.34[c] | 226.07[c] |
| $SnOH^+$ | $-244.4$ $\pm 2.3$ | $-3.530$ $\pm 0.400$ | -13.57[c] | 155.80[c] |
| $Sn(OH)_3^-$ | $-645.0$ $\pm 3.4$ | $-17.000$ $\pm 0.600$ | 2150.32[c] | 2962.84[c] |
| $Sn(OH)_5^-$ | $-1133.0$ $\pm 2.4$ | $-8.600$ $\pm 0.400$ | 3851.94[c] | 5170.21[c] |
| $Sn(OH)_6^{2-}$ | $-1312.6$ $\pm 1.8$ | $-18.670$ $\pm 0.300$ | 4869.67[c] | 6490.41[c] |

[a] The hydrolysis constant ($\log\beta$) is for hydrolysis species, while the equilibrium constant is for solid species.

[b] Heat capacities calculated using the Helgeson-Kirkham-Flower Model

[c] Heat capacities calculated using the Criss-Cobble Method

The enthalpy and entropy of formation are well documented for most tin hydrolysis species, with most of the accepted values in this work being taken from *Chemical Thermodynamics of Tin* or the Thermo-Chimie database [43, 54]. The values taken from Thermo-Chimie [54] were originally calculated using values from *Chemical Thermodynamics of Tin* and the equation provided by *Jackson and Helgeson* [43, 55]. Only two species, $Sn(OH)_5^-$ and $Sn(OH)_6^{2-}$, were missing. The entropy values were estimated using the Criss-Cobble method and the enthalpy value was calculated in a similar fashion to Equation 2.2, using the standard Gibbs energy reported in *Chemical Thermodynamics of Tin* [43]. These values are presented in Table 2.7. The heat capacity for each ionic species was estimated using the Criss-Cobble method and these values are provided in Table 2.8.

TABLE 2.7: Entropy and enthalpy of formation values at 298.15 K for tin species. Values taken from Thermo-Chimie and calculated using data presented in *Chemical Thermodynamics of Tin* [43, 54] for all species, except $Sn(OH)_5^-$ and $Sn(OH)_6^{2-}$, which were calculated using the Criss-Cobble method.

| Species | $\Delta H^\circ_{298.15\,K}$ $(J{\cdot}mol^{-1})$ | $S^\circ_{298.15\,K}$ $(J{\cdot}\,mol^{-1}{\cdot}\,K^{-1})$ |
|---|---|---|
| $SnO_{2\,(s)}$ | -577630 | 51.77 |
| $SnO_{(s)}$ | -284240 | 57.18 |
| $Sn(OH)_{2\,(aq)}$ | -540515 | 109.70 |
| $Sn(OH)_{4\,(aq)}$ | -1224035 | -213.33 |
| $Sn^{2+}$ | -9617 | -19.89 |
| $Sn^{4+}$ | -31511 | -472.50 |
| $SnOH^+$ | -276835 | 44.90 |
| $Sn(OH)_3^-$ | -777917 | 174.50 |
| $Sn(OH)_5^-$ | -1568553 | 1460.98 |
| $Sn(OH)_6^{2-}$ | -1853291 | 1813.40 |

TABLE 2.8: Heat capacity coefficients of tin species are given for 298.15 K. The heat capacity for each solid species was taken from [43], except $SnO_{(s)}$ which was taken from [41]. The heat capacity of the aqueous species were estimated using the Criss-Cobble method.

| Species | $C_p = a + bT + cT^2 + dT^{-2}$ ($J \cdot mol^{-1} \cdot K^{-1}$) | | | |
|---|---|---|---|---|
| | a | b (x$10^6$) | c | d (x$10^{-6}$) |
| $SnO_{2\,(s)}$* | 0.22817 | 38.118 | -424850 | 496.96 |
| $SnO_{(s)}$ | 39.9572 | 14640 | 0 | 0 |
| $Sn(OH)_{2\,(aq)}$ | 1.83 | 0 | 0 | 0 |
| $Sn(OH)_{4\,(aq)}$ | 8.67 | 0 | 0 | 0 |
| $Sn^{2+}$ | 206.34 | 0 | 0 | 0 |
| $Sn^{4+}$ | 464.94 | 0 | 0 | 0 |
| $SnOH^{+}$ | 79.43 | 0 | 0 | 0 |
| $Sn(OH)_3^{-}$ | -77.84 | 0 | 0 | 0 |
| $Sn(OH)_5^{-}$ | 3851.94 | 0 | 0 | 0 |
| $Sn(OH)_6^{2-}$ | 4869.67 | 0 | 0 | 0 |

* Complete heat capacity formula is $C_p = a + bT + cT^2 + dT^{-2} + eT^{-1} + fT^3$, where e = 25506000 and f = 32586.

### 2.1.3 Thermodynamic Data of the Cr-$H_2O$ System

Multiple elevated temperature Pourbaix diagrams have been developed previously for chromium, primarily by *Beverskog and Puigdomenech* for 100 °C, 200 °C, and 300 °C [56]. Similar work [57] has been performed more recently for the Cr-$H_2O$ system at high-subcritical and low-supercritical conditions, which built off the work by *Beverskog and Puigdomenech*.

In the work by *Beverskog and Puigdomenech* [56], a total of 10 aqueous chromium species were considered as well as six solids. This number of hydrolysis species may seem to be large when compared to the Zr-$H_2O$ and the Sn-$H_2O$ systems, but chromium is known to have many hydrolysis species. For example, *Beverskog and Puigdomenech* only chose to include sixteen of forty potential species [56]. This abundance comes from chromium having three stable and common oxidation states in aqueous solutions, 2+, 3+, and 6+, though Cr(II) tends to be easily oxidized by oxygen to Cr(III) [56]. Additional reasons for exclusion include specific species being unstable in equilibrium with aqueous solutions, thermodynamic instability with respect to other

included species, and the requirement for high chromium concentrations for the formation of polynuclear species.

For the chromium species, *Beverskog and Puigdomenech* were able to aggregate the required thermodynamic data from various sources. There are a few decisions made in the work of *Beverskog and Puigdomenech* that should be noted when using the given thermodynamic data. For the solids species, the heat capacity equations for $Cr(OH)_2$ and $Cr(OH)_3$ were taken to be equal to their iron analogues, as reported in *Thermochemical Properties of Inorganic Substances* [58], as there is a lack of available literature values [56]. For $Cr(OH)_3$ the Gibbs energy of formation was calculated using the upper limit of the solubility constant proposed by *Rai et al.* [59].

For the aqueous species, the Gibbs energy values for the Cr(III) hydrolysis species $CrOH^{2+}$, $Cr(OH)_2{}^{+}$, and $Cr(OH)_3{}^{-}{}_{(aq)}$ were calculated using the equilibrium constants reported by *Rai et al.* [59]. The chromite ion was assumed by *Beverskog and Puigdomenech* to have the stoichiometry $Cr(OH)_4{}^{-}$. However, the exact stoichiometry of this ion had not been known at the time and was stated by *Beverskog and Puigdomenech* themselves that it appeared to be polynuclear in nature [56]. This ion was not included in this work because of its believed polynuclear nature. The heat capacity values for the hydrolysis products of Cr(III) were obtained by assuming that the standard heat capacity changes were the same as for the hydrolysis of Fe(III) [56].

Lastly, the Gibbs energy of formation for $H_2CrO_{4\,(aq)}$ was calculated by *Beverskog and Puigdomenech* [56], using the equilibrium constant at zero ionic strength recommended by *Baes and Mesmer* [36]. The thermodynamic data for

the chromium species are shown in Table 2.9.

TABLE 2.9: Thermodynamic data for chromium hydrolysis species at 25 °C. Heat capacity values were obtained from [56] or [60]. Solubility constants were obtained from [59, 61, 62]. The Gibbs energy of formation values were obtained from [56, 63].

| Species | $\Delta_f G^\circ$ $(kJ/mol)$ | $log(K)$[a] | $C_{p_{25°C}}$ $(J \cdot mol^{-1} \cdot K^{-1})$ | $C_{p_{100°C}}$ $(J \cdot mol^{-1} \cdot K^{-1})$ |
|---|---|---|---|---|
| $Cr_{(cr)}$ | 0.00 | * | 23.56 | 24.74 |
| $Cr(OH)_2$ | -570.824 | * | 86.31 | 98.65 |
| $Cr_2O_3$ | -1058.13 | * | 104.51 | 111.56 |
| $Cr(OH)_3$ | -864.45 | * | 92.59 | 112.86 |
| $CrO_2$ | -548.10 | * | 99.73 | 101.02 |
| $CrO_3$ | -510.45 | * | 79.12 | 92.52 |
| $Cr^{2+}$ | -146.44 | 11.00 | -11.00 | -11.00 |
| $Cr^{3+}$ | -194.56 | 9.35 | -30.00 | -30.00 |
| $CrOH^{2+}$ | -410.03 | 8.0 | 160.00 | 160.00 |
| $Cr(OH)_2{}^+$ | -606.68 | 2.3 | 340.00 | 340.00 |
| $Cr(OH)_{3\ (aq)}$ | -825.41 | -16.19 | -82.38 | -82.38 |
| $CrO_4{}^{2-}$ | -727.60 | -3.10 | -251.00 | -251.00 |
| $HCrO_4{}^-$ | -764.84 | 5.36 | -50.00 | -50.00 |
| $H_2CrO_{4\ (aq)}$ | -760.65 | 6.31 | 84.00 | 84.00 |
| $Cr_2O_7{}^{2-}$ | -1301.22 | 13.47 | -175.00 | -175.00 |

[a] The hydrolysis constant ($\log\beta$) is for hydrolysis species, while the equilibrium constant is for solid species.

There have been other works outside of *Beverskog and Puigdomenech*, which tabulate thermodynamic data for chromium hydrolysis species. The review by *Dellien et al.* [63] aggregated experimentally determined thermodynamic properties for a large number of chromium species, both aqueous and otherwise. However, heat capacity is not a property considered in this review. The review by *Dellien et al.* lacked thermodynamic information for the species $Cr(OH)_{3\,(aq)}$, $Cr(OH)_{3\,(s)}$, and $Cr(OH)_{2\,(s)}$. The required data for these species were obtained instead using the Thermo-Chimie thermodynamic database [54].

In summary, the values of the Gibbs energy of formation were primarily taken from *Dellien et al.* [63], whereas the heat capacities were taken from *Beverskog and Puigdomenech* [56], with the exception of $Cr(OH)_{3\,(aq)}$, which was obtained from [60].

The standard enthalpy and entropy of formation tend to be even more well documented for chromium species than their tin counterparts. All values for the enthalpy and entropy of chromium hydrolysis species were obtained from the review by *Dellien et al.* [63]. The heat capacities were taken directly from the work of *Beverskog and Puigdomenech* [56] or from the Thermo-Chimie thermodynamic database [54]. The values of all chromium species accounted for in this work are presented in Tables 2.10 and 2.11, for both solid and aqueous species.

TABLE 2.10: Entropy and enthalpy of formation values at 298.15 K for chromium species. Enthalpy and entropy values taken from *Dellien et al.* for all species [63].

| Species | $\Delta H^{\circ}_{298.15\,K}$ $(J{\cdot}mol^{-1})$ | $S^{\circ}_{298.15\,K}$ $(J{\cdot}\ mol^{-1}{\cdot}\ K^{-1})$ |
|---|---|---|
| $Cr_{(s)}$ | 0 | 23.8 |
| $CrO_{2\,(s)}$ | -598312 | 54.39 |
| $CrO_{3\,(s)}$ | -589526 | 66.94 |
| $Cr_2O_{3\,(s)}$ | -1139722 | 81.17 |
| $Cr(OH)_{2\,(s)}$ | -653814 | 81.1 |
| $Cr(OH)_{3\,(s)}$ | -993239 | 95.4 |
| $Cr(OH)_{3\,(aq)}$ | -954285 | 95.1 |
| $Cr^{2+}$ | -143511 | -100.42 |
| $Cr^{3+}$ | -238488 | -317.98 |
| $CrOH^{2+}$ | -481160 | -175.73 |
| $Cr(OH)_2{}^{+}$ | -736384 | -133.89 |
| $CrO_4{}^{2-}$ | -881150 | 50.21 |
| $HCrO_4{}^{-}$ | -878222 | 184.1 |
| $H_2CrO_{4\,(aq)}$ | -840984 | 292.88 |
| $Cr_2O_7{}^{2-}$ | -1490341 | 261.92 |

TABLE 2.11: Heat capacity coefficients given for 298.15 K and are taken from *Beverskog and Puigdomenech* [56] and the Thermo-Chimie database [54].

| Species | $C_p = a + bT + cT^2 + dT^{-2}$ $(J{\cdot}mol^{-1}{\cdot}K^{-1})$ | | | |
|---|---|---|---|---|
| | a | b | c | d |
| $Cr_{(s)}$ | 21.76 | 0.00898 | 0.00000226 | -86000 |
| $CrO_{2\,(s)}$ | 94.6 | 0.0172 | 0 | 0 |
| $CrO_{3\,(s)}$ | 71.76 | 0.08786 | 0 | -1674000 |
| $Cr_2O_{3\,(s)}$ | 119.37 | 0.0092 | 0 | -1565000 |
| $Cr(OH)_{2\,(s)}$ | 116.064 | 0.008648 | 0 | -2874000 |
| $Cr(OH)_{3\,(s)}$ | 127.612 | 0.041639 | 0 | -4217000 |
| $Cr(OH)_{3\,(aq)}$ | -82.38 | 0 | 0 | 0 |
| $Cr^{2+}$ | -11 | 0 | 0 | 0 |
| $Cr^{3+}$ | -30 | 0 | 0 | 0 |
| $CrOH^{2+}$ | 160 | 0 | 0 | 0 |
| $Cr(OH)_2{}^{+}$ | 340 | 0 | 0 | 0 |
| $CrO_4{}^{2-}$ | -251 | 0 | 0 | 0 |
| $HCrO_4{}^{-}$ | -50 | 0 | 0 | 0 |
| $H_2CrO_{4\,(aq)}$ | 84 | 0 | 0 | 0 |
| $Cr_2O_7{}^{2-}$ | -175 | 0 | 0 | 0 |

## 2.2 Hydrolysis Models for Zr, Sn, and Cr

As discussed above, an understanding of the possible species and their thermodynamic properties for each of the metals is important. The aqueous species that would be present depend on more than just their thermodynamic properties and the operating temperature. The chemical conditions of the solvating solution will play a key part in determining the species present and their respective quantities. Such conditions include the ionic strength and the pH of the aqueous solution.

The ionic strength is a measure of the total concentration of ions in solution, accounting for their charge, and is widely used when discussing the solubility of ionic species [64]. The expression for the ionic strength, $I$,

$$I = \frac{1}{2}\sum_i z_i^2 [C_i] \tag{2.3}$$

where $z_i$ represents the charge of the species $i$ and $C_i$ represents the concentration. This concentration can either be in mol/L or mol/kg.

One property that is dependent on the ionic strength is the activity (discussed in Section 1.2). It was stated that this activity will be equal to the concentration of a species when in an ideal dilute solution. This occurs in very dilute solutions where the ionic strength of the solution approaches zero. Equation 1.12 can be rewritten as,

$$\alpha_i = [C_i] * \gamma_i \tag{2.4}$$

Another property that is dependent on the ionic strength in solution is the equilibrium constant, and thereby the solubility of a species in solution. Typically the equilibrium constant, $K$, is defined as the concentrations of the

products over the reactants. When redefined using activities this becomes,

$$K^{\circ} = \frac{\prod_i \alpha_i}{\prod_j \alpha_j} \tag{2.5}$$

In non-ideal solutions Equation 2.5 will not be equivalent to the traditional definition of the equilibrium constant, as $\alpha$ is not equal to the concentration. This type of environment is more typical, as experiments and solubility studies are usually conducted in non-zero ionic strength solutions. This results in the need for corrections of measured equilibrium or solubility constants to the zero ionic strength constant, $K^{\circ}$, in order for proper comparisons to be performed. This can be done by combining Equations 2.4 and 2.5, resulting in Equation 2.6 where $K_{exp}$ is the traditionally defined equilibrium constant. For the dissolution reaction, $A_iB_j \rightleftharpoons iA_{(aq)} + jB_{(aq)}$, the zero ionic strength equilibrium constant will be,

$$K^{\circ} = [C_A]^i \gamma_A^i * [C_B]^j \gamma_B^j = K_{exp} * \gamma_A^i * \gamma_B^j \tag{2.6}$$

This zero ionic strength equilibrium constant can be found relatively easily when the activity coefficients for the involved species are known, or through repeated experiments to lower ionic strengths to extrapolate to zero ionic strength. However, this will only provide the overall contribution for all the ions when measured experimentally, due to the complexity of solutions.

Estimations of the activity coefficients for individual ions can be made using known semi-empirical models and equations, such as the Debye-Hückel, the extended Debye-Hückel, and the Davies equation. These three equations have been found to provide good estimates for ionic strengths up to 0.01 M, 0.1 M, and 0.5 M, respectively [64–66].

$$log(\gamma_{\pm}) = -A_{dh}|z_{-}z_{+}|\sqrt{I} \qquad \text{Debye-Hückel Equation} \tag{2.7}$$

$$log(\gamma_{\pm}) = -\frac{A_{dh}|z_{-}z_{+}|\sqrt{I}}{1 + B_{dh}a_{dh}\sqrt{I}} \qquad \text{Extended Debye-Hückel Equation} \tag{2.8}$$

$$log(\gamma_{\pm}) = -A_{dh}z_{\pm}^{2}(\frac{\sqrt{I}}{1+\sqrt{I}} - b_{d}I) \qquad \text{Davies Equation} \tag{2.9}$$

where $A_{dh}$ and $B_{dh}$ represent temperature dependent constants and have been tabulated up to 100 °C [67]. $Z$ represents the charge of the ions involved, $I$ represents the ionic strength, $a_{dh}$ represents the effective radius of the ion, and $b_d$ represents an experimentally derived constant that is typically taken to be 0.2 or 0.3. This $b_d$ term was not determined through theoretical rigor, but rather through empirical work and has been found to improve the accuracy when estimating activity coefficients. The Davies equation will be the primary equation used to estimate the activity coefficients for different ionic species for this work because of the higher upper ionic strength limit compared to the Debye-Hückel and Extended Debye-Hückel equations. Though, there are other more complex equations and models that can be used to estimate the activity coefficient at higher ionic strengths, such as the specific ion interaction (SIT) theory.

The SIT theory builds upon the Debye-Hückel theory by accounting for the individual interactions of the chosen ion with the other ions in solution that have an opposite sign charge, and their given concentrations [68]. With the equation,

$$log(\gamma_{\pm}) = -z_{j}^{2}(\frac{0.51\sqrt{I}}{1+1.5\sqrt{I}} + \sum_{k}\epsilon_{jk}m_{k}) \tag{2.10}$$

where $z$ and $I$ are the same in the SIT theory as for Debye-Hückel, $m$ represents the ion concentration in molality, and $\epsilon$ represents the interaction

coefficient. This interaction coefficient acts as a kind of correction factor to the Debye-Hückel theory. Lastly, $j$ is the species in question and $k$ is all other interacting chemical species being accounted for.

Given these equations above, these activity coefficients and equilibrium constants can be related to the hydrolysis reactions for the intended metals. Generally a hydrolysis reaction of a metal can be written as seen,

$$[M(H_2O)_n]^z \rightleftharpoons [MOH(H_2O)_{n-1}]^{z-1} + H^+ \tag{2.11}$$

with each successive reaction replacing a water molecule from the hydrated ion. This type of reaction is pH dependent due to the dependence on either hydroxide or hydrogen atoms. This dependency allows one to predict the pH regions in which individual ions will be more dominant in solution, in the form of a hydrolysis distribution plot.

### 2.2.1 Hydrolysis Model of Zr

The hydrolysis species of zirconium have been outlined previously in Table 2.1. The hydrolysis reactions of these ions are listed below, excluding any aquo ligands that would be present.

$$ZrO_{2(s)} + 4H^+_{(aq)} \rightleftharpoons Zr^{4+}_{(aq)} + 2H_2O_{(l)} \tag{2.12}$$

$$Zr^{4+}_{(aq)} + H_2O_{(l)} \rightleftharpoons Zr(OH)^{3+}_{(aq)} + H^+_{(aq)} \tag{2.13}$$

$$Zr^{4+}_{(aq)} + 2H_2O_{(l)} \rightleftharpoons Zr(OH)^{2+}_{2(aq)} + 2H^+_{(aq)} \tag{2.14}$$

$$Zr^{4+}_{(aq)} + 4H_2O_{(l)} \rightleftharpoons Zr(OH)_{4(aq)} + 4H^+_{(aq)} \tag{2.15}$$

$$Zr^{4+}_{(aq)} + 6H_2O_{(l)} \rightleftharpoons Zr(OH)^{2-}_{6(aq)} + 6H^+_{(aq)} \tag{2.16}$$

Additionally, the non-zero ionic strength solubility/hydrolysis constants will be as follows,

$$K_{Zr^{4+}} = \frac{[Zr^{4+}]}{[H^+]^4} \tag{2.17}$$

$$K_{Zr(OH)^{3+}} = \frac{[Zr(OH)^{3+}][H^+]}{[Zr^{4+}]} \tag{2.18}$$

$$K_{Zr(OH)_2^{2+}} = \frac{[Zr(OH)_2^{2+}][H^+]^2}{[Zr^{4+}]} \tag{2.19}$$

$$K_{Zr(OH)_4} = \frac{[Zr(OH)_4][H^+]^4}{[Zr^{4+}]} \tag{2.20}$$

$$K_{Zr(OH)_6^{2-}} = \frac{[Zr(OH)_6^{2-}][H^+]^6}{[Zr^{4+}]} \tag{2.21}$$

Lastly, the overall concentration of zirconium in solution will be a sum over the concentration of each aqueous species,

$$\sum[Zr] = [Zr^{4+}] + [Zr(OH)^{3+}] + [Zr(OH)_2^{2+}] + [Zr(OH)_4] + [Zr(OH)_6^{2-}] \tag{2.22}$$

This relationship for the total zirconium concentration allows the generation of a hydrolysis distribution plot where the relative percentages for the ionic species will be pH dependent. This can be done by rearranging equations 2.17 – 2.21 to isolate for the concentration of the respective ion. As can be seen in equations 2.18 – 2.21, this will result in the need for the hydrolysis constant to be known for each species and for the concentration of $Zr^{4+}$ to be calculated. The hydrolysis constants used for each species are tabulated in Table 2.1 and the concentration of $Zr^{4+}$ can be found using Equation 2.17. It is important to note that all solubility data used to generate the hydrolysis distribution plot, Figure 2.1, of zirconium is for 298.15 K.

From Figure 2.1, there are four main pH ranges where different ionic species are dominant; -1–0 pH, 0–1 pH, 3–12 pH, and 13–14 pH. In these ranges the measurements of the solubility constant of different ionic species with limited

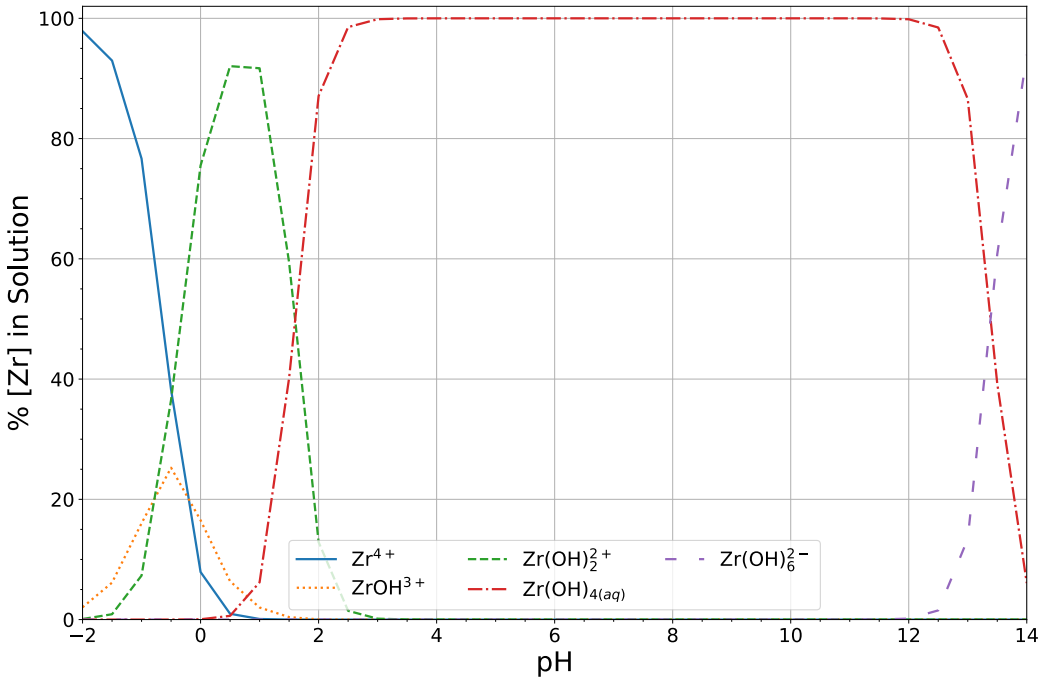


FIGURE 2.1: Hydrolysis distribution plot of Zr(IV) species at 298.15 K

interference from the other species is possible, but the range of -1–0 pH does present a region where isolation becomes difficult. At a pH of -2, $Zr^{4+}$ would be the expected dominant species. However, this extreme pH is difficult to obtain and maintain for extended periods. Therefore, the stated pH ranges of 0–1 pH, 3–12 pH, and 13–14 pH will be used to determine solubility constants of $Zr(OH)_2{}^{2+}$, $Zr(OH)_{4\,(aq)}$, and $Zr(OH)_6{}^{2-}$, respectively.

### 2.2.2 Hydrolysis model of Sn

The hydrolysis model used for tin was generated using the same method as described for zirconium, where the total concentration of tin in solution is a sum of the concentrations for each aqueous species.

$$\sum[Sn] = [Sn^{4+}] + [Sn^{2+}] + [Sn(OH)_2] + [Sn(OH)_4] + [Sn(OH)^+] + [Sn(OH)_3^-] + [Sn(OH)_5^-] + [Sn(OH)_6^{2-}] \quad (2.23)$$

Unlike the work by *Palazhchenko* [42], a singular hydrolysis plot for the species of $Sn^{2+}$ and $Sn^{4+}$ was made. Whereas *Palazhchenko* created an individual hydrolysis plot for both $Sn^{2+}$ and $Sn^{4+}$ [42]. Additionally a model was only made for 298.15 K due to solubility data limitations. The solubility constants used in this model are given in Table 2.6 in the the log(K) form.

The solubility/hydrolysis reaction equations for the Sn-$H_2O$ system are;

$$SnO_{2(s)} + 4H^+_{(aq)} \rightleftharpoons Sn^{4+}_{(aq)} + 2H_2O_{(l)} \tag{2.24}$$

$$SnO_{(s)} + 2H^+_{(aq)} \rightleftharpoons Sn^{2+}_{(aq)} + H_2O_{(l)} \tag{2.25}$$

$$Sn^{2+}_{(aq)} + H_2O_{(l)} \rightleftharpoons Sn(OH)^+_{(aq)} + H^+_{(aq)} \tag{2.26}$$

$$Sn^{2+}_{(aq)} + 2H_2O_{(l)} \rightleftharpoons Sn(OH)_{2(aq)} + 2H^+_{(aq)} \tag{2.27}$$

$$SnO_{2(s)} + 2H_2O_{(l)} \rightleftharpoons Sn(OH)_{4(aq)} \tag{2.28}$$

$$SnO_{(cr)} + 2H_2O_{(l)} \rightleftharpoons Sn(OH)^-_{3(aq)} + H^+_{(aq)} \tag{2.29}$$

$$Sn(OH)_{4(aq)} + H_2O_{(l)} \rightleftharpoons Sn(OH)^-_{5(aq)} + H^+_{(aq)} \tag{2.30}$$

$$Sn(OH)_{4(aq)} + 2H_2O_{(l)} \rightleftharpoons Sn(OH)^{2-}_{6(aq)} + 2H^+_{(aq)} \tag{2.31}$$

with their respective non-zero ionic strength equilibrium constants being:

$$K_{Sn^{4+}} = \frac{[Sn^{4+}]}{[H^+]^4} \tag{2.32}$$

$$K_{Sn^{2+}} = \frac{[Sn^{2+}]}{[H^+]^2} \tag{2.33}$$

$$K_{Sn(OH)^+} = \frac{[Sn(OH)^+][H^+]}{[Sn^{2+}]} \tag{2.34}$$

$$K_{Sn(OH)_2} = \frac{[Sn(OH)_2][H^+]^2}{[Sn^{2+}]} \tag{2.35}$$

$$K_{Sn(OH)_4} = [Sn(OH)_4] \tag{2.36}$$

$$K_{Sn(OH)^-_3} = [Sn(OH)^-_3][H^+] \tag{2.37}$$

$$K_{Sn(OH)^-_5} = \frac{[Sn(OH)^-_5][H^+]}{[Sn(OH)_4]} \tag{2.38}$$

$$K_{Sn(OH)_6^{2-}} = \frac{[Sn(OH)_6^{2-}][H^+]^2}{[Sn(OH)_4]} \tag{2.39}$$

The relationships given above can then be taken alongside Equation 2.23 to generate Figure 2.2.

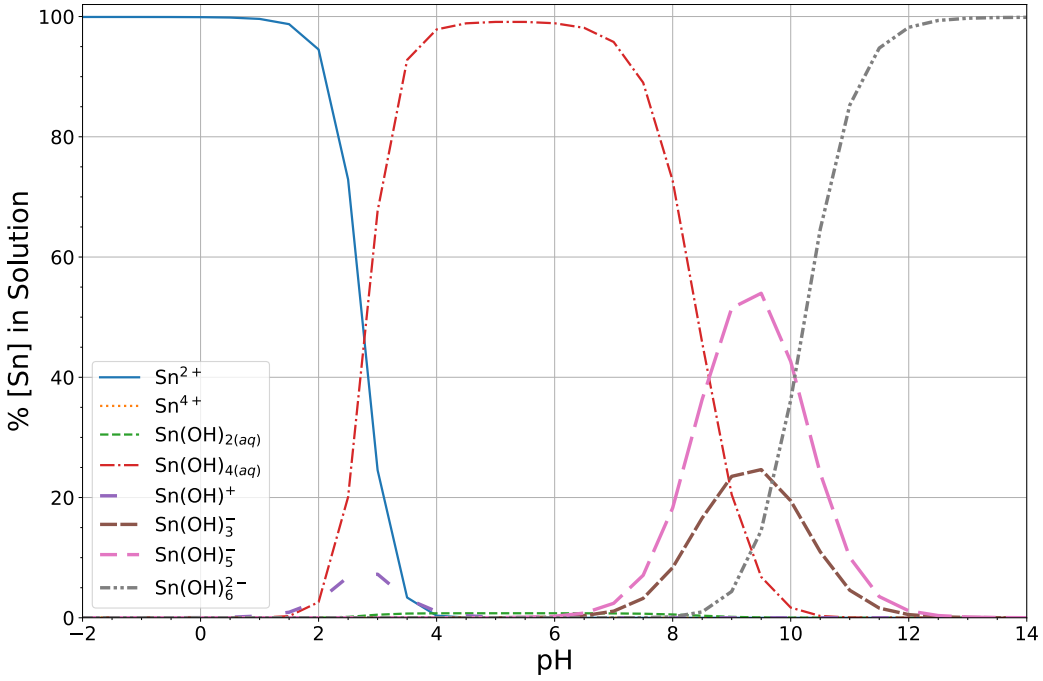


FIGURE 2.2: Hydrolysis distribution plot of Sn(IV) and Sn(II) species at 298.15 K

Unlike for zirconium, the solubility constants of the tin species cannot be directly isolated by solubility experiment measurements in the pH region with expected individual ionic species dominance. This is because the source of tin in this work is Zircaloy-4 rather than metallic tin or an oxide. This source results in the inherent possibility that other metallic hydrolysis species will be present and affect the solubility of the tin species.

### 2.2.3 Hydrolysis model of Cr

The Cr-$H_2O$ system was modelled using the equilibrium constants given in Table 2.9, in the *log(K)* form. A total of nine aqueous species were included in this model, with some being much more dominant than others. The total

aqueous concentration of chromium would be,

$$\sum[Cr] = [Cr^{2+}] + [Cr^{3+}] + [CrOH^{2+}] + [Cr(OH)_2^+] + [Cr(OH)_{3,(aq)}] + [CrO_4^{2-}] + [HCrO_4^-] + [H_2CrO_{4(aq)}] + [Cr_2O_7^{2-}] \quad (2.40)$$

For each species, the equilibrium equations are:

$$Cr(OH)_{2(s)} + 2H^+_{(aq)} \rightleftharpoons Cr^{2+}_{(aq)} + 2H_2O_{(l)} \quad (2.41)$$

$$Cr(OH)_{3(s)} + 3H^+_{(aq)} \rightleftharpoons Cr^{3+}_{(aq)} + 3H_2O_{(l)} \quad (2.42)$$

$$Cr(OH)_{3(s)} + 2H^+_{(aq)} \rightleftharpoons CrOH^{2+}_{(aq)} + 2H_2O_{(l)} \quad (2.43)$$

$$Cr(OH)_{3(s)} + H^+_{(aq)} \rightleftharpoons CrOH^{+}_{2(aq)} + H_2O_{(l)} \quad (2.44)$$

$$Cr^{3+}_{(aq)} + 3H_2O_{(l)} \rightleftharpoons Cr(OH)_{3(aq)} + 3H^+_{(aq)} \quad (2.45)$$

$$CrO_{3(s)} + H_2O_{(l)} \rightleftharpoons CrO^{2-}_{4(aq)} + 2H^+_{(aq)} \quad (2.46)$$

$$CrO^{2-}_{4(aq)} + H^+_{(aq)} \rightleftharpoons HCrO^-_{4(aq)} \quad (2.47)$$

$$CrO^{2-}_{4(aq)} + 2H^+_{(aq)} \rightleftharpoons H_2CrO_{4(aq)} \quad (2.48)$$

$$2CrO^{2-}_{4(aq)} + 2H^+_{(aq)} \rightleftharpoons Cr_2O^{2-}_{7(aq)} + H_2O_{(l)} \quad (2.49)$$

The respective non-zero ionic strength equilibrium constant equations are:

$$K_{Cr^{2+}} = \frac{[Cr^{2+}]}{[H^+]^2} \quad (2.50)$$

$$K_{Cr^{3+}} = \frac{[Cr^{3+}]}{[H^+]^3} \quad (2.51)$$

$$K_{CrOH^{2+}} = \frac{[CrOH^{2+}]}{[H^+]^2} \quad (2.52)$$

$$K_{Cr(OH)_2^+} = \frac{[Cr(OH)_2^+]}{[H^+]} \quad (2.53)$$

$$K_{Cr(OH)_3} = \frac{[Cr(OH)_3][H^+]^3}{[Cr^{3+}]} \quad (2.54)$$

$$K_{CrO_4^{2-}} = [CrO_4^{2-}][H^+]^2 \quad (2.55)$$

$$K_{HCrO_4^-} = \frac{[HCrO_4^-]}{[H^+][CrO4^{2-}]} \tag{2.56}$$

$$K_{H_2CrO_4} = \frac{[H_2CrO_4]}{[H^+]^2[CrO4^{2-}]} \tag{2.57}$$

$$K_{Cr_2O_7^{2-}} = \frac{[Cr_2O_7^{2-}]}{[H^+]^2[CrO4^{2-}]^2} \tag{2.58}$$

The preceding relations can be taken with the sum of the aqueous chromium concentrations to generate a hydrolysis distribution plot.

The hydrolysis plot, shown in Figure 2.3, which resulted from the hydrolysis and solubility coefficients given in Table 2.9 shows that there are three areas of dominance in the given pH range; less than -2 pH with $Cr^{3+}$ being the primary species, -1.5–0 for $Cr^{2+}$, and $Cr_2O_7^{2-}$ being dominant at greater than 2 pH. The individual solubility constants of the expected aqueous chromium species cannot be properly measured in this work, as aqueous species of tin and zirconium are expected to form as well during the corrosion of Zircaloy-4. This would cloud and invalidate any solubility measurements in the aqueous solution for chromium species.

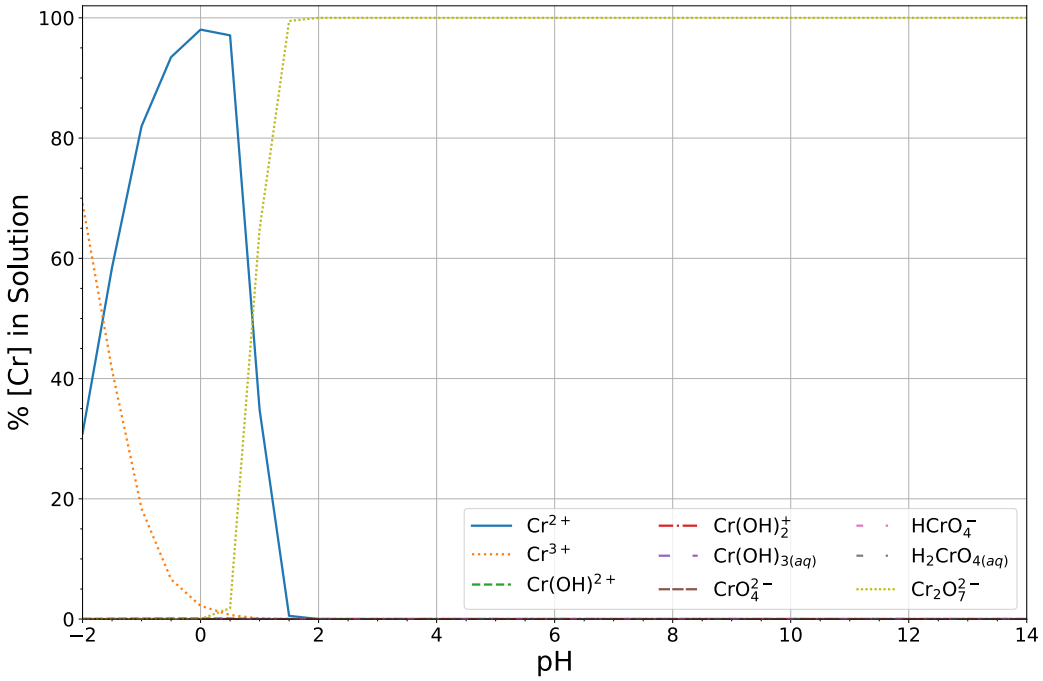


FIGURE 2.3: Hydrolysis distribution plot of Cr species at 298.15 K

## 2.3 Elevated Temperature Pourbaix Diagrams & Multi-Element Diagrams

There has been ample work performed previously to develop both elevated temperature Pourbaix diagrams and Pourbaix diagrams for engineering alloys. For example, *Wang et al.* [22], developed Pourbaix diagrams for the multi-principle element alloy (MPEA) $Ni_{38}Fe_{20}Cr_{22}Mn_{10}Co_{10}$ using the Calculation of Phase Diagram (CALPHAD) method. Unlike previously mentioned works, the method used was not the Criss-Cobble method or the HKF model. Rather, the semi-empirical model estimates the Gibbs energy, using the following equation for isobaric processes,

$$G_m^\theta - \sum_i b_i H_i^{SER} = a_o + a_1 T + a_2 T ln(T) + a_3 T^2 + a_4 T^{-1} + a_5 T^3 + ... \quad (2.59)$$

where $b_i$ represents the molar fraction of the $i$-th element and the second factor on the left hand side of the equation is the sum of enthalpies for the elements in their standard element reference (SER) state, standard conditions [22]. The coefficients on the right hand side of the equation are either determined experimentally or through first principle calculations and represent the temperature dependence of the Gibbs energy. This method allows for more precise estimations of the Gibbs energy, but it comes with the increased overhead of needing adequate experimental measurements or computational calculations in order to determine the coefficients.

This method allows estimation of the Gibbs energy for non-stoichiometric oxides by using the compound energy formulism (CEF) [22]. This differs from the Criss-Cobble and HKF models, which were not made to incorporate non-stoichiometric oxides. As can be seen in Figure 2.4, this allows the creation of very complex Pourbaix diagrams that may account for a multitude of potential species.

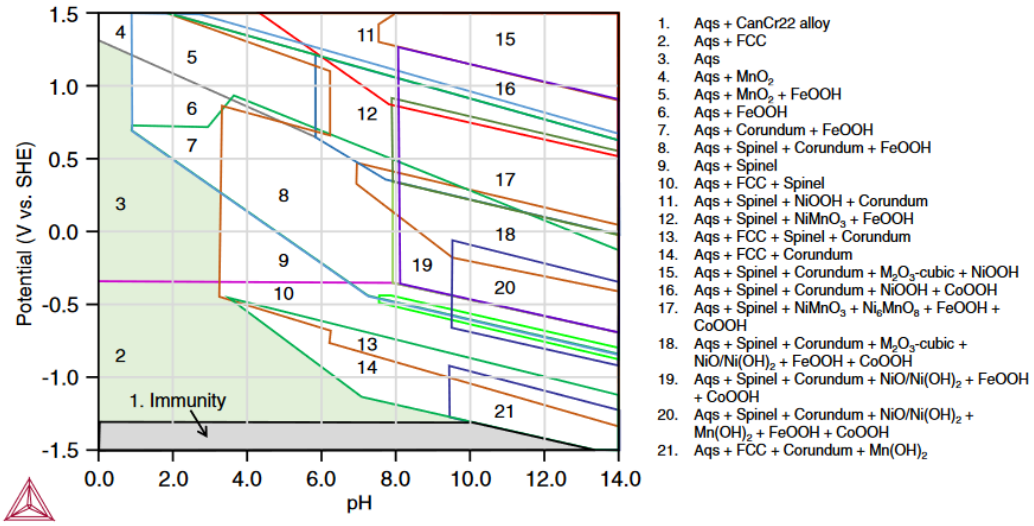


FIGURE 2.4: Pourbaix diagram of MPEA $Ni_{38}Fe_{20}Cr_{22}Mn_{10}Co_{10}$ at 25 °C from *Wang et al.*, including non-stoichiometric oxides [22].

While the CALPHAD method can be seen to be effective, it is not ubiquitous when developing multi-element or elevated temperature Pourbaix diagrams. The Criss-Cobble method and HKF model can currently be seen used in literature more often, especially for elevated temperature Pourbaix diagrams [56, 57, 69]. This may be due to the established nature of these two methods, while the CALPHAD method tends to be used in more recent publications [22, 70].

Pourbaix diagrams were developed by *Cubicciotti* for the Fe-Cr-Ni alloy system at temperatures up to typical light water reactor conditions (300 °C) [69]. The elevated temperature heat capacities for ionic species were estimated purely using the Criss-Cobble method. As can be seen in Figure 2.5 the species stability regions change with the change of temperatures.

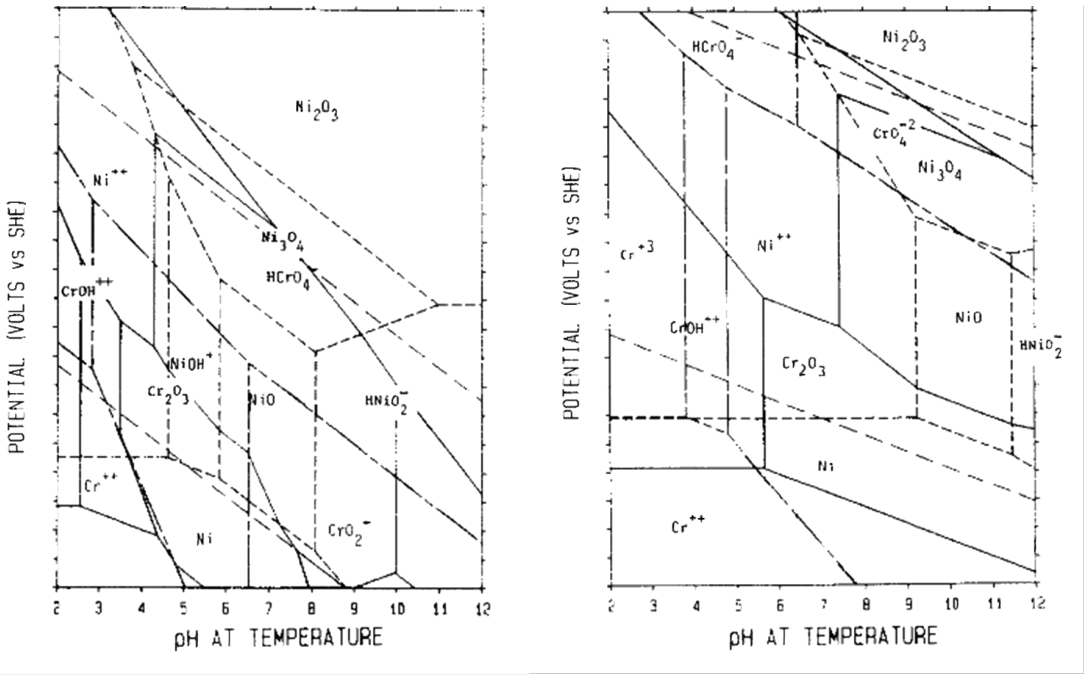


FIGURE 2.5: Pourbaix diagram of the Ni-Fe-Cr-$H_2O$ system at 25 °C (right) and 300 °C (left) from *Cubicciotti* [69].

Some works also choose to forgo the use of the Criss-Cobble method entirely and to use the HKF [27] or revised-HKF model [29] to estimate the Gibbs energy of formation for the intended species; for example, *Cook and Olive* [57] who reported Pourbaix diagrams for the Fe-$H_2O$ system at high-subcritical and low-supercritical conditions.

Overall, there are various methods used to estimate and plot the Gibbs energies to develop more complex Pourbaix diagrams, each with advantages and disadvantages. The main factor when deciding the method tends to be the availability of data and the complexity of the method.

# Chapter 3

# Materials & Experimental Methods

## 3.1 Materials and Reagents

Zirconium oxide powder, with a purity of 99%, was obtained from Sigma Aldrich. Perchloric acid (70%w/w), hydrochloric acid (36.5%w/w), and sodium hydroxide (50%w/w) solutions were used in the preparation of the experimental solutions. Distilled water was used for all tests and reactions. Thermo Scientific™ Orion™ (1.68, 12.46) and Fisher Scientific (4.00, 7.00, 10.00) pH buffer standards were used for calibration of the pH electrode. An Orion™ KI ORP standard from Thermo Scientific™ was used to calibrate the ORP electrode. An AccuTrace™ zirconium 1000 µg/mL standard and a Fisher Scientific tin 1 mg/mL standard were used for Inductively Coupled Plasma Optical Emission spectroscopy (ICP-OES) calibration. Lastly, the Zircaloy-4 sections used in this work were cut from Zircaloy-4 fuel cladding tubes, donated by BWXT NEC and the Piro group.

## 3.2 Experimental Apparatus

A bolted-closure type batch reaction vessel was used as the main experimental apparatus and is pictured in Figure 3.1. The vessel is made up of three sections, a pipe spool and two blind flanges as caps. The body and flanges of the vessel are made of 316 stainless steel and are lined with polytetrafluoroethylene

(PTFE). The body of the vessel had an inner diameter of 10.2 cm (4 inches). The total volume of the vessel was 2 L; a working volume of 1.8 L was used with a 0.2 L plenum of air. An Omega Engineering pH (PHE-5431-10) and ORP (ORE-5431-10) electrode were housed in the top blind flange, alongside a pressure gauge, as seen in Figure 3.1 b). Both electrodes were inserted and sealed into the vessel using 19 mm (0.75 inch) stainless steel Swagelok fittings and O-rings.

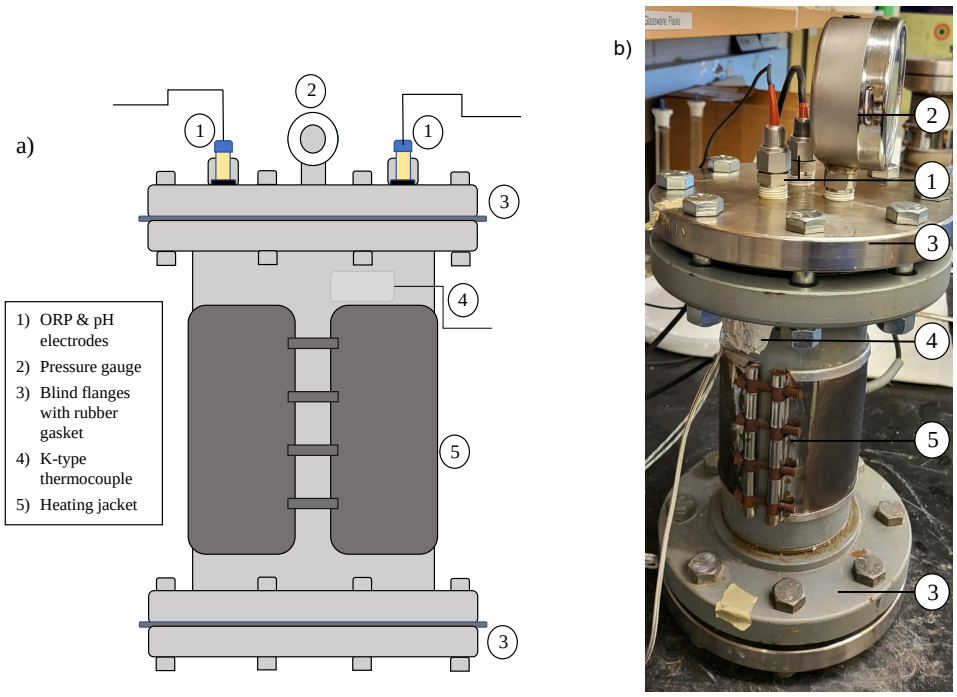


FIGURE 3.1: Diagram a) and picture b) of reaction vessel used. The numbering schemes are identical in a) and b).

The vessel was fitted with an external 900 W band heating jacket from O.E.M. heaters, which surrounded the body of the vessel to ensure even heating. The exterior temperature of the vessel was measured using a K-type thermocouple from Omega Engineering and a proportional-integral-derivative temperature controller from Love Controls.

The pH electrode was designed with a maximum operating temperature of 135 °C and pressure of 34.5 bar, with a precision of 0.1%. A double junction KCl/AgCl reference probe was housed inside a polyarylsulfone (PAS)

thermoplastic body. The ORP probe was made of the same PAS body but used a platinum indicator electrode and KCl/AgCl reference electrode, with a precision of 0.1%.

The pH and ORP of solution were continuously measured and recorded using an Orion™ Dual Star™ pH, ISE, mV, ORP, and Temperature Dual Channel Benchtop Meter. Both probes were calibrated before every experimental run using calibration methods built into the Benchtop Meter. The pH probe was calibrated using a five-point calibration process with standard buffers of 1.68, 4.00, 7.00, 10.00, and 12.46 pH. The ORP probe was calibrated using a one-point calibration process, using a potassium iodide standard with a standard potential of 420 mV vs. Standard Hydrogen Electrode ($E_H$).

## 3.3 Method

### 3.3.1 Sample Preparation of Zircaloy-4

The Zircaloy-4 samples were prepared from the polished Zircaloy-4 tubes by sectioning them into small rings. This was manually performed by placing the whole Zircaloy-4 tube into a vice and cutting them using a pipe cutter. Efforts were made to cut each ring into similar sizes by measuring and marking uniform intervals onto the tube before cutting. The rings were cleaned using ethanol and stored until further use. An example of the source tube and Zircaloy-4 samples can be seen in Figure 3.2

FIGURE 3.2: Images of the Zircaloy-4 samples used in the solubility experiments and the source cladding tube.

### 3.3.2 Preliminary Experiments

Preliminary experiments were performed for both Zircaloy-4 and zirconium to determine if/when an equilibrium was achieved for the concentration of zirconium in solution. This allowed the test duration for further experiments to be decided. Perchloric acid was used to allow determination of the concentration equilibrium without the effect of complexation, as perchloric acid is a non-complexing acid.

0.500±0.004 L of distilled water was dispensed into a 1.0 L volumetric flask, followed by 15.0±0.5 mL of perchloric acid (11.595 M). The mixture was further diluted to 1 L using distilled water, and mixed. The mixture was carefully poured into the reaction vessel and further diluted with 0.800±0.006 L of distilled water and mixed using a glass stir rod, resulting in a 0.100±0.006 M perchloric acid solution with a measured pH of 1.5±0.2, at 298.5 K. Following this, 4.54±0.10 g of $ZrO_2$ was poured into the solution and mixed. The reaction vessel was then sealed and the temperature set to 100 °C. The solution was held at 100 °C for two full days, after which the temperature was lowered to 80 °C and allowed to equilibrate for 30 mins before a 25 mL samples was taken through the ORP probe port. The ORP probe was replaced and sealed, and the temperature was returned to 100 °C. This sampling process was repeated on days 4, 6, 8, and 9 of the experiment. All aqueous samples were analyzed shortly after being taken using ICP-OES. This test process was repeated using 1.6±0.1 g of Zircaloy-4 in a 0.100±0.006 M perchloric solution and samples were taken after 2, 5, 7, and 9 days and analyzed using ICP-OES.

A separate experimental test was performed after the previously outlined test using a perchloric acid solution of the same concentration and a similar mass of $ZrO_2$, but with samples being taken at three temperatures, 80 °C, 60 °C, and 40 °C. Access limitations to the ICP-OES required samples to be taken and analyzed on days 2, 4, and 9.

### 3.3.3 General Experimental Process

The solubility experiments were completed at four pH ranges; -1–0, 0–1, 7, and 13–14. Hydrochloric acid was used to create the acidic solutions and sodium hydroxide for the alkaline solution. Solely distilled water was used to create the neutral solutions. Solutions were prepared in the same manner as performed in the preliminary tests, with the approximate volumes and concentrations for each solution being given in Table 3.1. Each experimental run for zirconium followed the same general process given below.

TABLE 3.1: Volumes and concentration of pH adjusting compounds for all pH ranges other than pH 7.

| Compound | Approximate volume (mL) | Concentration (M) | pH range |
|---|---|---|---|
| Hydrochloric acid | 450.0±0.2 | 3.050±0.010 | -1–0 |
| Hydrochloric acid | 75.0±0.1 | 0.510±0.002 | 0–1 |
| Sodium hydroxide | 30.0±0.6 | 0.320±0.006 | 13–14 |

The prepared 1 L solution was poured into the reaction vessel and diluted using 0.800±0.006 L of distilled water. Approximately 2.0±0.1 g of $ZrO_2$ was poured into the solution and mixed using a glass stir rod. The top flange of the vessel was placed and sealed using 8 bolts. The pH and ORP probes were calibrated at room temperature and inserted into their respective ports. The initial pH and ORP measurements were recorded and the heating jacket was set to 100 °C. The mixture was allowed to equiliberate for one hour, after which pH and ORP measurements were recorded every 30 mins over a total length of eight days. The mixture was sampled every two days by reducing the temperature to 80 °C and allowing it to equiliberate for an hour. The ORP probe was removed and a 25 mL sample was taken through the ORP port. The ORP probe was returned to its port and sealed, and the temperature was returned to 100 °C. This process was repeated every two days, for a total of four samples per experimental run. Each sample was analyzed using ICP-OES directly after and the aqueous concentration of zirconium was obtained.

The procedure for the experimental runs of the Zircaloy-4 samples was performed in a very similar manner as for zirconium. A 1–2 g Zircaloy-4 cut ring was used and samples were taken every day, including the initial day. A second sample was taken on the 8th day of the experiment at room temperature, resulting in a total of ten samples per experimental run. All samples were sealed and stored in a muffle furnace at 95 °C until the final day of the reaction. All aqueous Zircaloy-4 samples were analyzed by the Water Quality Centre (WQC), at the University of Trent, using inductively coupled plasma mass spectrometry (ICP-MS) to obtain the aqueous concentration of zirconium, tin, and chromium.

### 3.3.4 ICP-OES Standards & Calibration

Six zirconium standard solutions were prepared using distilled water and a zirconium ICP standard from AccuStandard. Standard solutions were made using a serial dilution method with concentrations of 20 mg/L, 15 mg/L, 10 mg/L, 5 mg/L, 1 mg/L, and 0.1 mg/L. A blank was also made for each analysis with a hydrochloric acid or sodium hydroxide concentration matching that of the initial solution being analyzed. The concentration of each standard solution was measured by the ICP-OES and a calibration curve was generated. Each calibration was performed with a minimum confidence of $R^2 \geq 0.995$.

### 3.3.5 FactSage

The EpH module of the FactSage [31] software was used to calculated the Pourbaix diagrams of zirconium and Zircaloy-4 in this work. The EpH module functions by using predetermined thermodynamic data given in database files to calculate the Gibbs energy for a given temperature, pressure, and aqueous metal concentration. More specifically, the EpH module uses the standard enthalpy, standard entropy, and the heat capacity for each chosen species and

calculates the Gibbs energy for each over a range of electrochemical potentials and pH.

The EpH module does not allow for data which is given for a fixed temperature. A heat capacity must be given for each individual species as a result, alongside the enthalpy and entropy of formation at standard conditions. The standard entropy values listed in Table 2.2 and the experimentally determined Gibbs energy of formation values were used to calculate the standard enthalpy values for each zirconium species listed in Section 2.1. These thermodynamic data were inputted into the EpH module for the aqueous species. All other thermodynamic data used for the zirconium, chromium, and tin species were given in Section 2.1. Finally, the EpH module is only able to perform calculations for a maximum of a three-metal system. The Pourbaix diagrams of Zircaloy-4 were calculated using zirconium, tin, and chromium as a result of this limitation.

# Chapter 4

# Results

## 4.1 Preliminary Tests

The measured aqueous concentrations of zirconium for $ZrO_2$ samples are given in Table 4.1. Measurements were performed on three sets of samples, each taken at different temperatures (40 °C, 60 °C, and 80 °C). The concentration of each sample was measured three times, with the average value and standard deviation given in Table 4.1. All metal concentrations given here were measured using ICP-OES.

TABLE 4.1: Zirconium concentrations (ppb) measured over a 9-day period using ICP-OES at 80 °C, with additional measurements taken at 60 °C and 40 °C, at approximately 1.5 pH. Errors are equal to the standard deviation of the measurement.

| Sample Day | 80 °C | 60 °C | 40 °C |
|---|---|---|---|
| 2 | 409.6±30.1 | 280.7±28.5 | 232.5±1.4 |
| 4 | 261.4±5.3 | 243.1±2.3 | 230.3±2.4 |
| 6 | 456.5±16.3 | - | - |
| 8 | 719.7±67.3 | - | - |
| 9 | 742.2±58.9 | 507.8±9.8 | 476.0±5.0 |

The preliminary test measurements were not taken directly at 100 °C. However, these tests indicated that an equilibrium occurred after 8 days. This is illustrated in Figure 4.1, in the form of concentration versus time, for zirconium.

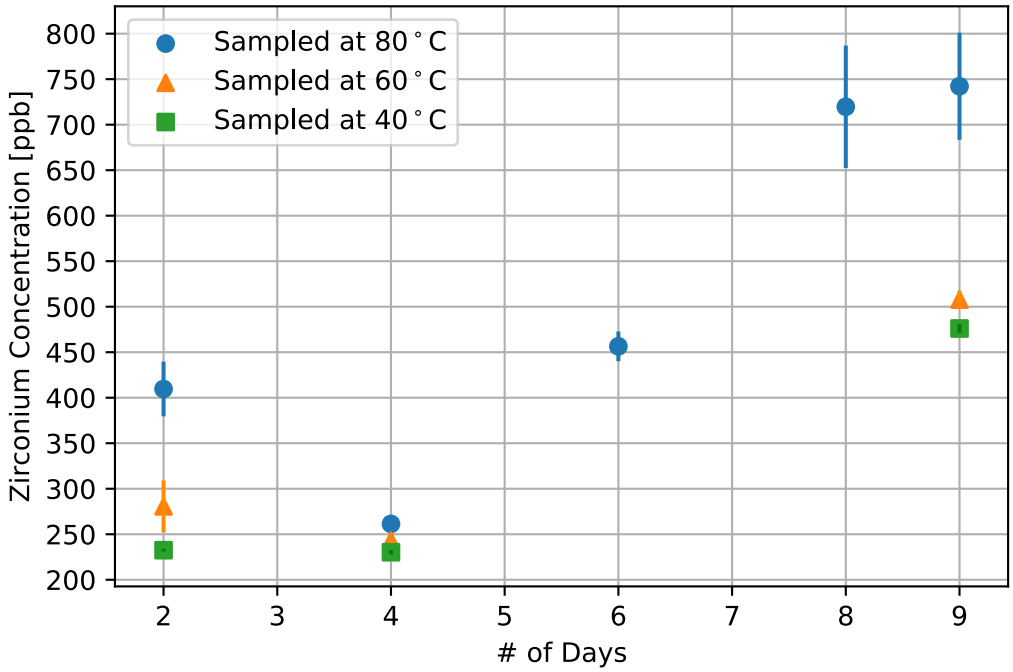


FIGURE 4.1: Aqueous zirconium concentration over a 9 day period in a 0.100±0.006 M perchloric acid solution. Samples taken at 40 °C, 60 °C, and 80 °C and analyzed using ICP-OES.

ICP-OES measurements were performed in a similar manner for the Zircaloy-4 samples, but only at 80 °C. The concentrations of both zirconium and tin were measured. The purpose of this was two-fold: to confirm that a similar aqueous zirconium equilibrium was seen in Zircaloy-4, and to confirm whether the limit of detection for ICP-OES was adequate for tin. The zirconium concentrations indicated a similar equilibrium to the $ZrO_2$ tests, with an equilibrium seen by the 9th day, at 80 °C. The limit of detection for tin using ICP-OES was found to be inadequate, with a negative tin concentration being measured. The zirconium and tin concentrations are given for Zircaloy-4 in Table 4.2 as average values, with the error being the standard deviation. The variation of the concentrations over time is shown in Figure 4.2.

TABLE 4.2: Zirconium and tin concentrations measured over a 9-day period using ICP-OES at 80 °C. Ring sections of Zircaloy-4 were tested at approximately 1.5 pH solution. Errors are equal to the standard deviation of the measurement.

| Sample Day | Zirconium [pbb] | Tin [ppb] |
|---|---|---|
| 2 | 372.6±76.6 | 87.1±498.9 |
| 5 | 322.0±61.2 | -0.1±177.6 |
| 7 | 341.6±51.7 | -172.9±213.8 |
| 9 | 404.5±24.9 | 315.0±420.0 |

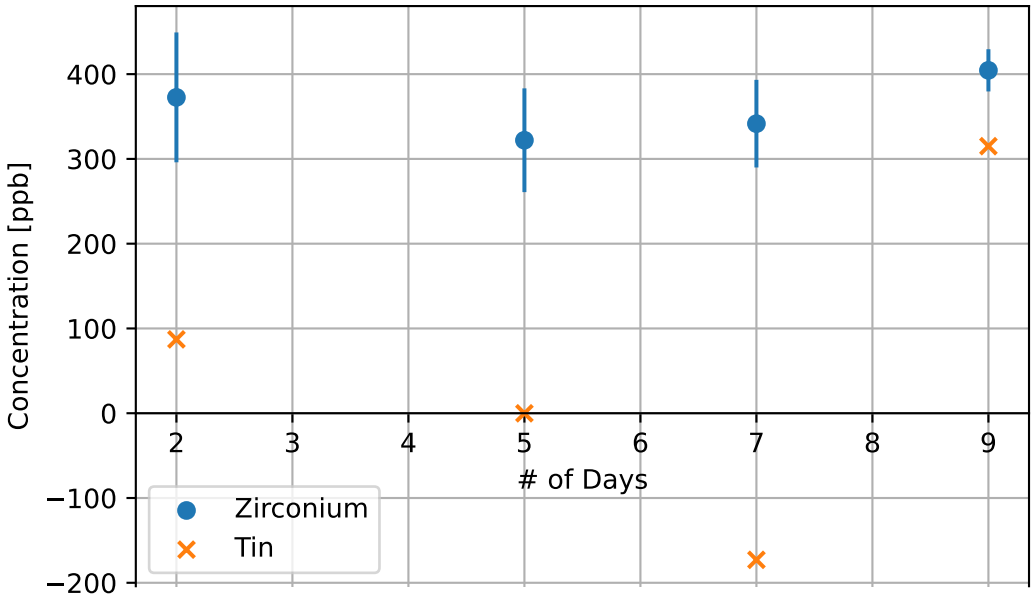


FIGURE 4.2: Aqueous zirconium and tin concentrations over a 9 day period in a 0.100±0.006 M perchloric acid solution. Samples taken at 80 °C analyzed using ICP-OES.

## 4.2 Zirconium

### 4.2.1 ICP-OES

The experimental measurements for the zirconium experiments are presented in Table 4.3, and the measured zirconium concentrations for each of the four pH ranges are presented in Table 4.4. The pH and ORP measurements are presented as averages for the specific day of measurement. Additionally, all pH and ORP measurements were made at 100 °C, while the pH ranges discussed previously were determined for 25 °C. Therefore, there may be some differences in the

measured pH and the stated intended range. Lastly, all ORP measurements were converted from Ag/AgCl to Standard Hydrogen Electrode.

TABLE 4.3: Experimental data from zirconium at 373.15 K.

| Experimental run | Reaction time (days) | Ionic strength (M) | $pH_{373.15\,K}$ | Oxidation-Reduction Potential ($E_H$, V) |
|---|---|---|---|---|
| pH -1–0 | 2 | 3.122±0.010 | -0.82±0.06 | 1.0181±0.0026 |
| | 4 | | -0.50±0.06 | 1.0260±0.0013 |
| | 6 | | -0.73±0.25 | 1.0263±0.0012 |
| | 8 | | -0.26±0.06 | 0.9985±0.0215 |
| pH 0–1 | 2 | 0.600±0.004 | 0.81±0.20 | 1.0838±0.0276 |
| | 4 | | 1.40±0.07 | 1.1020±0.0229 |
| | 6 | | 1.32±0.04 | 1.0879±0.0144 |
| | 8 | | 1.50±0.12 | 1.1357±0.0080 |
| pH 7 | 2 | 0.066±0.004 | 6.64±0.01 | 0.4854±0.0003 |
| | 4 | | 6.59±0.09 | 0.4866±0.0017 |
| | 6 | | 7.35±0.02 | 0.4665±0.0115 |
| | 8 | | 7.19±0.07 | 0.4242±0.0165 |
| pH 13–14 | 2 | 0.301±0.004 | 9.83±1.14 | 0.3696±0.0048 |
| | 4 | | 9.47±1.24 | 0.4324±0.0594 |
| | 6 | | 10.66±0.02 | 0.3702±0.0009 |
| | 8 | | 10.75±0.02 | 0.3630±0.0011 |

TABLE 4.4: ICP-OES measurements from zirconium at 373.15 K.

| Experimental run | Reaction time (days) | Ionic strength (M) | Zr concentration (ppb) |
|---|---|---|---|
| pH -1–0 | 2 | 3.122±0.010 | 2269.1±35.4 |
| | 4 | | 3021.6±80.9 |
| | 6 | | 2458.6±59.4 |
| | 8 | | 3177.4±73.2 |
| pH 0–1 | 2 | 0.600±0.004 | 1475.8±348.4 |
| | 4 | | 526.5±18.2 |
| | 6 | | 462.6±12.4 |
| | 8 | | 482.9±11.7 |
| pH 7 | 2 | 0.066±0.004 | 500.3±18.5 |
| | 4 | | 754.0±50.9 |
| | 6 | | 468.6±8.1 |
| | 8 | | 475.4±42.1 |
| pH 13–14 | 2 | 0.301±0.004 | 410.7±30.0 |
| | 4 | | 520.5±34.6 |
| | 6 | | 628.6±11.3 |
| | 8 | | 202.8±14.1 |

The measured zirconium concentrations are presented in Figure 4.3, for each reaction day, with the error being the standard deviation of the three averaged concentration measurements.

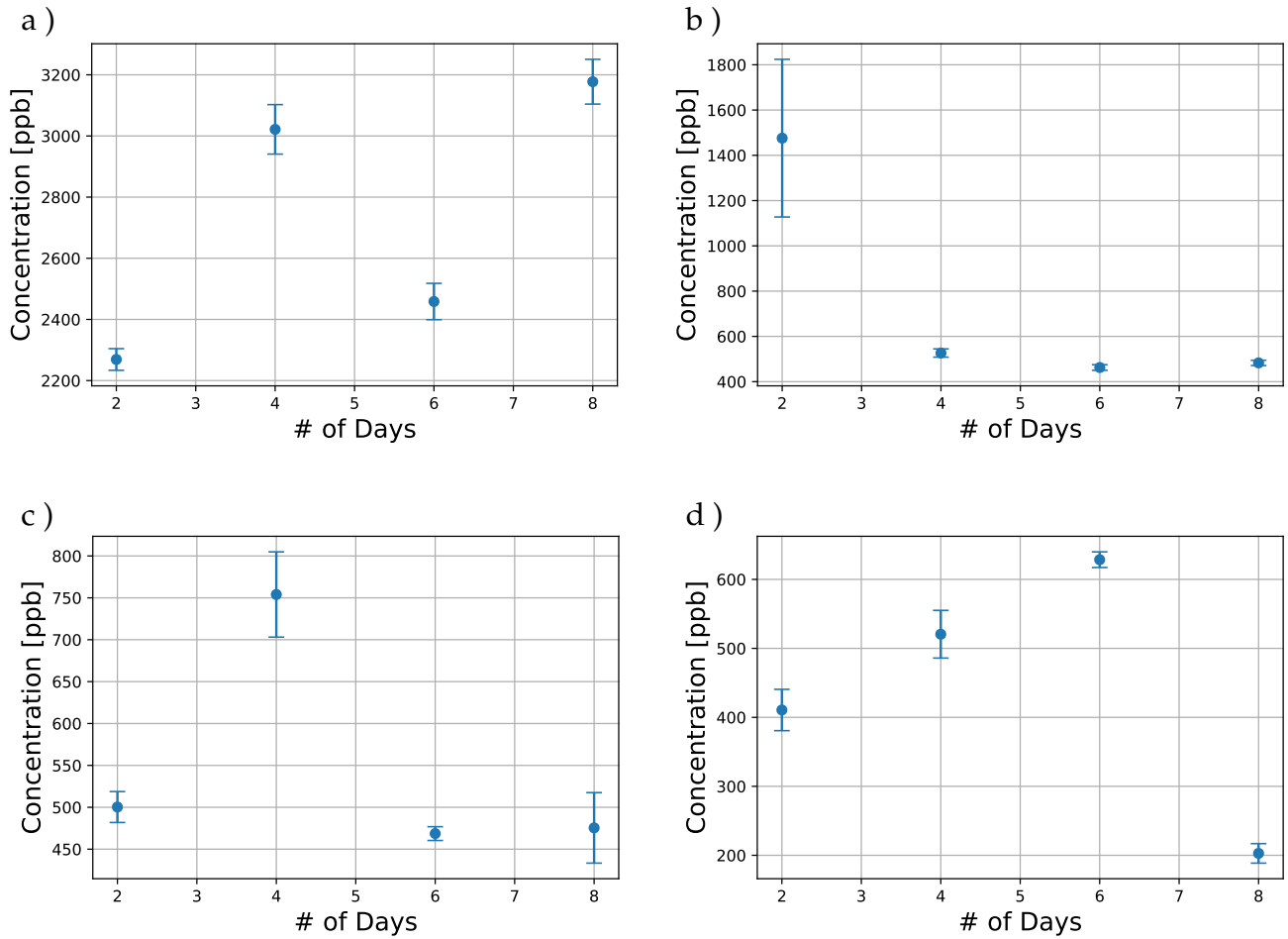


FIGURE 4.3: Zirconium concentrations in solution at various pH ranges, measured over multiple days using ICP-OES. The pH ranges are as follows, a) pH -1–0, b) pH 0–1, c) pH 7, d) pH 13–14.

### 4.2.2 Equilibrium Constants & Gibbs Energy

The equilibrium constants of the isolated species outlined in Figure 2.1 can be calculated given the data from Table 4.3 and through the use of the Davies Equation, Equation 2.9, and the SIT theory, Equation 2.10.

The hydrolysis reaction equations given in section 2.2.1 can first be simplified for each of the species. For example, to identify the equilibrium constant of $Zr(OH)_6^{2-}$ one can combine Equations 2.12 and 2.16, resulting in Equation 4.1. This also leads to the equilibrium constant (Equation 4.2).

$$ZrO_{2(s)} + 4H_2O_{(L)} \rightleftharpoons Zr(OH)_6^{2-} + 2H^+ \tag{4.1}$$

$$K_{Zr(OH)_6^{2-}} = [Zr(OH)_6^{2-}][H^+]^2 \tag{4.2}$$

This equilibrium constant is a non-zero ionic strength constant. So, a correction using Equation 2.6 is necessary to be able to compare it with other sources and to determine the appropriate Gibbs energy. This results in Equation 4.3, where the activity of hydrogen can be taken to be equal to the concentration in an ideal solution. This can be related to the measured zirconium concentration using Figure 2.1, since $Zr(OH)_6^{2-}$ is predicted to make up approximately 90% of the aqueous zirconium concentration in the given pH range, pH 13–14.

$$K^{\circ}_{Zr(OH)_6^{2-}} = [Zr(OH)_6^{2-}]\gamma_{Zr(OH)_6^{2-}}\alpha^2_{H^+} \tag{4.3}$$

$$K^{\circ}_{Zr(OH)_6^{2-}} = 0.9[Zr]\gamma_{Zr(OH)_6^{2-}}(10^{-pH})^2 \tag{4.4}$$

A similar treatment can be performed for $Zr(OH)_2^{2+}$ to obtain the following reaction and equilibrium constant equations.

$$ZrO_{2(s)} + 2H^+ \rightleftharpoons Zr(OH)_2^{2+} \tag{4.5}$$

$$K^{\circ}_{Zr(OH)_2^{2+}} = \frac{[Zr(OH)_2^{2+}]\gamma_{Zr(OH)_2^{2+}}}{\alpha^2_{H^+}} \tag{4.6}$$

Similarly, for $Zr(OH)^{3+}$:

$$2ZrO_{2(s)} + 5H^+ \rightleftharpoons Zr(OH)_2^{2+} + Zr(OH)^{3+} + H_2O \tag{4.7}$$

$$K^{\circ}_{Zr(OH)^{3+}} = \frac{[Zr(OH)_2^{2+}]\gamma_{Zr(OH)_2^{2+}}[Zr(OH)^{3+}]\gamma_{Zr(OH)^{3+}}}{\alpha^5_{H^+}} \tag{4.8}$$

And finally, for $Zr(OH)_{4\,(aq)}$:

$$ZrO_{2(s)} + 2H_2O_{(L)} \rightleftharpoons Zr(OH)_{4(aq)} \tag{4.9}$$

$$K^{\circ}_{Zr(OH)_{4(aq)}} = [Zr(OH)_{4(aq)}]\gamma_{Zr(OH)_{4(aq)}} \tag{4.10}$$

One can now use the Davies Equation (Equation 2.9) to estimate the activity coefficient of $Zr(OH)_6^{2-}$, given that $A_{373.15\,K}$ is -0.6056 and $b$ is 0.3 [67]. The Davies equation can be used to estimate the activity coefficient for $Zr(OH)_2^{2+}$ as well. This cannot be done for $Zr(OH)^{3+}$, as the experimental solution exceeds the ionic strength limitations of the Davies equation. Instead, the SIT theory is used for this species. Additionally, the activity coefficient for $Zr(OH)_{4\,(aq)}$ is assumed to be unity due to its neutral nature.

For $Zr(OH)^{3+}$, the activity coefficient can be calculated using Equation 2.10. The activity coefficient of $Zr(OH)_2^{2+}$ must also be recalculated as a result of the high ionic strength. The interaction coefficients used for $Zr(OH)^{3+}$ and $Zr(OH)_2^{2+}$ account for the interactions of $Zr(OH)^{3+}$ with $Cl^-$, and $Zr(OH)_2^{2+}$ with $Cl^-$. A value of 0.22 kg/mol was used for $Zr(OH)^{3+}$, as reported by *Kraš and Milošev* [71]. A direct value for $Zr(OH)_2^{2+}$ and $Cl^-$ could not be obtained, so the interaction parameter of $Zr(OH)_2^{2+}$ with $ClO_4^-$ was used instead, with a value of 0.62 kg/mol [23]. The resulting activity coefficients are presented in Table 4.5.

TABLE 4.5: Activity coefficients of zirconium hydrolysis species at 373.15 K. For $Zr(OH)_2^{2+}$, a) was calculated using the Davies equation and b) was calculated using SIT theory.

| Species | $Zr(OH)_6^{2-}$ | $Zr(OH)_{4\ (aq)}$ | $Zr(OH)^{3+}$ | $Zr(OH)_2^{2+}{}_{a)}$ | $Zr(OH)_2^{2+}{}_{b)}$ |
|---|---|---|---|---|---|
| $\gamma_{100°C}$ | 0.229 | 1.000 | 0.006 | 0.239 | 0.103 |

These activity coefficients were used in tandem with the measured pH values and zirconium concentrations to calculate the zero ionic strength equilibrium constants, using the previously given equations, and are tabulated in Table 4.6. All concentration values for the hydrolysis species are multiplied by the expected percentage of the aqueous zirconium in the form of the given species, as seen in Figure 2.1.

The Gibbs energy of reaction can then be calculated using the values in Table 4.6 and Equation 1.6, with a temperature of 373.15 K and universal gas constant of 8.3145 $J \cdot mol^{-1} \cdot K^{-1}$. The resulting values for the Gibbs energy of reaction are provided in Table 4.6.

TABLE 4.6: Equilibrium constants, $log(K^\circ)$, for zirconium hydrolysis species at 373.15 K over 8 day period. Precision given for averages is equal to one standard deviation. The resulting Gibbs energy of reaction is given for each species.

| Time (day) | $Zr(OH)_6^{2-}$ | $Zr(OH)_{4\ (aq)}$ | $Zr(OH)^{3+}$ | $Zr(OH)_2^{2+}$ |
|---|---|---|---|---|
| 2 | -25.69 | -5.26 | -17.53 | -3.81 |
| 4 | -24.86 | -5.08 | -15.69 | -3.09 |
| 6 | -27.16 | -5.29 | -17.04 | -3.30 |
| 8 | -27.84 | -5.28 | -14.48 | -2.93 |
| Average $\log(K^\circ)$ | -26.4±1.2 | -5.2±0.1 | -16.2±1.2 | -3.3±0.3 |
| $\delta G^\circ_{r,373.15\,K}$ (kJ/mol) | 188.5±8.4 | 37.4±0.6 | 115.6±8.5 | 23.5±2.4 |

The previous $log(K^\circ)$ and Gibbs energy of reaction values are given for the reaction equations given above where the initial source of zirconium is $ZrO_2$. Most literature sources will provide these values using reactions in the form of Equations 2.12 to 2.16. Table 4.7 provides these values in the traditional form, given that the solubility constant for $Zr^{4+}$ is $-7 \pm 1.6$ [23] and understanding

that the overall equilibrium constant in a multi-step reaction is the product of the equilibrium constant of each individual step [23], *i.e.*, $K_{total} = K_1 \cdot K_2 \cdot K_3$.

TABLE 4.7: Equilibrium constants, $log(K^{\circ})$ of the zirconium hydrolysis species, with reaction equations of the form $Zr^{4+} + nH_2O \rightleftharpoons Zr(OH)_n^{4-n} + nH^+$

| Species | $Zr(OH)_6^{2-}$ | $Zr(OH)_{4\,(aq)}$ | $Zr(OH)^{3+}$ | $Zr(OH)_2^{2+}$ |
|---|---|---|---|---|
| $\log(\beta^{\circ})$ | -19.4±2.0 | 1.8±1.6 | -5.9±3.3 | 3.7± 1.6 |

These Gibbs energy of reaction can be used to calculate the standard Gibbs energy (*i.e.*, Gibbs energy of formation) for each hydrolysis species. This allows direct comparison of values with other experimental works which used different reaction media. The standard Gibbs energy can be calculated using the generalized formula,

$$\Delta G^{\circ}_{r,T} = \sum G^{\circ}_{products,T} - \sum G^{\circ}_{reactants,T} \tag{4.11}$$

The standard Gibbs energy at 373.15 K will be required for $H^+$, $ZrO_2$, and $H_2O$ to calculate the standard Gibbs energy for each of the hydrolysis species. However, values of this type are traditionally provided at standard conditions and extrapolation will be required. The required thermodynamic data were provided in Tables 2.4 and 2.5. The standard Gibbs energy values at 373.15 K for $ZrO_2$, $H_2O$, and $H^+$ were calculated, using Equation 1.34, to be: -1118.52±1.3 kJ/mol; -311.85±0.1 kJ/mol; and 0 kJ/mol, respectively [23].

A sample calculation can be performed for $Zr(OH)_6^{2-}$, using Equation 4.11 and the Gibbs energy values for the auxiliary species.

$$\Delta G^{\circ}_{Zr(OH)_6^{2-},373.15\,\mathrm{K}} = G^{\circ}_{Zr(OH)_6^{2-}} + 2G^{\circ}_{H^+} - G^{\circ}_{ZrO_2} - 4G^{\circ}_{H_2O}$$

$$G^{\circ}_{Zr(OH)_6^{2-}} = \Delta G^{\circ}_{Zr(OH)_6^{2-},373.15\,\mathrm{K}} - 2G^{\circ}_{H^+} + G^{\circ}_{ZrO_2} + 4G^{\circ}_{H_2O}$$

$$G^{\circ}_{Zr(OH)_6^{2-},373.15\,\mathrm{K}} = -2177.4 \pm 8.5 kJ/mol$$

Therefore, the standard Gibbs energy for $Zr(OH)_6^{2-}$ is -2177.4±8.5 kJ/mol. This calculation was repeated for each of the four hydrolysis species, giving the following values for $\Delta G_f^\circ$ at 373.15 K for $Zr(OH)_6^{2-}$; $Zr(OH)_{4\,(aq)}$; $Zr(OH)^{3+}$; and $Zr(OH)_2^{2+}$ to be: -2177.4±8.5 kJ/mol, -1704.9±1.5 kJ/mol, -1808.8±8.9 kJ/mol, and -1095.1±2.7 kJ/mol, respectively.

## 4.3 Zircaloy-4

### 4.3.1 ICP-MS

As a result of equipment difficulties, only the zirconium, chromium, and tin concentrations of the Zircaloy-4 experiments could be accurately recorded. No ORP or pH measurements will be provided, as a result of these difficulties, to prevent misrepresentation. The measured aqueous metal concentrations of each element are provided in Table 4.8, with both an elevated temperature and room temperature sample analyzed on the final day. These samples are indicated as (hot) and (cold) for the elevated temperature samples and room temperature samples, respectively. All ICP-MS measurements are presented as an average of a set of three measurements, with the precision being the standard deviation of each. A visualization of the concentrations over time is provided in Figure 4.4.

TABLE 4.8: Aqueous zirconium, chromium, and tin concentrations measured using ICP-MS by the Trent WQC. Hot samples were taken just below 373.15 K, cold samples were taken at room temperature.

| Experimental run | Reaction time (days) | Sn concentration (ppb) | Cr concentration (ppb) | Zr concentration (ppb) |
|---|---|---|---|---|
| pH -1–0 | 0 | 6.36 | 38.61 | 39.09 |
| | 1 | 49.48 | 420.14 | 20.34 |
| | 2 | 49.85 | 531.77 | 22.74 |
| | 3 | 54.33 | 742.90 | 30.20 |
| | 4 | 38.86 | 843.96 | 50.36 |
| | 5 | 26.27 | 992.17 | 57.75 |
| | 6 | 28.75 | 1192.90 | 77.86 |
| | 7 | 43.65 | 1417.77 | 99.85 |
| | 8 (hot) | 24.57 | 2032.29 | 124.34 |
| | 8 (cold) | 28.70 | 2031.29 | 124.85 |
| pH 0–1 | 0 | 43.62 | 17.47 | 62.94 |
| | 1 | 124.28 | 27.10 | 28.80 |
| | 2 | 25.55 | 28.87 | 29.80 |
| | 3 | 23.59 | 34.61 | 36.14 |
| | 4 | 11.31 | 42.12 | 38.75 |
| | 5 | 11.36 | 40.95 | 37.24 |
| | 6 | 10.99 | 42.59 | 38.03 |
| | 7 | 8.04 | 50.74 | 45.47 |
| | 8 (hot) | 6.81 | 68.69 | 40.13 |
| | 8 (cold) | 7.47 | 48.95 | 41.28 |
| pH 7 | 0 | 1.89 | 1.10 | 23.93 |
| | 1 | 1.40 | 0.40 | 15.66 |
| | 2 | 2.62 | 0.49 | 12.48 |
| | 3 | 3.51 | 1.43 | 14.35 |
| | 4 | 2.11 | 0.70 | 11.72 |
| | 5 | 2.32 | 0.49 | 7.39 |
| | 6 | 2.30 | 1.04 | 11.01 |
| | 7 | 2.04 | 0.91 | 12.02 |
| | 8 (hot) | 2.06 | 1.24 | 11.89 |
| | 8 (cold) | 2.40 | 1.02 | 10.44 |
| pH 13–14 | 0 | 2.77 | 8.20 | 0.00 |
| | 1 | 9.46 | 122.07 | 3.23 |
| | 2 | 7.46 | 168.43 | 0.86 |
| | 3 | 6.62 | 185.83 | 0.76 |
| | 4 | 4.10 | 195.10 | 2.40 |
| | 5 | 5.25 | 229.46 | 1.20 |
| | 6 | 8.31 | 232.88 | 0.95 |
| | 7 | 6.69 | 256.79 | 1.30 |
| | 8 (hot) | 5.73 | 260.59 | 0.73 |
| | 8 (cold) | 5.36 | 245.50 | 0.00 |

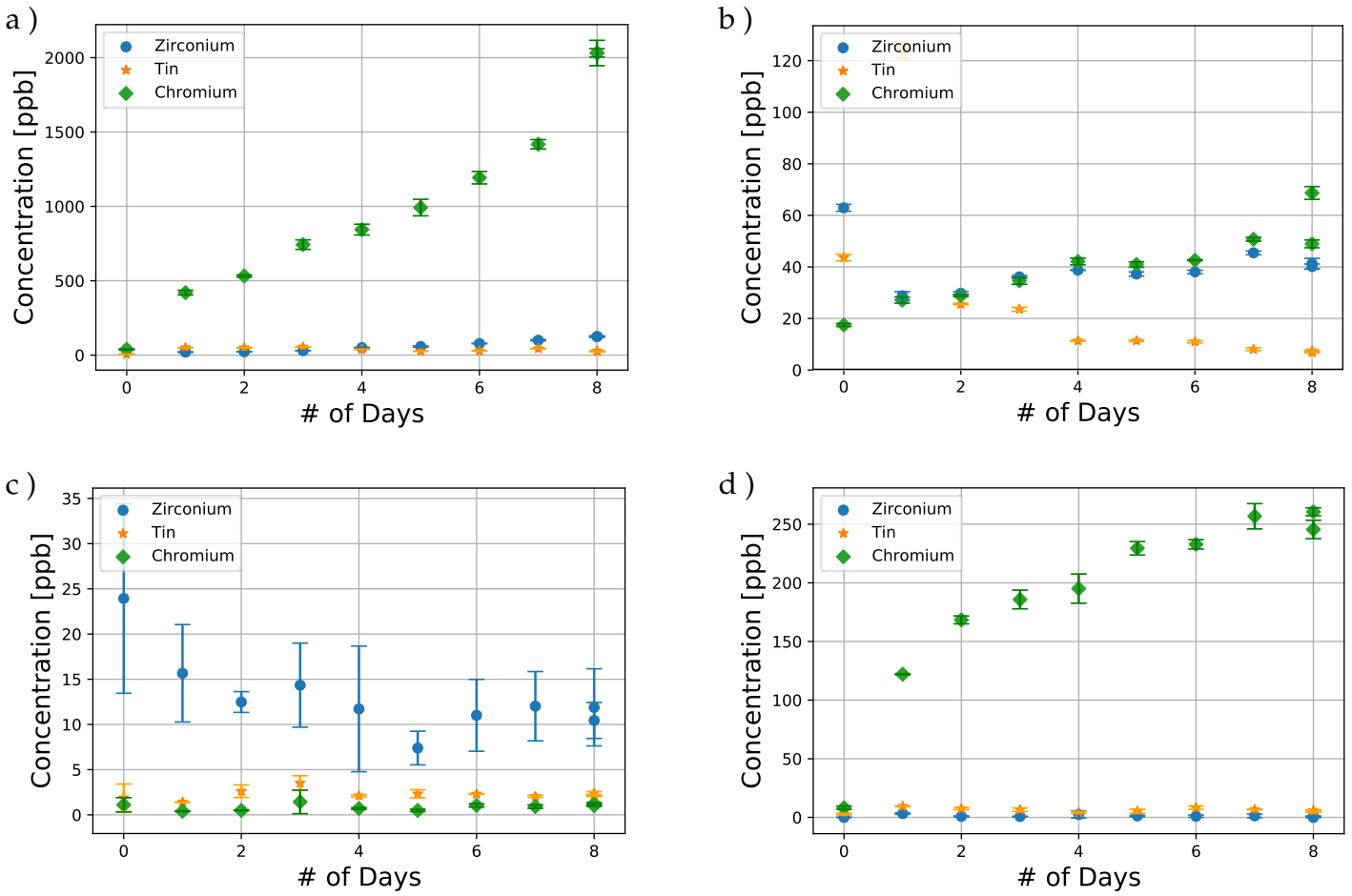


FIGURE 4.4: Measured concentrations of Zr, Cr, and Sn in various pH ranges over an eight day period, using ICP-MS. a) pH -1–0, b) pH 0–1, c) pH 7, d) pH 13–14. Precision given by standard deviation over three replicate measurements.

## 4.4 Pourbaix Diagrams

### 4.4.1 Zirconium

Pourbaix diagrams were calculated using the EpH module of FactSage [31] and the thermodynamic data presented in Section 2.1.1. The values presented in Tables 2.2 and 2.3 were used in FactSage [31]. Figure 4.5 shows the Pourbaix diagram for zirconium at 298.15 K.

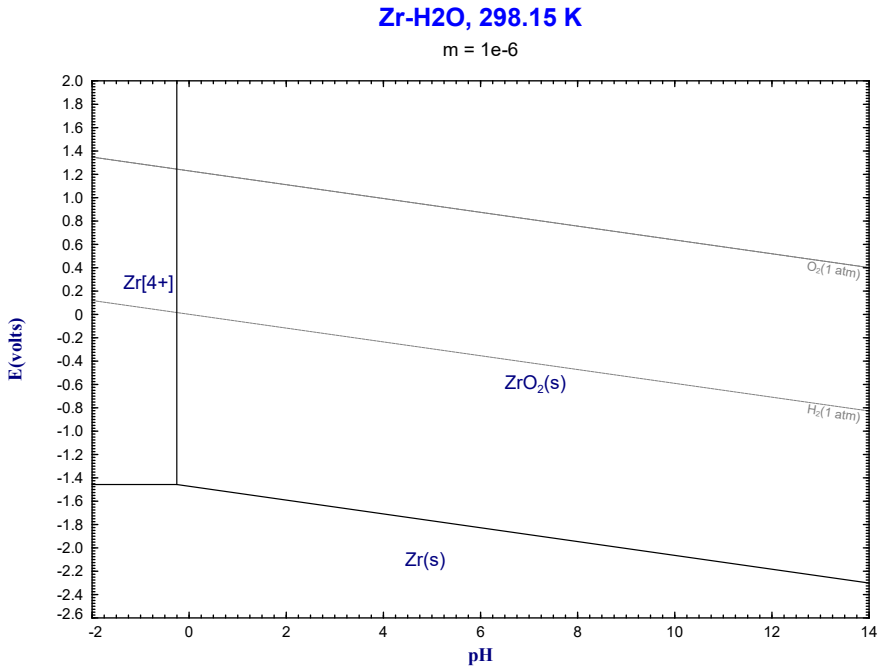


FIGURE 4.5: Pourbaix diagram of zirconium at 298.15 K and $10^{-6}$M. Constructed using literature and estimated data, with FactSage [31].

The Pourbaix diagram for zirconium at 373.15 K is given in Figure 4.6, using extrapolation to obtain the required thermodynamic data at this temperature. The heat capacities used for each species were provided in Section 2.1.1. The molarity of the aqueous species is $10^{-6}$ M.

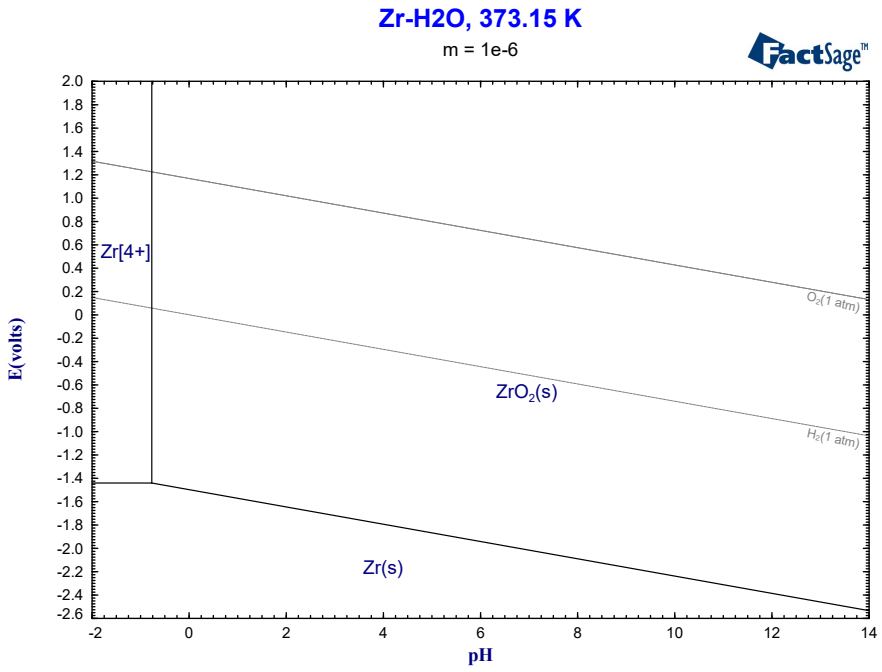


FIGURE 4.6: Pourbaix diagram of zirconium at 373.15 K and $10^{-6}$M. Constructed using literature and estimated data, with FactSage [31].

The Pourbaix diagrams for zirconium were recalculated using the experimentally determined standard Gibbs energy values given at the end of Section 4.2.2. The E-pH module of FactSage [31], which generates the Pourbaix diagrams, requires variable temperature thermodynamic data. To account for this, the experimentally determined standard Gibbs energy values were used with entropy values from Table 2.2 and Equation 1.34 to determine the enthalpy of formation for each hydrolysis species, for the given temperature. The diagrams resulting from this were calculated at 298.15 K and 373.15 K. Figure 4.7 shows the Pourbaix diagram calculated at 298.15 K. It should be noted that ZrH was omitted from this diagram as it was found to directly replace the solid zirconium metal domain.

Figure 4.8 shows the Pourbaix diagram calculated at 373.15 K. Again, ZrH was omitted from this diagram, because it was found to directly replace the solid zirconium metal domain.

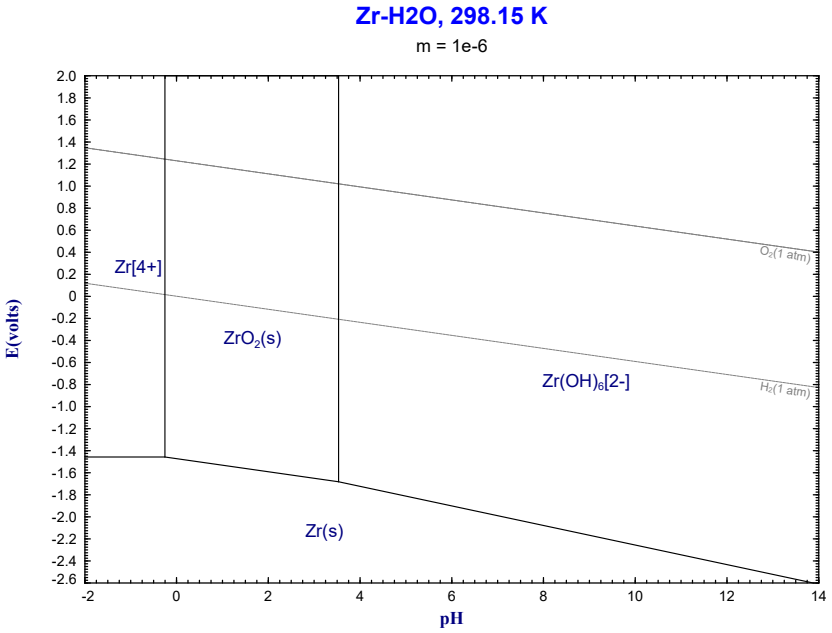


FIGURE 4.7: Pourbaix diagram of zirconium at 298.15 K and $10^{-6}$ M. Constructed using experimentally derived standard Gibbs energy values, with FactSage [31].

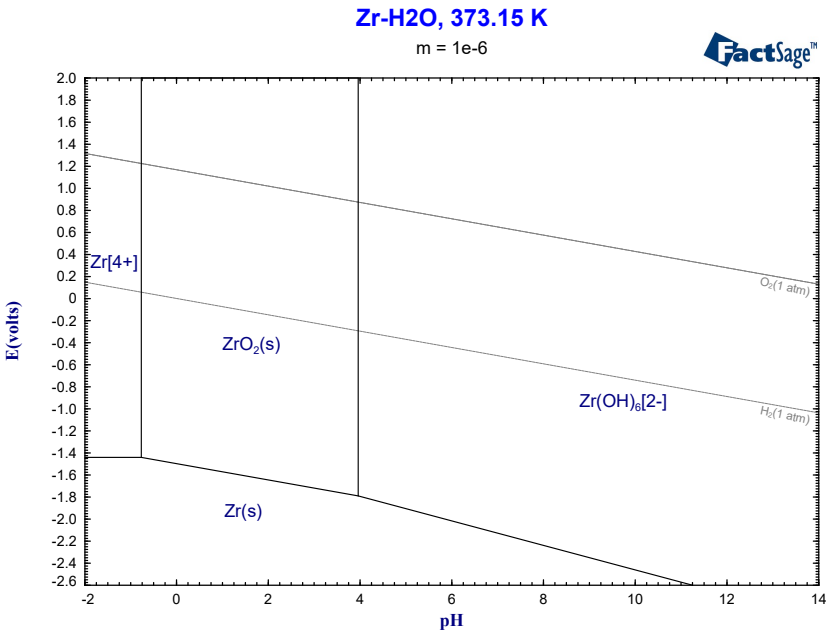


FIGURE 4.8: Pourbaix diagram of zirconium at 373.15 K and $10^{-6}$ M. Constructed using experimentally derived standard Gibbs energy values, with FactSage [31].

### 4.4.2 Zircaloy-4

For Zircaloy-4, more than just zirconium species must be accounted for. Both tin and chromium species should considered, as well as any intermetallic ionic species. These metals do not tend to form aqueous intermetallic hydrolysis species and only mono-metallic species need to be used in the calculation.

The Pourbaix diagram for Zircaloy-4 at 298.15 K is shown in Figure 4.9, using the thermodynamic data presented in Tables 2.7, 2.8, 2.10, and 2.11.

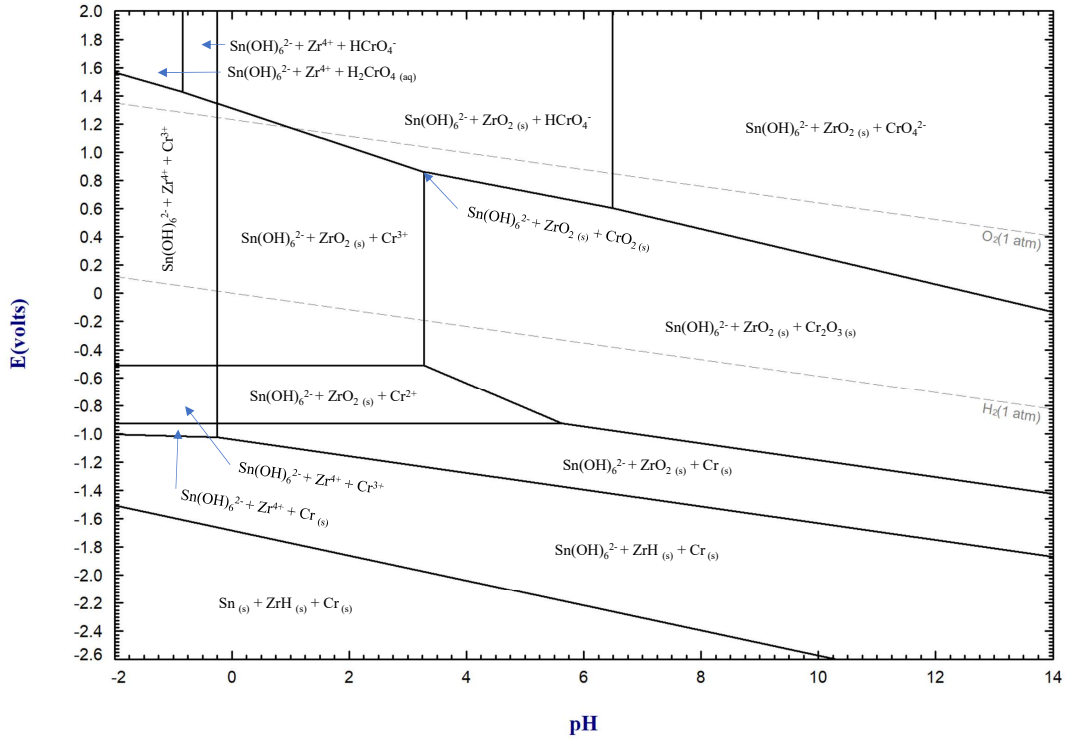


FIGURE 4.9: Pourbaix diagram of Zircaloy-4 (Zr, Sn, Cr) at 298.15 K and $10^{-6}$ M. Constructed using literature and estimated data, with FactSage [31].

The Pourbaix diagram for Zircaloy-4 at 373.15 K is shown in Figure 4.10. Again, the thermodynamic data used are taken from Tables 2.7, 2.8, 2.10, and 2.11. Extrapolation was performed using previously provided heat capacities for the species of each element. Iron was omitted due to technical limitations

of the EpH module in the FactSage [31] software, since the software can only consider equilibria of water (*i.e.*, $H_2$ and $O_2$) with at most three other elements.

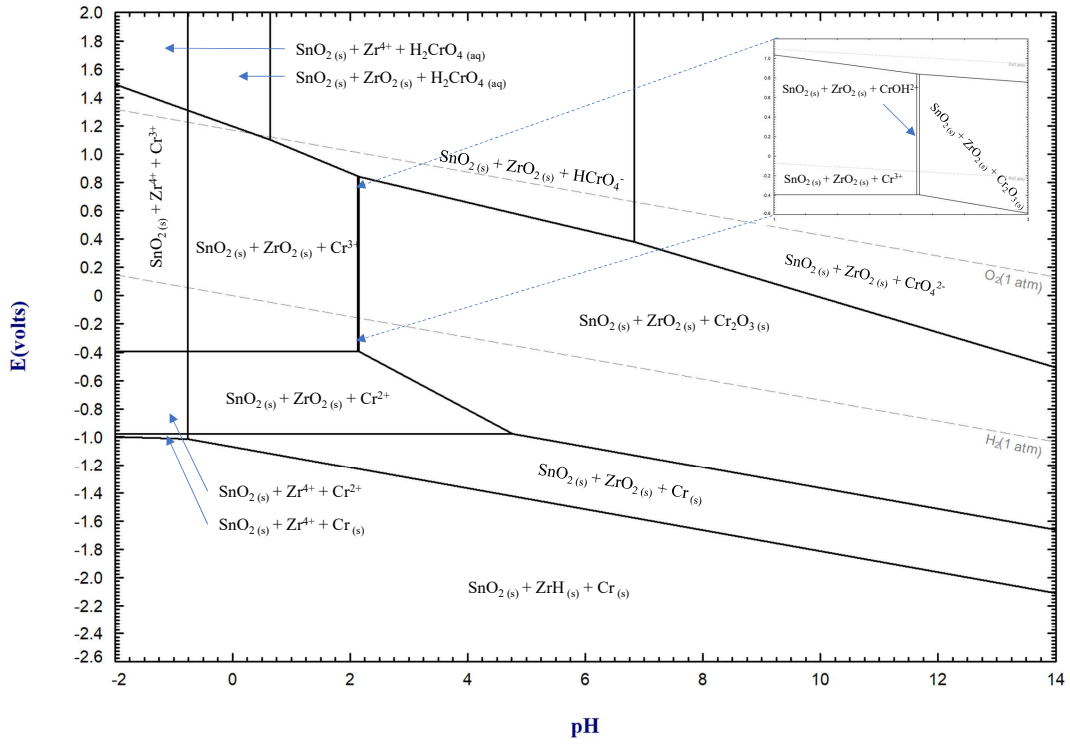


FIGURE 4.10: Pourbaix diagram of Zircaloy-4 (Zr, Sn, Cr) at 373.15 K and $10^{-6}$ M. Constructed using literature and estimated data, with FactSage [31].

# Chapter 5

# Discussion

## 5.1 Concentration Measurements

### 5.1.1 Zirconium

It was found that the measured zirconium concentrations in the preliminary experiments and the pH 0–1 experimental run differed over the 8 day period, both in magnitude and in the variation of the concentration. As shown in Table 4.1, the preliminary experiment was found to have a lower overall maximum concentration of 742.2±58.9 ppb. The zirconium concentration decreased between day 2 and 4, before increasing almost linearly until day 8. On the other hand, the experimental run was found to have a maximum at day 2, with a value of 1475.8±348.4 ppb, before dropping dramatically.

A potential cause of this different trend in measured concentrations would be the use of perchloric acid as the acidifying agent in the preliminary tests versus hydrochloric acid in the experimental runs. Perchloric acid was required to be used instead of hydrochloric acid, as the PAS body of the probes are incompatible with perchloric acid. Perchloric acid was originally used to generate acidic solutions without complexation of the metal and chloride ions, as the $ClO_4^-$ ion is non-complexing. However, the chlorine ions from HCl would increase the formation of zirconium chloride species, thereby increasing the solubility of the zirconium.

Though, this does not inherently explain the rapid decrease in the zirconium concentration after the 2 day mark in the experimental run. Intuitively, the concentration would be consistently increasing as a result of the increased solubility, but it does not. It may be that the increased solubility of zirconium from chlorine complexation allowed for the reordering of the zirconium into a more stable and less soluble crystal form. This mechanism has been observed before at both standard conditions by *Curti and Degueldre* [72] and at 373 K by *Qiu et al.* [73].

In the work by *Qiu et al.*, $ZrO_2$ was dissolved in an aqueous LiOH solution with a pH of 10.48 [73]. The shift in the aqueous zirconium concentration was seen to occur after 200 hours, at 373 K, with a maximum concentration near 77.54 ppb [73]. Given that the maximum concentration seen in this work was two orders of magnitude greater than that of *Qiu et al.* [73], it is understandable to see a rapid decrease in the concentration after the 2 day mark. It is also known that oversaturation tends to result in higher zirconium concentrations in acidic solutions, as the depolymerization of aqueous zirconium species becomes hindered [72, 74].

This trend of higher measured zirconium concentrations in this work compared to other sources was found in all pH ranges. For example, the pH 13–14 range tests, which are closest to that of *Qiu et al.*, were consistently a magnitude greater than the measurements of *Qiu et al.* [73].

Another factor that may contribute to the higher measured zirconium concentrations would be carbon dioxide contamination. Zirconium is known to undergo complexation by carbonate ions, which results in elevated solubility of zirconium [23]. The reaction vessel was kept under an air atmosphere at all times during reaction, leading to the possibility for contamination. Though the volume of carbon dioxide to water would be expected to be low, given that the plenum was only 200 mL, compared to the 1800 mL of solution.

The variation in the measured concentrations may also be a result of the

variation in the pH of the experimental solutions. For the pH -1–0 range, the zirconium concentration was found to increase when the pH increased towards zero and decreased towards pH -1. It may be that the presence of $Zr^{4+}$ results in greater polymerization and decreased solubility compared to $Zr(OH)^{3+}$ and $Zr(OH)_2{}^{2+}$. The inverse of this behaviour was observed for the pH 0–1 range, where the concentration tended to increase as the pH was closer to zero. This, in tandem with the trend from the -1–0 pH range, could insinuate that the $Zr(OH)^{3+}$ species has a higher solubility than $Zr(OH)_2{}^{2+}$ and $Zr(OH)_4$. The variation in the concentrations of the pH 13–14 and pH 7 experiments were not as consistent as the more acidic regions.

### 5.1.2 Zircaloy-4

For Zircaloy-4, the variations in aqueous metal concentrations over time were more consistent than for zirconium. The measured concentrations were presented in Figure 4.4 and are shown again in a semilog scale in Figure 5.1. When compared to zirconium and tin, the chromium concentrations were significantly higher in the pH -1–0 and pH 13–14 ranges. Even though the nominal weight percentage of chromium in Zircaloy-4 is 0.1%wt, the chromium concentrations were one to two magnitudes higher than zirconium. This shows that chromium is lost in disproportionately large amounts in more extreme pH ranges, while both zirconium and tin experience corrosion in lesser amounts. Tin was found in higher concentrations than zirconium in the pH 13–14 range, with the tin concentration appearing to decrease as the zirconium concentration increased. This trend was also seen in both the pH 0–1 and -1–0 ranges. This may be due to competing complexation mechanisms with ions in solution; but no concrete evidence can be given for this. Interestingly, the pH 7 experimental run was found to have very different trends. Zirconium concentrations were found to be much higher than tin and chromium, and it appeared that the

concentration of all three metals fluctuated in a similar pattern from day 2 to day 8. It could be possible that the alloy corroded uniformly in these more mild conditions and resulted in the metals exhibiting similar aqueous behaviours.

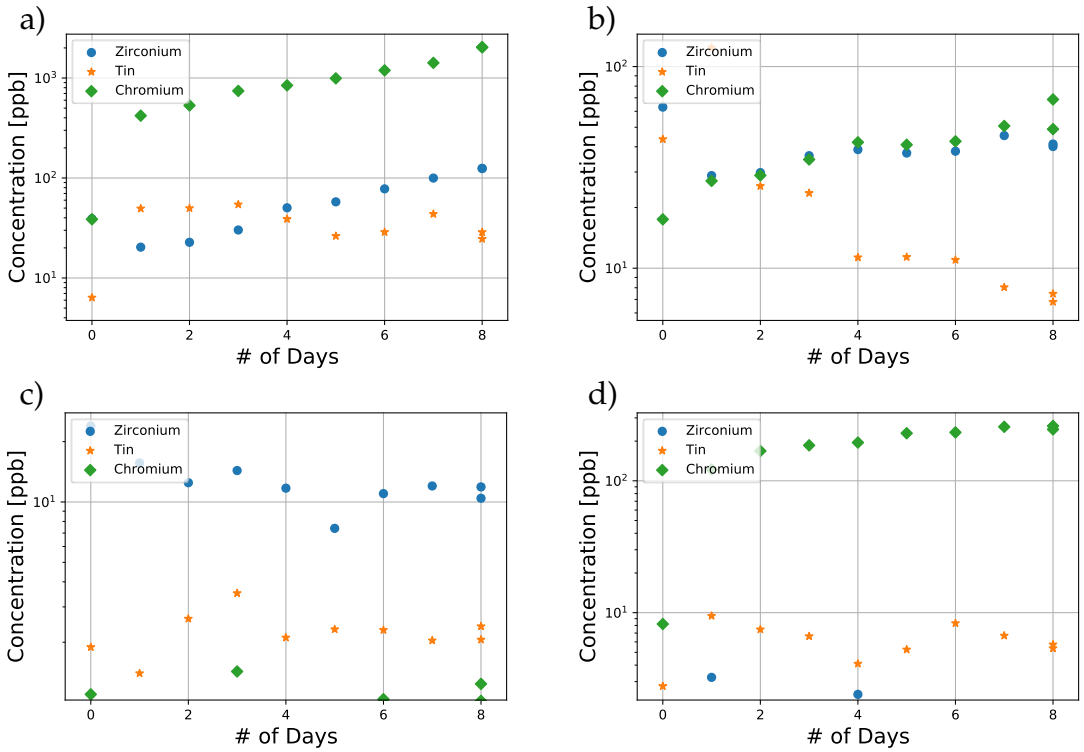


FIGURE 5.1: Measured concentrations of Zr, Cr, and Sn using ICP-MS in a semilog scale. a) pH -1–0, b) pH 0–1, c) pH 7, d) pH 13–14.

## 5.2 Gibbs Energy of Formation and Log($K^{\circ}$)

### 5.2.1 $Zr(OH)_6^{2-}$

The $log(\beta^{\circ}_{Zr(OH)_6^{2-}})$ value determined in the pH 13–14 region, at 373.15 K was found to be higher than other reported values at 298.15 K, -19.4±2.0 versus -29.0±0.7 [23] and −33.29 [71]. There are no available works that allow a direct comparison of values at 373.15 K. A comparison can be made between these

values, but it is not expected they will be the same as equilibrium constants are known to change with temperature.

It has been seen previously that the hydrolysis/equilibrium constants of zirconium hydrolysis species tend to increase with temperature. This is illustrated well in the work by *Ekberg et al.* [34] for various hydrolysis species in (Na,H)$ClO_4$, with hydrolysis constants varying by up to 2.9 over a 20 °C range. It may be that the measured value is simply higher because of the temperature, but this cannot be confirmed without further experimentation.

As mentioned previously, it is also possible that carbon dioxide contamination occurred. The value of $log(\beta^{\circ})$ for $Zr(OH)_6^{2-}$ is quite close to the reported values of -16.0 [36] and -19.66 [71] for $Zr(OH)_5^-$, with $Zr(OH)_5^-$ originally proposed by *Baes and Mesmer* [36] to be dominant at high pH values. This has since been suggested to be incorrect, as it is likely that carbon dioxide contamination occurred the original experiments [36, 75]. It is unlikely that if it occurred that carbon dioxide contamination was the sole influence in the difference of the measured equilibrium constant and that proposed by *Baes and Mesmer*. The values reported here and by *Baes and Mesmer* are close for $Zr(OH)_5^-$, given the 100 °C difference in measurement temperatures.

The Gibbs energy of formation for $Zr(OH)_6^{2-}$ is reported to be -1785.8±10.1 kJ/mol at 298 K [23]. The determined value in this work was -2177.4±8.5 kJ/mol, a noticeably lower value. However, it is important to note how the Gibbs energy can scale with temperature, as shown in Equation 1.34. Given the thermodynamic values for $Zr(OH)_6^{2-}$, stated in Table 2.2, it would be expected that the Gibbs energy of formation would decrease by a notable amount with an increase in the measurement temperature. A general illustration of the Gibbs energy of formation temperature dependence for each zirconium hydrolysis species is provided in Figure 5.2. It is with this understanding that is believed that the determined Gibbs energy of formation is relatively accurate. Though, repeated measurements under a carbon dioxide free atmosphere are

recommended to ensure that this result is reproducible.

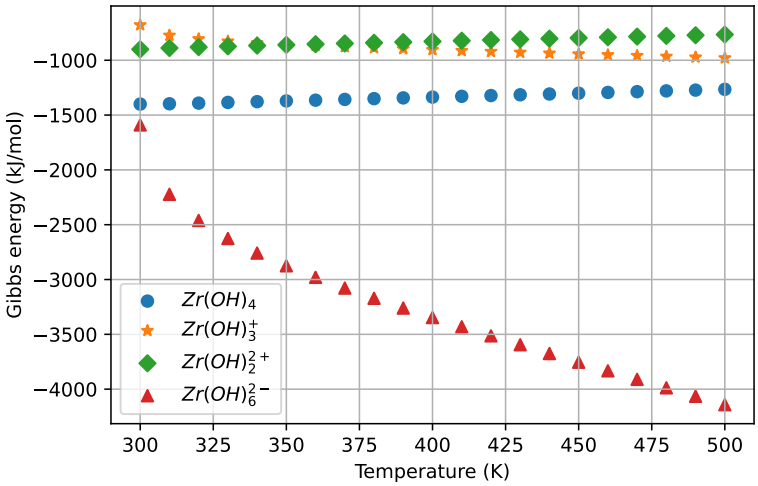


FIGURE 5.2: Predicted change in the Gibbs energy of formation for zirconium hydrolysis species, using the thermodynamic data provided in Table 2.2.

### 5.2.2 $Zr(OH)_{4\,(aq)}$

A more dramatic difference was seen between the measured value of $log(\beta^{\circ})$ for $Zr(OH)_{4\,(aq)}$ and reported literature values. The selected value by the NEA was -2.19±1.70 [23], whereas the value determined in this work was 1.8±1.6. Even so, significant variance in the reported values for the hydrolysis constant of $Zr(OH)_4$ can be seen in literature sources. For example, *Curti and Degueldre* [72] and *Kobayashi et al.* [35] reported values of -9.7 and 54.78, respectively. It is important to note that the value given by *Kobayashi et al.* was reported as an upper limit rather than an exact value. With this variance in literature values in mind, it is clear that the value determined in this work does not agree within error of the NEA values. The determined value of this work does come rather close given the difference in temperature though, as $log(\beta^{\circ})$ is expected to increase with an increase in temperature.

This determined value can also be directly compared to the work of *Qiu et al.* [73] who evaluated the solubility of zirconium dioxide up to 573 K and were

able to develop an equation for the equilibrium constant of $Zr(OH)_{4\,(aq)}$ that is dependent on temperature. The equation (given below) at 373 K for *ln(K)* provides a value of 0.34 when converted to *log(K)*.

$$lnK_h = \frac{12149.6}{T} + 30.26ln(T) - 211.61 \tag{5.1}$$

Our determined equilibrium constant for $Zr(OH)_{4\,(aq)}$ coincides, within precision, with the resulting value from Equation 5.1, and there is high confidence in the determined value.

The Gibbs energy of formation for $Zr(OH)_{4\,(aq)}$, at 298 K, is reported to be -1464.6±13.4 kJ/mol and -1472.6 kJ/mol, by *Brown et al.* [23] and by *Qiu et al.* [73] respectively . This value at 373.15 K was found to be -1704.9±1.5 kJ/mol, a notable decrease from the standard conditions. While this does disagree with the general plot given in Figure 5.2, that is likely a result of an underestimated heat capacity for aqueous $Zr(OH)_4$. An increased stability at elevated temperatures has also been predicted previously, with $Zr(OH)_4$ being suggested to be the dominant species at elevated temperatures, outside of highly acidic or alkaline conditions [37, 73]. Therefore, it is reasonable to see this difference in the Gibbs energy of formation at elevated temperatures compared to standard conditions.

### 5.2.3 $Zr(OH)_2^{2+}$

The $log(\beta^\circ)$ of 3.7±1.6 for $Zr(OH)_2^{2+}$ at 373.15 K was found to be higher than the reported value of 0.98±1.06 for 298 K, but only by 0.06 when accounting for precision. The difference in values can likely be attributed to the difference in measurement temperature, as was partially done for $Zr(OH)_6^{2-}$. Other values of $log(K^\circ)$ for $Zr(OH)_2^{2+}$ at 298 K have been reported previously in the literature. However, these values tend to vary with the method used and whether an oversaturated or undersaturated solution was used. For example, *Bilinski et al.*

[38] obtained a value of -2.77 using an oversaturation solution, while *Kobayashi et al.* [35] used a value of -62.46±0.10 for the solubility constant of $ZrO_2$ rather than $-7 \pm 1.6$. A higher confidence is placed in the value reported by the NEA, due to the extensive literature review that was performed to determine the value.

The Gibbs energy of formation for $Zr(OH)_2^{2+}$ was found to be smaller at 373.15 K, with a value of -1095.1±2.7 kJ/mol compared to -1008.4±11.0 kJ/mol [23] and -1032.42 kJ/mol [37] at 298.15 K. Again, this is contrary to the predicted behaviour given in Figure 5.2. This difference in the predicted behaviour is likely in part due to poorer estimations on the heat capacity using the Criss-Cobble method. It is recommended that the HKF model be used, if possible, for future works as it tends to have a higher accuracy. However, it was not used here as there is a lack of the required experimentally derived constants.

### 5.2.4 $Zr(OH)^{3+}$

The $log(\beta^{\circ})$ value obtained for $Zr(OH)^{3+}$ is believed to be incorrect when compared to other literature sources. The determined value is reported as -5.89±3.31. All other sources report this value to be positive, with the lowest being 0.3 by *Baes and Mesmer* [36]. The NEA [23] reported this ion to have a hydrolysis constant of 0.32±0.22 and multiple sources report to be as high as ≈14 [35, 37]. The hydrolysis constant was also found to increase with temperature by *Ekberg et al.* [34] from 298 K to 308 K, which indicates that the cause of this difference is unlikely to be from measurement at 373 K. Rather, it is likely that $Zr(OH)^{3+}$ was not adequately isolated, which is unsurprising. Based on Figure 2.1, $Zr(OH)^{3+}$ is only expected to make up a maximum of 25% of the aqueous zirconium concentration, within the tested pH range. Additionally, the treatment methods used for the data to calculate the activity coefficient and

hydrolysis constant were likely inadequate, as the activity coefficients of both $Zr(OH)^{3+}$ and $Zr(OH)_2{}^{2+}$ had to be estimated. This would result in greater amounts of imprecision for the final $log(\beta^{\circ})$ value of $Zr(OH)^{3+}$.

Contrary to the Gibbs energy of formation values found for other zirconium hydrolysis species, the determined value for $Zr(OH)^{3+}$ is quite different than other literature values. At 298.15 K, $Zr(OH)^{3+}$ is reported to have values of -767.5±9.3 kJ/mol and -798.75 kJ/mol [23, 37]. The determined value of -1808.8±8.9 kJ/mol at 373.15 K is over 1000 kJ/mol smaller than the literature values at 298.15 K and this difference is unlikely to have been caused by the measurement temperature. Rather, as stated above, it is likely that the $Zr(OH)^{3+}$ was not adequately isolated in the pH -1–0 range. This resulted in the erroneous value given. It is recommended that the Gibbs energy of formation value for $Zr(OH)^{3+}$ be disregarded, as was done when creating the experimental Pourbaix diagrams in the following section.

## 5.3 Pourbaix Diagrams

### 5.3.1 Zirconium

A Pourbaix diagram of zirconium is given in Figure 4.7 at 298.15 K using Gibbs energy of formation values that were experimentally determined at 373.15 K, but extrapolated to 298.15 K. For the diagrams calculated using literature values, Figures 4.5 and 4.6, it can be seen that the predicted species would be $Zr^{4+}$, $ZrO_2$, and Zr. There is very little difference between Figures 4.5 and 4.6, with only the $Zr^{4+}$ boundary region differing. This small region is predicted in these diagrams to be where zirconium actively corrodes at potentials above -1.4 and below approximately pH 0 and pH -0.25, for 298.15 K and 373.15 K, respectively. Outside of this region $ZrO_2$ is predicted to be the dominant species for a majority of the given ranges.

Both the experimentally derived and literature-based diagrams disagree with the original Pourbaix diagram developed for zirconium shown in Figure 1.4. One clear difference is the absence of ionic species outside of $Zr^{4+}$, with Pourbaix including $ZrO^{2+}$ and $HZrO_3^-$ [18]. The absence of $ZrO^{2+}$ is not inherently concerning; because the existence of this species has since been disproven by multiple sources [76–79]. The absence of $HZrO_3^-$ (analogous to $ZrO_3^{2-}$ and $Zr(OH)_6^{2-}$) is a concern. The presence of this ion is corroborated in other experimentally and computational derived diagrams [71, 80].

For example, the Pourbaix diagrams proposed by *Jin et al.* [80] using both density functional theory (DFT) and experimentally derived thermodynamic data. All of which are provided in Figure 5.3 [80]. It can be seen in these diagrams that through DFT calculations there is predicted to be a greater number of regions with dominant ionic species than those seen in Figures 4.5 and 4.6. However, the lower stability domain boundary for $Zr^{4+}$ does relatively match between these diagrams and those created in this work from literature values. Where the stability regions differ greatly is at higher electrochemical potential, where *Jin et al.* [80] predict $HZrO_2^{2+}$ will be dominant. At >12 pH, $HZrO_3^-$ is predicted to be dominant in the mid-range of electrochemical potentials. Additionally, Figure 5.3 a) and b) predict oxide forms with multiple valencies, which are not accounted for in the Pourbaix diagrams of this work. These regions would likely be incorporated within the stability regions of $ZrO_2$ in this work. Further, unlike the non-experimental Pourbaix diagrams given in Figures 4.5 and 4.6, the $Zr(OH)_6^{2-}$ (analogous to $HZrO_3^-$) can be seen in Figure 4.8, with a stability region much greater than in *Jin et al.* [80]. This is likely a shortcoming of the heat capacity estimation using the Criss-Cobble method which propagated inaccuracies through to other calculations. However, the lower electrochemical potential boundary of the stability region does appear to be similar to those in Figure 5.3.

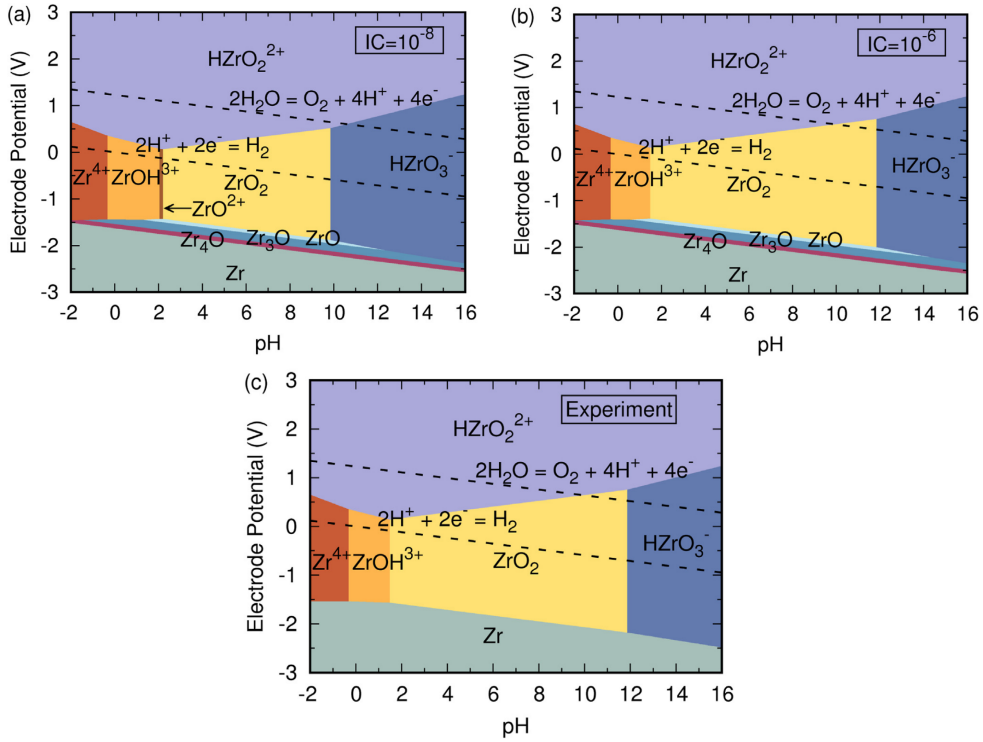


FIGURE 5.3: Pourbaix diagrams taken from *Jin et al.* derived from DFT calculations with HSE06 functionals and ionic concentration of $10^{-6}$ M [80]. a) corrected relative chemical potentials b) non-corrected relative chemical potentials c) derived from experimental thermodynamic data only.

$ZrOH^{3+}$ was omitted from these calculations. Overall, there is a better agreement between the experimentally derived zirconium Pourbaix diagram with those of *Jin et al.* than the diagrams created using literature data. However, the presence of $ZrO^{2+}$, shown in Figure 5.3 a) is a concern.

Figure 4.8 is also found to have a better agreement with Figure 1.4. It may be interesting to note that while $ZrO^{2+}$ is known to be disproven, the bottom of the stability region appears to closely match that of $ZrO_2$ region determined in this work, for both the electrochemical potential and pH at $10^{-6}$ M.

*Kraš and Milošev* [71] also created a Pourbaix diagram for zirconium, which is given in Figure 5.4. This was done using thermodynamic data from *Brown et al.* [23], SIT theory, and a code base called Spana [71]. This diagram should be expected to be slightly different as *Kraš and Milošev* chose to include polynuclear hydrolysis species for concentrations greater than $10^{-4}$ M [71]. The stability

region of metallic Zr can be seen to be very similar between Figures 4.8 and 5.4. For $Zr^{4+}$, the region is much larger than predicted in this work for 373.15 K, with it extending out to approximately pH 1. This variation is not unusual to see for Pourbaix diagrams given the difference in temperature. A similar effect can be seen if one compares the stability region of $Zr^{4+}$ in Figures 4.7 and 4.8.

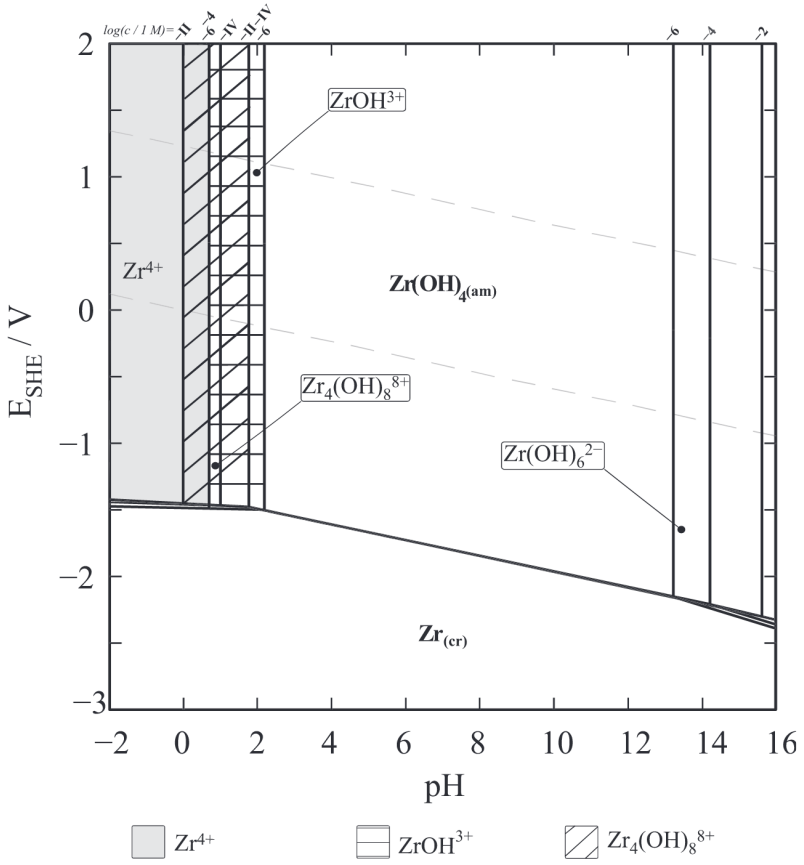


FIGURE 5.4: Zirconium Pourbaix diagram at 298.15 K, with varying ionic strength in NaCl taken from *Kraš and Milošev* [71].

The stability region for $Zr(OH)_6^{2-}$ can be seen to extend leftward to approximately pH 13 for $10^{-6}$ M. This agrees relatively well with the hydrolysis plot in Figure 2.1, and further indicates that additional refinement is required for $Zr(OH)_6^{2-}$. The presence of $Zr(OH)_{4\,(aq)}$ rather than $ZrO_2$ is not a concern as $Zr(OH)_{4\,(aq)}$ is typically taken as the hydrated form of $ZrO_2$. This is stated as such by *Kraš and Milošev* [71].

Overall, the experimentally derived Pourbaix diagram for zirconium at 373.15 K in this work is believed to be an improvement over the previous diagram by Pourbaix at 298 K [18]. However, further refinement for the estimations of the heat capacity for certain ions and better isolation of $ZrOH^{3+}$ is required before it can be recommended to be used in any material development purposes. Additionally, polynuclear hydrolysis species should be included for any environment where higher aqueous metal concentration are expected.

### 5.3.2 Zircaloy-4

There are immediate differences in the individual element Pourbaix diagrams given by *Beverskog and Puigdomenech* [56] and *Palazhchenko* [42] when compared to the Pourbaix diagrams for Zircaloy-4 in Figures 4.9 and 4.10. The Pourbaix diagram for tin at 358.15 K developed by *Palazhchenko* is given in Figure 5.5. It predicts that the metallic form would be thermodynamically dominant from -0.8 V to approximately -0.45 V and a pH range of -4 to approximately 8.5, with the electrochemical potential range decreasing as the pH increased [42].

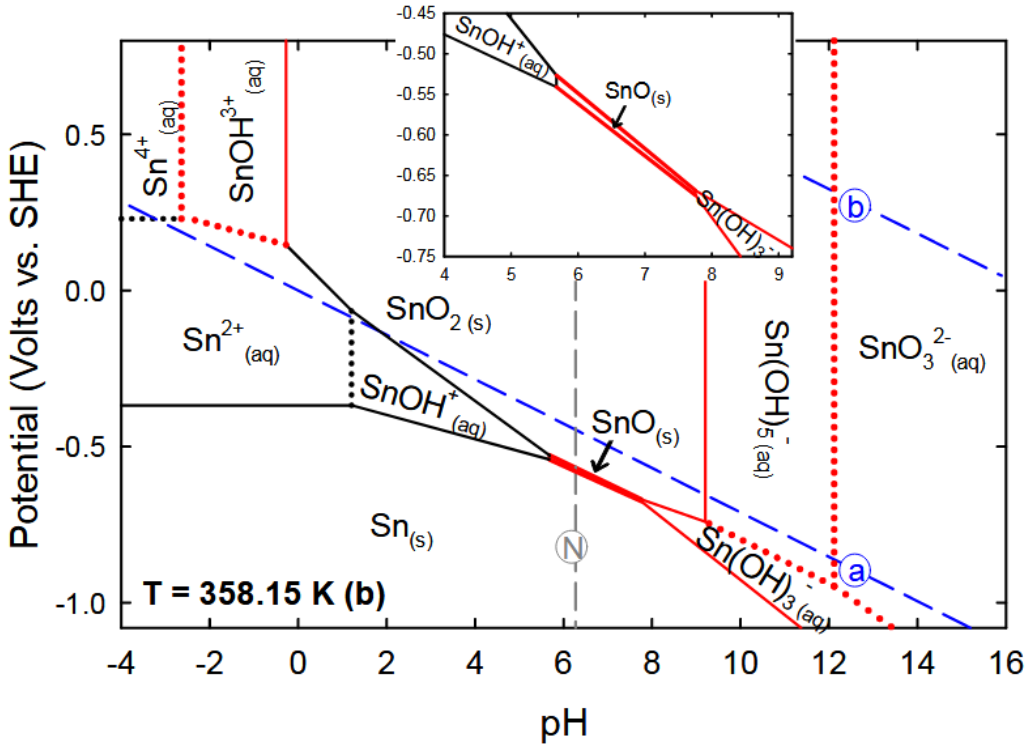


FIGURE 5.5: Pourbaix diagram for tin at 358.15 K and a concentration of $10^{-6}$ M constructed by *Palazhchenko* using experimental data [42].

Conversely, Figure 4.10 for Zircaloy-4 at 373.15 K predicts that the tin components will be in the form of $SnO_2$, and therefore passivating rather than immune to corrosion. In fact, the 373.15 K Pourbaix diagram predicts that $SnO_2$ will be thermodynamically dominant over the entire given ranges. However, the thermodynamically dominant species can change dramatically with the change in temperature. This can be seen when Figures 4.9 and 4.10 are compared; $SnO_2$ is no longer present and$Sn(OH)_6^{2-}$ is thermodynamically dominant over the majority of the diagram indicating that the tin content in Zircaloy-4 at 298.15 K would be expected to undergo corrosion. The metallic form is shown to be dominant at reducing electrochemical potentials up to a pH of 10. Overall, the direct comparison of the Zircaloy-4 diagrams with that of *Palazhchenko* [42] must be treated with caution as the thermodynamic behaviour of tin is expected to vary in the alloy than when being a pure metal.

The 373 K Pourbaix diagram of chromium, shown in Figure 5.6, was seen to have similar stability regions to those seen in the 373.15 K Pourbaix diagram of Zircaloy-4. In Figure 4.10, chromium metal can be seen to be the thermodynamically dominant form, below -1.6 V over the entire pH range. This is seen in Figure 5.6, but above this electrochemical potential the stability region is seen to drop around a pH of 7 [56]. Whereas in this work, the drop is expected earlier at a pH of approximately 5.

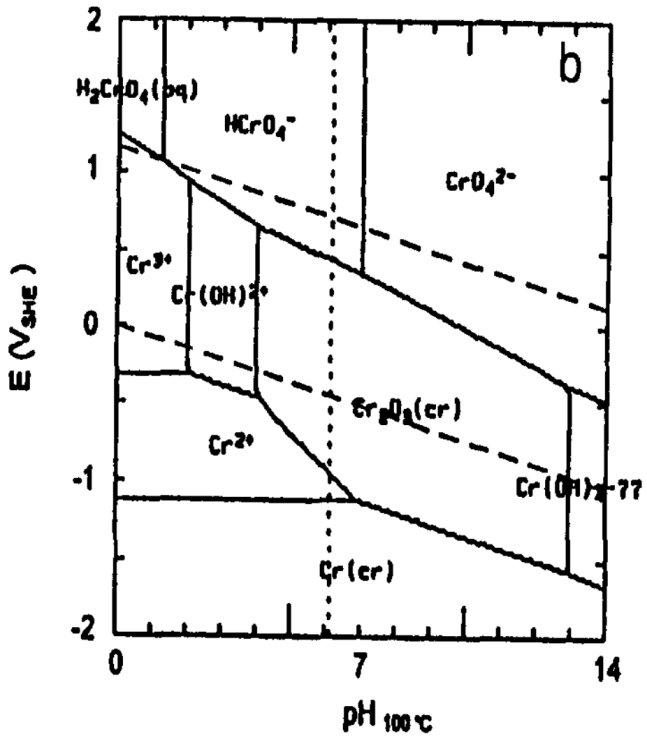


FIGURE 5.6: Chromium Pourbaix diagram at 373.15 K and $[Cr(aq)]_{tot}$ of $10^{-6}$ M, taken from *Beverskog and Puigdomenech* [56].

A key difference can be seen between Figures 4.10 and 5.6 for the stability region of $Cr(OH)^{2+}$. In this work, $Cr(OH)^{2+}$ is predicted to be stable only in a very small pH range, from between approximately 2.3 to 2.4 pH. Whereas *Beverskog and Puigdomenech* predicted $Cr(OH)^{2+}$ to be stable in the approximate range of 2.5 to 4 pH, with similar electrochemical potential bounds [56]. $Cr(OH)_4^-$ is not seen in Figure 4.10; however, this is a result of omission rather than it being predicted to be non-dominant. While the Pourbaix diagram of

Zircaloy-4 can be compared to the Pourbaix diagram of its constituent elements, it is not possible to compare Zircaloy-4 to other Pourbaix diagrams of itself. This is because a Pourbaix diagram for Zircaloy-4 is not available in the open literature. The diagram can be compared to the experimental concentration measurements made to apply some experimental validation.

In Figures 4.4 and 5.1, it is seen that minimal aqueous dissolution of tin and zirconium occurred in each of the four tested pH ranges. With the highest aqueous concentrations of zirconium and tin being in the pH -1–0 range. Chromium was seen to have high aqueous concentrations in the pH 13–14 and -1–0 ranges.

These measurements for chromium coincide well with the presented Pourbaix diagrams for Zircaloy-4. Assuming similar ORP ranges to those seen in Table 4.3 and a pH range of 13–14, chromium would be expected to be in the thermodynamically dominant form of $CrO_4^{2-}$. This indicates that the chromium should be actively corroding in those conditions, while tin and zirconium would both be in oxide forms and would be passivating, though some corrosion would be expected for tin and zirconium while the oxide layers form. This is similarly true for the pH -1–0 range, with chromium in the form of $H_2CrO_{4\,(aq)}$.

The pH 7 range would be near the three boundary region intersection point at approximately 0.4 V in Figure 4.10, with chromium either being passivating or corroding. Tin and zirconium would be expected to be passivating in and around this region in Figures 4.9 and 4.10. The aqueous concentrations in this region coincide well with Figure 4.10. Chromium was measured to have the lowest concentration, followed by tin and zirconium. This lower aqueous concentration of chromium matches the prediction in Figures 4.9 and 4.10 that chromium would be in the form of $Cr_2O_3$ and would be passivating.

In a pH range of 0–1 and an electrochemical potential between 1.0 V to 1.1 V, it is predicted by Figure 4.10 that chromium should be actively corroding, while

zirconium and tin are passivating. Tin was seen to have a minimal aqueous concentration by the 8th day, while chromium and zirconium were seen to have similar concentrations. It may be that the stability regions for zirconium species in this range are incorrect in Figure 4.10. However, chloride ions were present in solution and their effects were not accounted for in the Pourbaix diagram.

These chloride ions may have caused enhanced corrosion of the zirconium metal in the Zircaloy-4 sample. Further works should attempt to account for this behaviour, if hydrochloric acid is used. Overall, it is expected that small amounts of aqueous corrosion would occur for Zircaloy-4 at 373.15 K based on the Pourbaix diagram of Zircaloy-4.

It is also important to provide meaning for the presented Pourbaix diagram of Zircaloy-4 in the context of uses of the alloy. The cooling systems in the primary heat transport systems, because of LiOH additions, operate under alkaline conditions, approximately pH 10 [2, 73]. While the presence of lithium ions is not included in this work, Figure 4.10 shows that at pH 10 both zirconium and tin should form passivating layers over the entire electrochemical potential range. In these conditions, chromium would be expected to be either immune to corrosion or passivating, unless more oxidizing conditions are met, which would result in corrosion. This behaviour may also be true for higher temperatures. However, as seen between Figures 4.9 and 4.10, the thermodynamically dominant species can vary as the temperature is increased. Therefore, it is possible that additional aqueous corrosion could occur under CANDU coolant system operating parameters and further work should be performed to confirm this.

# Chapter 6

# Conclusions

The aims of this work were three-fold: to investigate the aqueous corrosion and corrosion species of zirconium and Zircaloy-4 up to 373.15 K; to perform empirical solubility measurements of the Zr-$H_2O$ system at 373.15 K to fill knowledge gaps at these temperatures; and to develop elevated temperature Pourbaix diagrams for zirconium and Zircaloy-4. This resulted in the hydrolysis constants and Gibbs energy of formation at 373.15 K to be determined for $Zr(OH)_6^{2-}$, $Zr(OH)_{4\,(aq)}$, and $Zr(OH)_2^{2+}$, alongside the creation of the aforementioned Pourbaix diagrams. These diagrams were compared to other standard condition and elevated temperature Pourbaix diagrams created using computational or extrapolation methods.

The values for the Gibbs energy of formation at 373.15 K were found to be lower than those values at standard conditions reported in literature, indicating an increase in the thermodynamic stability of aqueous zirconium ions at elevated temperatures. From this work, the Gibbs energy of formation at 373.15 K were determined to be -2177.4±8.5 kJ/mol, -1704.9±1.5 kJ/mol, and -1095.1±2.7 kJ/mol, for $Zr(OH)_6^{2-}$, $Zr(OH)_{4\,(aq)}$, and $Zr(OH)_2^{2+}$, respectively. An increase was also seen in the hydrolysis constants of these species at elevated temperatures, with values of -19.39±1.98, 1.77±1.60, and 3.72±1.63, for $Zr(OH)_6^{2-}$, $Zr(OH)_{4\,(aq)}$, and $Zr(OH)_2^{2+}$, respectively. These values are presented with the caveat that an artificial increase in the solubility of zirconium oxide was possible as a result of carbon dioxide contamination

and complexation by chloride ions in the acidic regimes. The Gibbs energy of formation and the hydrolysis constant were determined for $Zr(OH)^{3+}$. However, these were disregarded due to inadequate isolation of the ion, and this species was omitted from the resulting Pourbaix diagrams, since the measured data were suspect.

The experimentally derived elevated temperature Pourbaix diagram of zirconium was found to be similar with those calculated at 298 K, using computational methods, though with some dissimilarities in the stability domains of the species. In particular, $Zr(OH)_6^{2-}$ was predicted to be the dominant species at electrochemcial potentials above -2 V and from pH 4–14. This is contrary to diagrams at 298 K, where $ZrO_2$ or $Zr(OH)_4$ (analogous species) are predicted to be stable over large areas. Other works involving solubility measurements of $ZrO_2$ agree with this prediction and it is likely that the estimation of the heat capacity for $Zr(OH)_6^{2-}$ was flawed, thus leading to an overestimated stability region to a pH of 4.

A multi-element Pourbaix diagram accounting for zirconium, tin, and chromium was presented for Zircaloy-4 at both 298.15 K and 373.15 K. From this diagram it was found that Zircaloy-4 is expected to form metallic oxides for all three elements in reducing conditions above pH 5. Zirconium is expected to form either oxides or remain in the metallic form above approximately pH -0.75. Below this pH, active corrosion is expected to occur. Tin is predicted to remain in the oxide form over all given ranges. However, chromium was predicted to corrode in all oxidizing conditions and acidic conditions above potentials of -1.0 V. This expectation was partially corroborated by aqueous concentration measurements using ICP-MS, where chromium concentrations were measured to be one to two magnitudes greater than zirconium and tin in pH ranges of 13–14 and -1–0.

Lastly, it is recommended that the Pourbaix diagrams of zirconium and Zircaloy-4 be further improved before being used in any material development

at 373.15 K. Estimations of the ionic species heat capacities were performed primarily using the Criss-Cobble method while more modern techniques and models are available. These models were not used in this work as the required experimentally determined values were not available, and their higher complexity. Finally, it is recommended that diagrams be created up to 573.15 K to more closely match the operating conditions of a CANDU reactor cooling system.

# Chapter 7

# Recommended Future Work

There are twelve recommendations that should be considered when performing further high temperature solubility measurements and empirical Pourbaix diagram development. These recommendations apply for experimentation at 373.15 K and above.

## 7.1 Experimental Apparatus and Solution Preparation

It is recommended that all further measurements be performed under an inert/carbon dioxide free atmosphere to eliminate any concern of carbon dioxide contamination. Longer duration experiments are also recommended to ensure the system has reached a true equilibrium state and that all concentration measurements be performed using ICP-MS.

It is also advised that an autoclave developed for corrosion experiments be utilized for further works. This is to ensure the apparatus is robust against extreme and varied conditions. The internal lining of this autoclave should also be composed of a high temperature corrosion resistance material, such as Hastelloy, in part due to the decomposition of Teflon at 573 K. The pH and ORP probes would also need to be replaced with platinum or yttria-stabilized $ZrO_2$ based probes as the maximum operating temperature of the current probes is 408 K. The replacement of the current probes would also allow for the

use of perchloric acid rather than hydrochloric acid, eliminating the chloride complexation issue.

It is recommended that a flow-through analysis system be developed in tandem with ICP-MS. This would allow for rapid concentration measurements without requiring the decrease of the sample temperature for analysis.

## 7.2 Improvements to Pourbaix Diagrams

Further steps can be taken to improve the Pourbaix diagrams for Zircaloy-4 and zirconium at elevated temperatures. It is recommended that an alternate program be used to develop these Pourbaix diagrams rather than FactSage [31], because of the technical limitations in place that prevent more than three metals to be included in calculations, and a total of five elements.

As seen in the work by *Wang et al.* [22], Thermo-Calc is a potential alternative application. It is capable of accounting for a greater number of elements as well an non-stoichiometric oxides. The inclusion of these non-stoichiometric oxides could be potentially valuable for Zircaloy-4. This would also allow for the inclusion of iron in the diagram. Additionally, polynuclear species should be included in future Pourbaix diagrams of zirconium and Zircaloy-4.

Heat capacity values estimated using the Criss-Cobble method should be replaced with the HKF model for future Pourbaix diagrams as it is a more empirically derived method. This would require additional work to determine the experimentally derived constants.

Lastly, some CANDU reactor specific recommendations can be made for Zircaloy-4. Irradiation of Zircaloy-4 can affect its corrosion properties and was not accounted for in this work. It is recommended that corrosion experiments be performed on both non-irradiated and irradiated Zircaloy-4 samples in order to see if the corrosion products and resulting Pourbaix diagram change. CANDU coolant systems also operate within a specific pH range and LiOH is added to

the coolant water. It is recommended that repeat experiments be performed at elevated temperatures for Zircaloy-4 closer to these operating conditions to better represent possible corrosion in reactors.

# References

[1] Atomic Energy of Canada Limited, "CANDU 6 Technical Summary," Atomic Energy of Canada Ltd., Sheridan Park (Ontario), Tech. Rep., 2005.

[2] R. Chaplin, "Nuclear Plant Systems," in *The Essential CANDU, A Textbook on the CANDU Nuclear Power Plant Technology*, W. J. Garland, Ed., 1st ed. University Network of Excellence in Nuclear Engineering (UNENE), 2014, ch. 8.

[3] M. Tayal and M. Gacesa, "Storage and Disposal of Irradiated Fuel," in *The Essential CANDU, A Textbook on the CANDU Nuclear Power Plant Technology*, W. J. Garland, Ed., 1st ed. University Network of Excellence in Nuclear Engineering (UNENE), 2014, ch. 19.

[4] D. W. Shoesmith and D. Zagidulin, "The Corrosion of Zirconium Under Deep Geologic Repository Conditions," *Journal of Nuclear Materials*, vol. 418, pp. 292–306, 2011. DOI: 10.1016/j.jnucmat.2011.07.028.

[5] E. McCafferty, *Introduction to Corrosion Science*, 1st ed. Springer New York, NY, 2009, ISBN: 978-1-4419-0455-3.

[6] D. H. Lister and W. G. Cook, "Nuclear Plant Materials and Corrosion," in *The Essential CANDU, A Textbook on the CANDU Nuclear Power Plant Technology*, W. J. Garland, Ed., 1st ed. University Network of Excellence in Nuclear Engineering (UNENE), 2014, ch. 14.

[7] P. Vanýsek, "Electrochemical Series," in *CRC Handbook of Chemistry and Physics*, 93rd ed. CRC Press, 2012, ch. 5, p. 80.

[8] R. Adamson, F. Garzarolli, B. Cox, A. Strasser, and P. Rudling, "Corrosion Mechanisms in Zirconium Alloys," ZIRAT12 Special Topic Report 2007.

[9] N. Ramasubramanian, "Shadow Corrosion," *Journal of Nuclear Materials*, vol. 328, pp. 249–252, 2004, ISSN: 0022-3115. DOI: https://doi.org/10.1016/j.jnucmat.2004.04.329.

[10] F. Garzarolli, P. B. Hoffmann, and A. Seibold, "Shadow Corrosion or Crevice Corrosion?" *Journal of Nuclear Materials*, vol. 289, pp. 338–341, 2001. DOI: 10.1016/S0022-3115(01)00429-9.

[11] R. Rebak, Y.-P. Lin, and Y.-J. Kim, "Review on Electrochemical Corrosion of Zirconium Alloys in High Temperature Water," in *14th International Conference on Environmental Degradation of Materials in Nuclear Power Systems Water Reactors 2009*, (Virginia Beach, Virginia, USA), vol. 2, American Nuclear Society, 2009, pp. 1400–1406, ISBN: 9781617388538.

[12] P. Wang, K. Nowotka, and G. S. Was, "Reproducing Shadow Corrosion on Zircaloy-2 Using In-situ Proton Irradiation," *Journal of Nuclear Materials*, vol. 558, 2022, ISSN: 0022-3115. DOI: https://doi.org/10.1016/j.jnucmat.2021.153406.

[13] B. Cox, "Some Thoughts on the Mechanisms of In-Reactor Corrosion of Zirconium Alloys," *Journal of Nuclear Materials*, vol. 336, pp. 331–368, 2005. DOI: 10.1016/j.jnucmat.2004.09.029.

[14] W. G. Cook and D. H. Lister, "Chemistry in CANDU Process Systems," in *The Essential CANDU, A Textbook on the CANDU Nuclear Power Plant Technology*, W. J. Garland, Ed., 1st ed. University Network of Excellence in Nuclear Engineering (UNENE), 2014, ch. 15.

[15] S. Müller and L. Lanzani, "Corrosion of Zirconium Alloys in Concentrated Lithium Hydroxide Solutions," *Journal of Nuclear Materials*, vol. 439, pp. 251–257, 2013. DOI: 10.1016/j.jnucmat.2012.07.030.

[16] B. Cox, M. Ungurelu, Y.-M. Wong, and C. Wu, "Mechanisms of LiOH Degradation and $H_3BO_3$ Repair of $ZrO_2$ Films," in *Zirconium in the Nuclear Industry: Eleventh International Symposium*, E. R. Bradly and G. P. Sabol, Eds. ASTM International, 1996, pp. 114–136.

[17] J. E. D. Verink, "Simpified Procedure for Constructing Pourbaix Diagrams," in *Uhlig's Corrosion Handbook Third Edition*, R. W. Revie, Ed., John Wiley & Sons, Inc., 2011, ch. 7, pp. 93–101.

[18] M. Maraghini, E. Deltombe, N. D. Zoubov, P. V. Rysselberghe, and M. Pourbaix, "Zirconium," in *Atlas of Electrochemical Equilibria in Aqueous Solutions*, National Association of Corrosion Engineers, 1974, pp. 223–229.

[19] W. T. Thompson, M. H. Kaye, C. W. Bale, and A. D. Pelton, "Pourbaix Diagrams for Multielement Systems," in *Uhlig's Corrosion Handbook Third Edition*, R. W. Revie, Ed., John Wiley & Sons, Inc., 2011, ch. 8, pp. 102–110.

[20] C. M. Criss and J. W. Cobble, "The Thermodynamic Properties of High Temperature Aqueous Solutions. IV. Entropies of the Ions up to 200° and the Correspondence Principle," *Journal of the American Chemical Society*, vol. 86, pp. 5385–5390, 1964, ISSN: 0002-7863. DOI: https://doi.org/10.1021/ja01078a003.

[21] C. M. Criss and J. W. Cobble, "The Thermodynamic Properties of High Temperature Aqueous Solutions. V. The Calculation of Ionic Heat Capacities up to 200°. Entropies and Heat Capacities above 200°," *Journal of the American Chemical Society*, vol. 86, pp. 5390–5393, 1964, ISSN: 0002-7863. DOI: https://doi.org/10.1021/ja01078a004.

[22] K. Wang, J. Han, A. Y. Gerard, J. R. Scully, and B.-C. Zhou, "Potential-pH Diagrams Considering Complex Oxide Solution Phases for Understanding Aqueous Corrosion of Multi-Principal Element Alloys," *npj Materials Degradation*, vol. 4, pp. 1–11, 2020, ISSN: 2397-2106. DOI: 10.1038/s41529-020-00141-6.

[23] P. L. Brown, E. Curti, and C. Ekberg, *Chemical Thermodynamics of Zirconium*, 1st ed., J. Perrone and M. Illemassène, Eds. Elsevier, 2005, ISBN: 978-0-08-045753-6.

[24] J. W. Cobble, "Empirical Considerations of Entropy. II. The Entropies of Inorganic Complex Ions," *The Journal of Chemical Physics*, vol. 21, pp. 1446–1450, 1953, ISSN: 0021-9606. DOI: 10.1063/1.1699277.

[25] R. E. Powell and W. M. Latimer, "The Entropy of Aqueous Solutes," *The Journal of Chemical Physics*, vol. 19, pp. 1139–1141, 1951, ISSN: 0021-9606. DOI: 10.1063/1.1748492.

[26] E. L. Shock, H. C. Helgeson, and D. A. Sverjensky, "Calculation of the Thermodynamic and Transport Properties of Aqueous Species at High Pressures and Temperatures: Standard Partial Molal Properties of Inorganic Neutral Species," *Geochimica et Cosmochimica Acta*, vol. 53, pp. 2157–2183, 1989, ISSN: 0016-7037. DOI: 10.1016/0016-7037(89)90341-4.

[27] J. C. Tanger and H. C. Helgeson, "Calculation of the Thermodynamic and Transport Properties of Aqueous Species at High Pressures and Temperatures; Revised Equations of State for the Standard Partial Molal Properties of Ions and Electrolytes," *American Journal of Science*, vol. 288, pp. 19–98, 1988, ISSN: 0002-9599. DOI: 10.2475/ajs.288.1.19.

[28] E. L. Shock and H. C. Helgeson, "Calculation of the Thermodynamic and Transport Properties of Aqueous Species at High Pressures and Temperatures: Correlation Algorithms for Ionic Species and Equation of State Predictions to 5 kb and 1000°C," *Geochimica et Cosmochimica Acta*, vol. 52, pp. 2009–2036, 1988. DOI: 10.1016/0016-7037(88)90181-0.

[29] E. L. Shock, E. H. Oelkers, J. W. Johnson, D. A. Sverjensky, and H. C. Helgeson, "Calculation of the Thermodynamic Properties of Aqueous Species at High Pressures and Temperatures. Effective Electrostatic Radii,

Dissociation Constants and Standard Partial Molal Properties to 1000 °C and 5 kbar," *Journal of the Chemical Society, Faraday Transactions*, vol. 88, pp. 803–826, 1992, ISSN: 1364-5455. DOI: 10.1039/FT9928800803.

[30] G. D. Miron, A. M. M. Leal, and A. Yapparova, "Thermodynamic Properties of Aqueous Species Calculated Using the HKF Model: How Do Different Thermodynamic and Electrostatic Models for Solvent Water Affect Calculated Aqueous Properties?" *Geofluids*, vol. 2019, pp. 1–24, 2019, ISSN: 1468-8115. DOI: 10.1155/2019/5750390.

[31] C. W. Bale, E. Bélisle, P. Chartrand, S. A. Decterov, G. Eriksson, A. E. Gheribi, K. Hack, I.-H. Jung, Y.-B. Kang, J. Melançon, A. D. Pelton, S. Petersen, C. Robelin, J. Sangster, P. Spencer, and M.-A. V. Ende, "FactSage Thermochemical Software and Databases, 2010–2016," *Calphad*, vol. 54, pp. 35–53, 2016. DOI: 10.1016/j.calphad.2016.05.002.

[32] D. O. Northwood, "The Development and Applications of Zirconium Alloys," *Materials & Design*, vol. 6, pp. 58–70, 1985, ISSN: 0261-3069. DOI: 10.1016/0261-3069(85)90165-7.

[33] A. J. Zielen and R. E. Connick, "The Hydrolytic Polymerization of Zirconium in Perchloric Acid Solutions," *Journal of the American Chemical Society*, vol. 78, pp. 5785–5792, 1956, ISSN: 0002-7863. DOI: 10.1021/ja01603a019.

[34] C. Ekberg, G. Källvenius, Y. Albinsson, and P. L. Brown, "Studies on the Hydrolytic Behavior of Zirconium(IV)," *Journal of Solution Chemistry*, vol. 33, pp. 47–79, 2004, ISSN: 1572-8927. DOI: 10.1023/B:JOSL.0000026645.41309.d3.

[35] T. Kobayashi, T. Sasaki, I. Takagi, and H. Moriyama, "Solubility of Zirconium(IV) Hydrous Oxides," *Journal of Nuclear Science and Technology*, vol. 44, pp. 90–94, 2007, ISSN: 0022-3131. DOI: 10.1080/18811248.2007.9711260.

[36] C. F. Baes and R. E. Mesmer, *The Hydrolysis of Cations*. John Wiley & Sons, 1976, ISBN: 978-0-471-03985-3.

[37] S. U. Aja, S. A. Wood, and A. E. Williams-Jones, "The aqueous Geochemistry of Zr and the Solubility of Some Zr-Bearing Minerals," *Applied Geochemistry*, vol. 10, pp. 603–620, 1995, ISSN: 0883-2927. DOI: 10.1016/0883-2927(95)00026-7.

[38] H. Bilinski, M. Branica, and L. G. Sillen, "Precipitation and Hydrolysis of Metallic Ions. II. Studies on the Solubility of Zirconium Hydroxide in Dilute Solutions and in 1 M $NaClO_4$," *Acta Chemica Scandinavica*, vol. 20, pp. 853–861, 1966. DOI: 10.3891/acta.chem.scand.20-0853.

[39] I. A. Sheka and T. V. Pevzner, "Solubility of Zirconium and Hafnium in Sodium Hydroxide Solutions," *Russian Journal of Inorganic Chemistry*, vol. 5, pp. 1119–1121, 1960.

[40] E. L. Shock, D. C. Sassani, M. Willis, and D. A. Sverjensky, "Inorganic Species in Geologic Fluids: Correlations Among Standard Molal Thermodynamic Properties of Aqueous Ions and Hydroxide Complexes," *Geochimica et Cosmochimica Acta*, vol. 61, pp. 907–950, 1997. DOI: 10.1016/S0016-7037(96)00339-0.

[41] M. H. Kaye and W. T. Thompson, "Computation of Pourbaix Diagrams at Elevated Temperature," in *Uhlig's Corrosion Handbook Third Edition*, R. W. Revie, Ed., John Wiley & Sons, Inc., 2011, ch. 9, pp. 111–122.

[42] O. Palazhchenko, "Pourbaix Diagrams at Elevated Temperatures A Study of Zn and Sn," M.Sc. Thesis, University of Ontario Institute of Technology, Oshawa, ON, Canada, 2012.

[43] H. Gamsjäger, T. Gajda, J. Sangster, S. K. Saxena, and W. Voigt, *Chemical Thermodynamics of Tin*, 1st ed., J. Perrone, Ed. OECD Publishing, 2012, ISBN: 978-92-64-99206-1.

[44] F. Séby, M. Potin-Gautier, E. Giffaut, and O. F. X. Donard, "A Critical Review of Thermodynamic Data for Inorganic Tin Species," *Geochimica et Cosmochimica Acta*, vol. 65, pp. 3041–3053, 2001. DOI: 10.1016/S0016-7037(01)00645-7.

[45] M. Pettine, F. J. Millero, and G. Macchi, "Hydrolysis of Tin(II) in Aqueous Solutions," *Analytical Chemistry*, vol. 53, pp. 1039–1043, 1981. DOI: 10.1021/ac00230a027.

[46] R. S. Tobias, "Studies on the Hydrolysis of Metal Ions. 21. The Hydrolysis of the Tin(II) Ion, $Sn^{2+}$," *Acta Chemica Scandinavica*, vol. 12, pp. 198–223, 1958.

[47] F. Salvatore, D. Ferri, M. Trifuoggi, C. Manfredi, and E. Vasca, "On the Hydrolysis of the Tin(II) Ion," *Annali di Chimica*, vol. 87, pp. 477–481, 1997.

[48] S. Gobom, "The Hydrolysis of the Tin(II) Ion," *Acta Chemica Scandinavica*, vol. 30, pp. 745–750, 1976.

[49] G. E. Kuril'chikova and V. L. Barsukov, "Stability of Hydroxistannate Complexes and Experimental Crystallization of Cassiterite Under Hydrothermal Conditions," *Geokhimiya*, vol. 1, pp. 35–42, 1970.

[50] T. Amaya, T. Chiba, K. Suzuki, C. Oda, H. Yoshikawa, and M. Yui, "Solubility of Sn(IV) Oxide in Dilute $NaClO_4$ Solution at Ambient Temperature," *MRS Online Proceeings Library*, vol. 465, pp. 751–758, 1997.

[51] C. Oda and T. Amaya, "Effects of ligands on the solubility of tin," Japanese Nuclear Cycle Development Institute, Naka-gun, Ibaraki, Japan, Tech. Rep. TN8400 98-001, 1998.

[52] D. Rai, M. Yui, H. T. Schaef, and A. Kitamura, "Thermodynamic Model for $SnO_2$(cr) and $SnO_2$(am) Solubility in the Aqueous $Na^+$–$H^+$–$OH^-$ –$Cl^-$ – $H_2O$ System," *Journal of Solution Chemistry*, vol. 40, pp. 1155–1172, 2011. DOI: 10.1007/s10953-011-9723-1.

[53] L. Duro, M. Grive, E. Cera, C. Domenech, and J. Bruno, "Update of a Thermodynamic Database for Radionuclides to Assist Solubility Limits Calculation for Performance Assessment," Swedish Nuclear Fuel and Waste Management Co, Stockholm, Sweden, Tech. Rep. TR-06-17, 2006.

[54] ThermoChimie Partners, "*Thermo-Chimie*", version V11a, ThermoChimie Consortium, 1/7 rue Jean Monnet Parc de la Croix Blanche 92298 Châtenay-Malabry France, 2022.

[55] K. J. Jackson and H. C. Helgeson, "Chemical and Thermodynamic Constraints on the Hydrothermal Transport and Deposition of Tin: I. Calculation of the Solubility of Cassiterite at High Pressures and Temperatures," *Geochimica et Cosmochimica Acta*, vol. 49, pp. 1–22, 1984. DOI: 10.1016/0016-7037(85)90187-5.

[56] B. Beverskog and I. Puigdomenech, "Revised Pourbaix Diagrams for Chromium at 25–300 °C," *Corrosion Science*, vol. 39, pp. 43–57, 1997. DOI: 10.1016/S0010-938X(97)89244-X.

[57] W. G. Cook and R. P. Olive, "Pourbaix Diagrams for Chromium, Aluminum and Titanium Extended to High-Subcritical and Low-Supercritical Conditions," *Corrosion Science*, vol. 58, pp. 291–298, 2012. DOI: 10.1016/j.corsci.2012.02.002.

[58] O. Knacke, O. Kubaschewski, and K. Hesselmann, *Thermochemical Properties of Inorganic Substances*, 2nd ed. Springer-Verlag, 1991.

[59] D. Rai, B. M. Sass, and D. A. Moore, "Chromium(III) Hydrolysis Constants and Solubility of Chromium(III) Hydroxide," *Inorganic Chemistry*, vol. 26, pp. 345–349, 1987. DOI: 10.1021/ic00250a002.

[60] J. Chivot, "Thermodynamique Des Produits de Corrosion: Fonctions Thermodynamiques, Diagrammes de Solubilité, Diagrammes E-pH des Systèmes Fe-$H_2O$, Fe-$CO_2$-$H_2O$, Fe-S-$H_2O$, Cr-$H_2O$ et Ni-$H_2O$ en Fonction de la Température," National Agency for Radioactive

Waste Management, rue Jean Monnet Parc de la Croix-Blanche 92298 Châtenay-Malabry Cedex France, Tech. Rep., 2004.

[61] J. W. Ball and D. K. Nordstrom, "Critical Evaluation and Selection of Standard State Thermodynamic Properties for Chromium Metal and Its Aqueous Ions, Hydrolysis Species, Oxides, and Hydroxides," *Journal of Chemical & Engineering Data*, vol. 43, pp. 895–918, 1998. DOI: 10.1021/je980080a.

[62] M. Szabó, J. Kalmár, T. Ditrói, G. Bellér, G. Lente, N. Simic, and I. Fábián, "Equilibria and Kinetics of Chromium(VI) Speciation in Aqueous Solution – A Comprehensive Study from pH 2 to 11," *Inorganica Chimica Acta*, vol. 472, pp. 295–301, 2018. DOI: 10.1016/j.ica.2017.05.038.

[63] I. Dellien, F. M. Hall, and L. G. Hepler, "Chromium, Molybdenum, and Tungsten: Thermodynamic Properties, Chemical Equilibriums, and Standard Potentials," *Chemical Reviews*, vol. 76, pp. 283–310, 1976. DOI: 10.1021/cr60301a001.

[64] P. J. Atkins, J. D. Paula, and J. Keeler, *Atkins' Physical Chemistry*, 11th ed. Oxford Univ. Press, 2017, ISBN: 978-0-19-876986-6.

[65] M. R. Wright, *An Introduction to Aqueous Electrolyte*, 1st ed. Wiley, 2007, ISBN: 978-0-470-51171-8.

[66] D. A. Skoog, J. F. Holler, and S. R. Crouch, *Principles of Instrumental Analysis*, 7th ed. Cengage Learning, 2018, ISBN: 978-1-337-46803-9.

[67] G. G. Manov, R. G. Bates, W. J. Hamer, and S. F. Acree, "Values of the Constants in the Debye-Hückel Equation for Activity Coefficients," *Journal of the American Chemical Society*, vol. 65, pp. 1765–1767, 1943. DOI: 10.1021/ja01249a028.

[68] M. Wang, Y. Zhang, and M. Muhammed, "Critical Evaluation of Thermodynamics of Complex Formation of Metal Ions in Aqueous

Solutions I. A Description of Evaluation Methods," *Hydrometallurgy*, vol. 45, pp. 21–36, 1997. DOI: 10.1016/S0304-386X(96)00072-2.

[69] D. Cubicciotti, "Potential-pH Diagrams for Alloy-Water Systems Under LWR Conditions," *Journal of Nuclear Materials*, vol. 201, pp. 176–183, 1993. DOI: 10.1016/0022-3115(93)90173-V.

[70] L. Kaufman, J. H. Perepezko, K. Hildal, J. Farmer, D. Day, N. Yang, and D. Branagan, "Transformation, Stability and Pourbaix Diagrams of High Performance Corrosion Resistant (HPCRM) Alloys," *CALPHAD*, vol. 33, pp. 89–99, 2009. DOI: 10.1016/j.calphad.2008.09.019.

[71] A. Kraš and I. Milošev, "The Aqueous Chemistry of Zirconium as a Basis for Better Understanding the Formation of Zirconium Conversion Coatings: Updated Thermodynamic Data," *Journal of the Electrochemical Society*, vol. 170, p. 021 508, 2023. DOI: 10.1149/1945-7111/acb9c2.

[72] E. Curti and C. Degueldre, "Solubility and Hydrolysis of Zr Oxides: A Review and Supplemental Data," *Radiochimica Acta*, vol. 90, pp. 801–804, 2002. DOI: 10.1524/ract.2002.90.9-11_2002.801.

[73] L. Qiu, D. A. Guzonas, and D. G. Webb, "Zirconium Dioxide Solubility in High Temperature Aqueous Solutions," *Journal of Solution Chemistry*, vol. 38, pp. 857–867, 2009. DOI: 10.1007/s10953-009-9412-5.

[74] A. S. Solovkin and Z. N. Tsvetkova, "The Chemistry of Aqueous Solutions of Zirconium Salts (Does the Zirconyl Ion Exist?)" *Russian Chemical Reviews*, vol. 31, pp. 655–669, 1962. DOI: 10.1070/RC1962v031n11ABEH001326.

[75] M. A. Pouchon, E. Curti, C. Degueldre, and L. Tobler, "The influence of Carbonate Complexes on the Solubility of Zirconia: New Experimental Data," *Progress in Nuclear Energy*, vol. 38, pp. 443–446, 2001. DOI: 10.1016/S0149-1970(00)00155-4.

[76] A. Clearfield and P. A. Vaughan, "The Crystal Structure of Zirconyl Chloride Octahydrate and Zirconyl Bromide Octahydrate," *Acta Crystallographica*, vol. 9, pp. 555–558, 1956. DOI: 10 . 1107 / S0365110X56001558.

[77] G. Lundgren, "Crystal-Structure Studies on Some Basic Salts of Ce(IV), Th(IV), U(IV), Ti(IV), and Zr(IV)," *Svensk Kemisk Tidskrift*, vol. 71, pp. 200–220, 1959.

[78] D. B. McWhan and G. Lundgren, "The Crystal Structure of Some Zirconium Hydroxide Salts," *Acta Crystallogr. Section A*, vol. 16, p. 36, 1963.

[79] D. B. McWhan and G. Lundgren, "The Crystal Structure of $Zr_2(OH)_2(SO_4)_3(H_2O)_4$," *Inorganic Chemistry*, vol. 5, pp. 284–289, 1965. DOI: 10.1021/ic50036a027.

[80] G. Jin, C. Xu, S. Hu, and X. Zhou, "Temperature Dependent Electrochemical Equilibrium Diagram of Zirconium-Water System Studied with Density Functional Theory and Experimental Thermodynamic Data," *Journal of Nuclear Materials*, vol. 532, p. 152 036, 2020. DOI: 10.1016/j.jnucmat.2020.152036.